Structural and electronic properties of self-assembled molecular layers at the organic/metal interface

DISSERTATION

zur Erlangung des akademischen Grades
doctor rerum naturalium
(Dr. rer. nat.)
im Fach Physik

eingereicht an der
Mathematisch-Naturwissenschaftlichen Fakultät I
Humboldt-Universität zu Berlin

von
Herrn Dipl.-Phys. Hendrik Glowatzki
geboren am 09.07.1978 in Neubrandenburg

Präsident der Humboldt-Universität zu Berlin:
Prof. Dr. Dr. h.c. Christoph Markschies

Dekan der Mathematisch-Naturwissenschaftlichen Fakultät I:
Prof. Dr. Lutz-Helmut Schön

Gutachter:

1. Dr. Norbert Koch
2. Prof. Dr. Recardo Manzke
3. Prof. Dr. Jose Ignacio Pascual

eingereicht am:	19.01.2009
Tag der mündlichen Prüfung:	15.06.2009

Abstract

The interfaces between conjugated organic molecules and metal electrodes play an important role for the performance of organic devices, such as organic light emitting diodes (OLED), organic thin film transistors (OTFT) and organic solar cells (OPVC). In this thesis the structural and electronic properties at these interfaces are investigated. In particular, the focus of this work is given to molecular systems which undergo self-assembly. The critical parameter which drives the ordering behavior at the interface is the balance between the inter-molecular and molecule-metal interaction strength.

To highlight different aspects of the self-assembled growth of molecules, four different molecular systems were investigated. (i) The defect mediated growth of directed self-assembled molecular layers is explored. It will be shown, that addition of short alkyl chains to molecules leads to significant changes in the interaction balance. (ii) The fast attenuation of the substrate's influence on the molecular ordering with increasing thickness of the molecular layer will be evidenced by the observation of changes in the molecular orientation. Additionally, indications for one dimensional electron band formation are found in the multilayer. (iii) The initiation of strong chemical interactions with the metal substrate by fluorination of molecules is demonstrated by conducting annealing time dependent experiments. (iv) A novel attempt to decouple molecules from the metal substrate is presented. This is achieved by the insertion of a molecular template layer. Experimental and theoretical results prove the successful prevention of molecule-metal interactions, while at the same time metallic properties of the substrate are conserved. Furthermore, the inserted layer acts as a structural template.

To explore the properties of the molecular systems, several complementary experimental techniques were used. Structural properties were investigated by scanning probe microscopy (STM and AFM), low energy electron diffraction (LEED) and near edge X-ray absorption fine structure spectroscopy (NEXAFS). The electronic properties were discovered by using photoelectron spectroscopy (UPS and XPS).

Keywords:
organic/metal interfaces, self-assembly, scanning probe microscopy, photoelectron spectroscopy

Zusammenfassung

Eine entscheidende Rolle hinsichtlich der Effektivität organischer Halbleiter spielen die Grenzflächen zwischen den konjugierten, organischen Molekülen und den Metallelektroden. Inhalt dieser Arbeit ist die Untersuchung dieser Grenzflächen bezüglich ihrer strukturellen und elektronischen Eigenschaften. Von besonderem Interesse sind dabei molekulare Systeme, welche Selbstaggregation aufweisen. Der kritische Parameter, welcher Einfluss auf das Organisationsverhalten der Moleküle hat, ist das Verhältnis der inter-molekularen zu den Molekül-Metall Wechselwirkungsstärken.

Um verschiedene Aspekte der molekularen Selbstaggregation zu beleuchten, wurden vier verschiedene Systeme untersucht. (i) Das defekt-gesteuerte Wachstum gerichteter, selbstaggregierender Molekülschichten wird betrachtet. Es wird gezeigt, dass durch das Hinzufügen kurzer Alkylketten zu den Molekülen das Wechselwirkungsverhältnis deutlich verändert werden kann. (ii) Weiterhin wird anhand der Beobachtung von Orientierungsänderungen der Moleküle der mit zunehmender Schichtdicke schnell abnehmende Einfluss des Substrats auf die Molekülordnung nachgewiesen. Zusätzlich lassen sich in der Multilage Hinweise auf die Ausbildung eines eindimensionalen Elektronenbandes erkennen. (iii) Es wird gezeigt, dass durch Fluorination von Molekülen starke chemische Wechselwirkungen mit dem Substrat erzeugt werden können. (iv) Ein neuartiger Ansatz zur Entkopplung von Molekülen von dem Metall wird vorgestellt. Dies geschieht mit Hilfe einer molekularen Vorbeschichtung. Aus experimentellen und theoretischen Daten geht hervor, dass auf diese Art die Wechselwirkung zwischen Molekül und Metall verhindert wird, während gleichzeitig die metallischen Eigenschaften des Substrats erhalten bleiben. Weiterhin wirkt die Vorbeschichtung auch als strukturelle Maske.

Zur Erkundung der verschiedenen Eigenschaften der molekularen Systeme kamen komplementäre experimentelle Techniken zum Einsatz. Die strukturellen Eigenschaften wurden dabei mit Hilfe von Rastersondenmikroskopie (STM und AFM), Beugung niederenergetischer Elektronen (LEED) und Röntgen-Nahkanten-Absorptions-Spektroskopie (NEXAFS) ermittelt. Eine Bestimmung der elektronischen Eigenschaften erfolgte mittels Photoelektronenspektroskopie (UPS und XPS).

Schlagwörter:
organischer Halbleiter/Metall Grenzflächen, Selbstaggregation,
Rastersondenmikroskopie, Photoelektronenspektroskopie

Contents

1 Introduction

Over the last years the field of *organic electronics* has achieved increasing attention. Substantial progress has been made in the development of several organic device types, for example organic light emitting diodes (OLED) [1–5], organic thin film transistors (OTFT) [6–9] and organic solar cells (OPVC) [10–12]. Although, compared to classical Si based electronics, organic materials have relatively low charge-carrier mobilities, they exhibit a number of advantages which makes them unique and offer new possible applications. Since organic molecules are commonly flexible, they provide the possibility to build bendable devices in combination with appropriate flexible substrates. Many organic molecules are soluble, which enables for very simple processing of these materials. This includes fabrication of thin films by spin-coating or simple printing techniques which are well known from inkjet printers. Therefore, processing of organic materials can be much cheaper than their inorganic counterparts. Once an organic material is established in a particular application and goes into mass production, material costs are also minimized. Consequently, the use of organic materials is of interest also from an economic point of view. For example quite a large number of companies are spending a lot of effort in the development of organic radio frequency identification (RFID) chips, which can be potentially integrated into labels of daily products, replacing the conventional bar code. Moreover, organic devices are of interest not only due to economic aspects. One organic device which already hit the market and will surely revolutionize this segment in the next years are OLEDs. Today an increasing number of portable devices, e.g. digital cameras and music players, are already equipped with OLED displays. Due to the architecture of OLEDs they provide the possibility of much more compact and lighter assembly, while at the same time lowering the power consumption and significantly increasing the contrast of the display. Recently, the first commercial full color OLED television screen has been released by Sony Corporation. It is expected that the market for *organic electronics* will grow rapidly in the next years. And so does the scientific community.

Although, several commercial products which integrate *organic electron-*

ics are already available, many fundamental aspects are not quite understood satisfactorily. The basis are conjugated organic molecules (COM), which have been found to act like semiconductors. Consequently, first approaches to describe systems made of these materials were to adapt theoretical knowledge from the well known inorganic semiconductors. Very soon it was found that the behavior of organic molecules is much more complex [13], which can be described only partly by classical semiconductor physics. In devices made of organic molecules a lot of interfaces between different materials are found. It turned out that these interfaces are often the key but also the bottleneck for efficient charge carrier injection from one material into another and therefore define the properties of the device. Important parameters in this context are the ordering behavior, conformational changes and chemical reactions at interfaces. Since organic materials have to be contacted with electrodes and these are usually made of metals, the focus in this work is set to organic-metal interfaces. The key factor for the ordering behavior within the first molecular layer on a metal surface and changes therein with increasing distance to the surface by growing additional layers on top, is mainly defined by the ratio of the strength of inter-molecular to molecule-metal interactions.

An approach to clearly pose this problem is to examine the behavior of a defined molecular system while changing a limited number of parameters. To keep the number of parameters as low as possible all experiments in this work were done under well-controlled conditions in ultra high vacuum (UHV). This includes not only the analysis, but also the preparation of organic samples. According to the previous argumentation, due to high costs of UHV-equipment and -maintenance, molecular systems investigated in this work will most probably not be directly transfered to industrial applications (even though this would be possible). Nevertheless, knowledge derived from these systems is essential for fundamental understanding of growth mechanisms and valuable for the design of new organic devices with the same or similar materials. In this work a number of novel, prototypical molecules and also prominent materials, which have been in the focus of the scientific community as well as in industrial applications, have been investigated. The goal is to analyze their growth behavior starting from mono- up to multilayers and to show how their structural and electronic properties can be influenced. For this, different approaches have been made, e.g. modifications of the molecule and introduction of a template layer. For the analysis several complementary experimental techniques were used. The local ordering of thin molecular films was investigated by scanning tunneling microscopy (STM). By this technique single molecules and point defects can be observed, which is valuable for a detailed characterization of molecular film growth. For the analysis of the long range order of molecules, low energy electron diffraction (LEED) experiments were conducted. Thick films were examined by atomic force microscopy (AFM), which is the preferred technique for investigations of samples with pronounced three dimensional growth. Additionally, the molecular orientation on surfaces was also determined by near edge X-ray absorption fine structure spectroscopy (NEXAFS). Furthermore, electronic properties were investigated by X-ray photoelectron spectroscopy (XPS) and ultraviolet photoelectron spectroscopy (UPS). With the help of these techniques information about the chemical environment as well as the valence band of the materials are derived accordingly.

For better orientation, a brief overview of the organization of this work should be given. In chapter 2 basic principles are explained. This includes fundamentals about π-conjugated systems, a brief description of their application in *organic electronics* and fundamentals about their behavior at interfaces. It covers all aspects which are important to understand the results discussed in chapter 5. The following chapter 3 describes the various experimental techniques used in this work. This is done in general form in order to get a better understanding of the fundamental aspects of the experimental methods and to highlight their potential use. Details about the appropriate experiments are given in chapter 4. There, the experimental setups used during this work, procedures of sample preparation and final processing of the data are explained. The main part of this thesis is presented in chapter 5, which at the same time introduces experimental findings and a discussion of their interpretation, including appropriate conclusions derived from the results. This chapter is divided into four parts, according to the four different molecular systems that where investigated within this work. In chapter 6 general conclusions and an outlook of this work will be given.

2 Basic principles

In this chapter the basic principles of organic molecules, their applications and layer growth mechanisms, will be introduced. At first the material class of conjugated organic molecules with defined π-systems is described in section 2.1. To point out further motivation for this work, applications of such systems in organic electronics will be presented in section 2.2. A discussion of their electronic properties, in particular in contact with metal substrates, will follow in section 2.3. In the end elements of the growth mechanism of organic molecular layers, especially in the context of self-assembly, which plays a crucial role for experiments done within this thesis, will be presented in section 2.4.

2.1 π-Conjugated systems

Organic molecules are build mainly of C-atoms, but often contain also heteroatoms like N-, S-, O- or F. In conjunction with organic electronics (section 2.2) the class of conjugated molecules is of special interest. Conjugated molecules are characterized by an alternation of single and multiple bonds (e.g. double). A principle explanation can be given by discussing one of the simplest systems shown in Figure 2.1a, which consists of just a single aromatic ring, named benzene.

Single carbon atoms have four valence electrons, occupying the s-state with two electrons and p_x and p_y with one electron in the ground state accordingly ($\frac{\upharpoonleft\downharpoonright}{1s}\frac{\upharpoonleft\downharpoonright}{2s}\frac{\upharpoonleft}{2p_x}\frac{\upharpoonleft}{2p_y}\frac{\quad}{2p_z}$). Bringing two carbon atoms close to each other leads to the formation of a covalent double bond (C=C) with sp^2-hybridization. This is achieved by promotion of one electron from the s-state to a p-state, which results in the formation of three sp^2-states occupied by one electron accordingly, while only one electron remains in a p-state ($\frac{\upharpoonleft\downharpoonright}{1s}\frac{\upharpoonleft}{sp^2}\frac{\upharpoonleft}{sp^2}\frac{\upharpoonleft}{sp^2}\frac{\upharpoonleft}{p}$). All three orbitals of the sp^2-hybridization lie within one plane, resulting in a planar conformation of the whole aromatic ring. This leads to the typical in-plane σ-orbitals found in conjugated organic molecules (Figure 2.1b). Electrons in

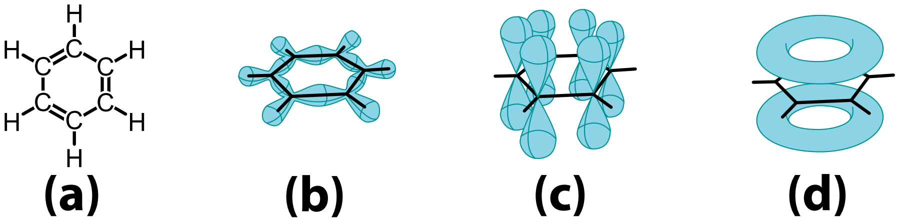

Figure 2.1: Schematics drawings of benzene. (a) Chemical structure of benzene (C_6H_6). (b) σ-bonds with hybridized sp^2-orbitals. (c) p_z-orbitals. (d) Delocalized π-orbitals (simplified).

σ-bonds remain close to their original C-atom and are therefore referred as to be localized. They represent the strongest type of covalent chemical bonding. Electrons in p-states form orbitals which stick out of the plane like lobes (Figure 2.1c). These lobes are perpendicular to the ring but parallel to each other. Two respective neighboring orbitals overlap, leading to delocalized π-orbitals above and below the plane of the ring (Figure 2.1d). Consequently, electrons in p-states are also delocalized within the according π-orbital. The character of these electrons gives rise to the properties which make conjugated organic molecules interesting for electronic applications. Also in large macro-molecules, which consist of a number of rings and conjugated chains, delocalized π-orbitals often cover the whole conjugated core.

The resulting π-states are the basis for the use of organic molecules as semiconductor material. In particular, the highest occupied molecular orbital (HOMO) and the lowest unoccupied molecular orbital (LUMO) (see Figure 2.3 and further explanation in section 2.3) are the key on the way to molecular electronics as they determine the semiconducting properties of the material. The HOMO acts as valence band whereas the LUMO is the analogon of the conduction band. Consequently, the energy difference between HOMO and LUMO represents the band gap similar to what is known from inorganic semiconductors. Based on these semiconducting properties, electronic devices made of conjugated organic molecules are build as described in the next section.

2.2 Organic Electronics

A lot of effort has been spent on semiconducting organic molecules in the last years. The main motivation of the work on this topic is their potential use in organic electronics. It has been shown that quite a number of electronic

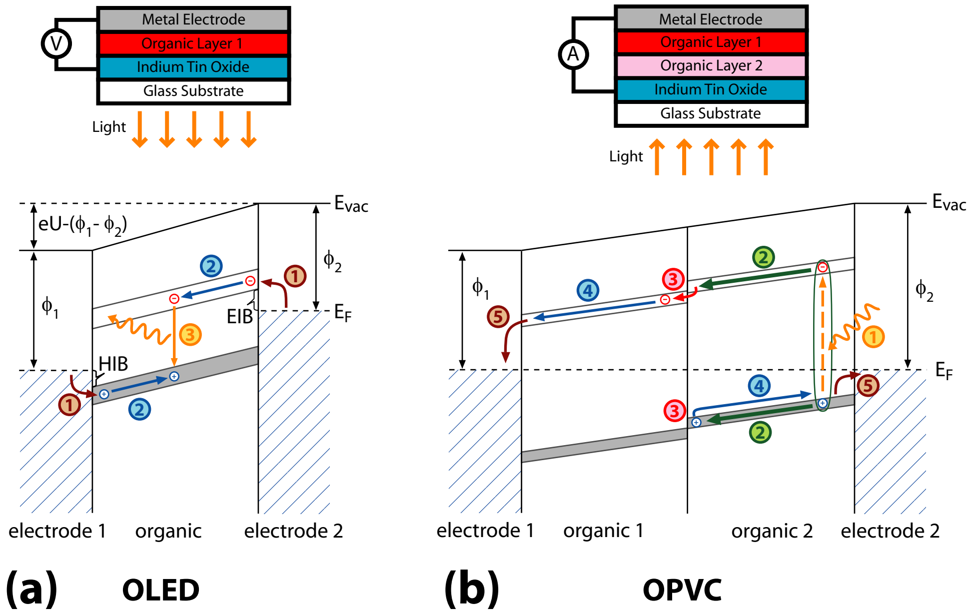

Figure 2.2: Schematic drawings of the layered structure (top) and according energy level diagram (bottom) for (a) a single layer organic light emitting diode and (b) a double layer organic photovoltaic cell.

device types based on organic materials can be realized. This includes for example organic light emitting diodes (OLED) [14], organic photovoltaic cells (OPVC) [15] and organic field-effect transistors (OFET) [16]. The basic principle of their function will be given in this section, selecting a simple OLED and OPVC as example. In Figure 2.2a a schematic drawing of a single layer OLED is shown. At the top the according principle layered structure is displayed. In this simple case an organic material is sandwiched between two electrodes. Because the organic layer is the active material in the device, one of the electrodes has to be transparent in order to extract light. To achieve this, today usually a thin layer of indium tin oxide (ITO) is applied to a glass substrate which provides reasonable conductivity as well as transparency at the same time. The other electrode is usually composed of a metal. Depending on the electronic alignment of all three materials, light may be generated by such a structure by applying a voltage to the electrodes. This process can be explained by the energy level diagram shown in Figure 2.2a. As first step ① an electron has to be injected from *electrode 2* into the LUMO and a hole from *electrode 1* into the HOMO. Therefore, the electron has to overcome the electron injection barrier (EIB) and the hole the hole injection barrier (HIB), accordingly (cf. Figure 2.3 and discussion in section 2.3). This is achieved either thermally, by tunneling through the barrier or by phonon-assisted hopping [17]. Once appropriate charge carriers are injected, they will travel towards the opposite electrodes ② due to the potential drop across the organic material. If the two charges get close to each other, they will form an exciton with a certain probability, which will eventually recombine by emitting a photon ③. The quantum efficiency η_Q of an OLED, which is the number of emitted photons per injected electron, is given by [18]:

$$\eta_Q = \gamma \cdot \eta_{ex} \cdot \eta_{pl} \cdot \eta_{oc} \tag{2.1}$$

Here, γ presents the ratio of injected electrons and holes, η_{ex} the proportion of excitons that can decay radiatively, η_{pl} the efficiency of radiative decay and η_{oc} the efficiency of light out-coupling, which is the proportion of photons actually leaving the device. Since the power efficiency η_P of the device is proportional to η_Q, optimizing the quantum efficiency is of substantial importance. For example, the parameter γ has a maximum value of 1, which stands for one electron per hole. It is influenced by the injection barrier height and the charge-carrier mobility. Consequently, the injection barriers at the organic-electrode interfaces (see section 2.3) need to be minimized. Over the years, numerous strategies have been developed in order to optimize all of the mentioned contributions to the quantum efficiency [18]. It turned out that multiple layers of organic molecules are needed to achieve the best results.

A simple example with already two organic material layers is given in Figure 2.2b: the OPVC. In principle, the process in an OPVC is reversed compared to an OLED but the materials actually needed in an OPVC and optimization of energy level alignment makes a huge difference. At the top again a sketch of the layered structure is shown, which now introduces a second layer of an organic material. The HOMO and LUMO of the two materials are chosen such that their energy levels are slightly shifted against each other as can be seen in the energy level diagram (bottom of Figure 2.2b). In the initial state of the device no voltage appears between the two electrodes, where in case of an OPVC the consumer is connected. The initial step ① in this case is the generation of an exciton by absorbing a photon, in this example in *organic 2*. With a certain probability the exciton will travel towards the interface between the two organic materials ②. If the interface is reached within the lifetime of the exciton, it will dissociate into an unbound electron and a hole ③. At this point the dissociation process is preferred over further existence of the exciton due to the energy gain for the electron when hopping into the neighboring, deeper lying LUMO. In contrast, the hole will stay in the higher lying HOMO. Once charges are dissociated, they will travel towards the according electrodes ④ where they are able to enter ⑤ and generate a detectable current between the two electrodes which can be used to operate a consumer. The quantum efficiency η'_Q of an OPVC is found to be [19]:

$$\eta'_Q = \eta_a \cdot \eta_{ed} \cdot \eta_{ct} \cdot \eta_{cc} \tag{2.2}$$

with the absorption efficiency η_a, the exciton diffusion efficiency η_{ed}, the charge transfer efficiency η_{ct} and the charge collection efficiency η_{cc}. These four contributions describe the efficiencies for the according steps (①-③ and ⑤) explained before. Similar as before, the properties of the organic materials have to be tuned in order to maximize the quantum efficiency. For example, maximizing the crystallinity of the organic layers improves the efficiency of exciton diffusion (η_{ed}) and charge collection (η_{cc}), due to minimized defect density. Furthermore, the charge collection is influenced by the injection barrier heights again.

Apart from today's organic electronic devices having a much more complex structure than what has been discussed here, the main principles remain the same as described above. For efficient injection of charge carriers, a defined alignment of all energy levels is crucial. Therefore, knowledge about the electronic structure and energy level alignment at interfaces is very important. Additionally, the efficiency of charge transport within the organic material plays a fundamental role. Due to the low polarizability of organic materials, free charges will instantly form polarons which can be regarded as the free charge carrier in organic materials. Polarons can be described like electrons with an higher effective mass. In amorphous materials charge transport from one molecule to another is usually achieved by hopping. This process again is induced thermally or realized by tunneling. To overcome this limitation a highly ordered structure without any defects and with a continuous band due to orbital overlap between adjacent molecules would be desired. In this context the controlled growth of molecular layers plays a crucial role and will be discussed in section 2.4. Special attention has to be given to interfaces between organic materials and metal electrodes, which are used as contacts. The interaction of molecules with the electrode material often has a high impact on the formation of ordered structures and its electronic properties and is often the bottleneck for efficient charge injection.

2.3 Organic-metal interfaces

As already mentioned in the previous section, organic layers in organic electronics are usually contacted by metal electrodes. The resulting organic-metal interfaces found in the devices play an important role for the efficiency

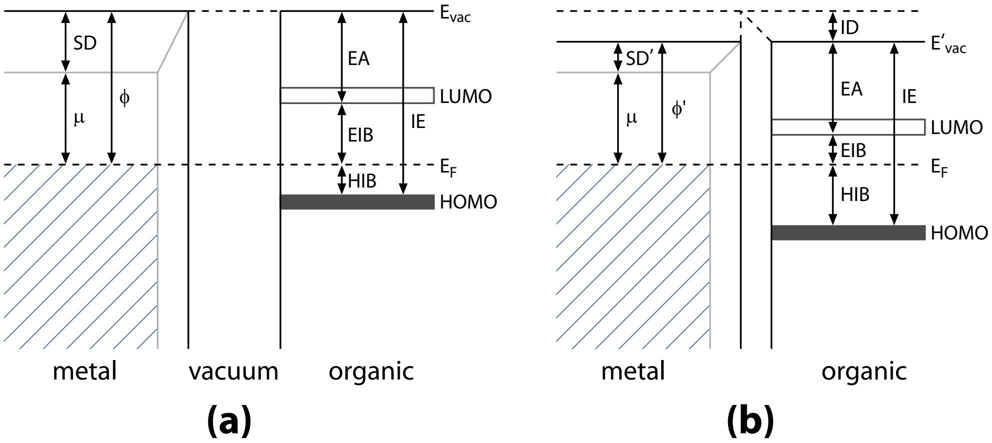

Figure 2.3: Schematic energy levels of a metal and an organic material (a) separated and (b) in contact with each other (assuming weak interaction between the metal and the organic material, i.e. physisorption described in section 2.4.1).

of the whole device (see equations in section 2.2). An overview of the resulting energy level diagram in case of a single and double layer structure has already been presented in Figure 2.2. Now, the focus will be on the interface between a metal electrode and an organic material. In Figure 2.3a the energy levels of both materials separated from each other are shown, while in Figure 2.3b the energy levels of both after contact are presented (assuming weak organic-metal interaction). The HOMO and LUMO in conjugated organic materials as counterparts of valence- and conduction-band in inorganic semiconductors were already introduced. For the discussion of electronic properties, several additional parameters have to be defined. First, the vacuum level E_{vac} defines the minimum potential energy of a free electron which is not in a bound state of the molecule or solid state material. Additionally, the Fermi-level E_F is the energy up to which all states of a metal are occupied by electrons at absolute zero temperature. Referring to Figure 2.3 the work function ϕ is then simply the energy difference between E_{vac} and E_F. These definitions do not only apply for metals, but also for semiconducting, in particular organic, materials, even though the Fermi level is not directly detectable in these materials, because it is located in the gap between HOMO and LUMO. In organic materials several additional parameters are of interest. The electron affinity (EA) of an atom or molecule is the amount of energy required to detach an electron from a singly charged negative ion. In a solid state material, this refers to the energy difference between

LUMO and E_{vac}. Moreover, the electron injection barrier (EIB) is the energy difference between LUMO and Fermi energy. Thus, it represents the energy needed to inject an electron from the continuum of states of a metal into the LUMO. Analogous, the hole injection barrier (HIB) is the energy difference between the Fermi level and the HOMO, referring to the energy needed to inject a hole from the metal into the HOMO, which of course means to move an electron in the opposite direction. The minimum energy required to eject an electron from the HOMO into vacuum is called ionization energy (IE).

When electronic properties of organic-metal interfaces were first explored it was expected that they follow the rules of commonly known inorganic semiconductor-metal interfaces. There, the behavior at the interface can be predicted following the simple rule of vacuum level alignment, which is known as the Schottky-Mott limit. In this case, the EIB and HIB can be easily precalculated once the properties of the separated constituents are known (Figure 2.3a). In fact it turned out that the situation is far more complex at the organic-metal interface. It was discovered that usually an interface dipole (ID) is formed leading to a shift of the vacuum level compared to the separated constituents [13] (Figure 2.3b). The interface dipole is caused by the rearrangement of the electron density distribution at the metal surface and on the molecules due to the interaction of molecules with the metal. This includes weak (physisorption, see section 2.4.1) as well as strong interactions (chemisorption, see section 2.4.2). A qualitative picture of the interface energetics in case of weak organic-metal interaction is shown in Figure 2.3 and will be discussed now. At closer inspection of the metal work function ϕ, a simple description of the vacuum level shift can be found [18]. The work function is composed of two parts. The first part is the bulk chemical potential μ which has its origin in the lowering of energy for atoms bound into a regular lattice. The second part is a surface dipole (SD) formed at the surface of the metal. The surface can be considered as a defect of the bulk crystal because the periodicity of the lattice is broken in at least one direction. Electrons which were involved in bonds in the bulk in this direction are now able to enter other bonds. In order to minimize the surface energy, this often results in the appearance of surface reconstructions. Moreover, electrons will usually spill out into vacuum, generating a surface dipole. Therefore, the work function ϕ is the sum of both parts. Now, by putting molecules onto the surface this dipole will be modified. Even for nonpolar molecules a lowering of SD can be observed. Due to the Pauli repulsion between electrons of the molecule and the metal at the interface, electrons which have been spilled out of the surface are now ‘pushed’ back into the metal. Therefore, this effect is often called the ‘push-back effect’. In case of polar molecules or molecules which are polarizeable the SD may also be further decreased or increased, depending on the direction of the molecular dipole. Thus, everything that happens when adding molecules to the metal surface is changing the metal surface dipole rather than creating an interface dipole. Consequently, the work function of the metal is changed to ϕ' according to the change in SD and the vacuum level is aligned accordingly. As a result HIB, EIB and IE of a molecule are significantly different in contact with a substrate than predicted from its bulk properties (Figure 2.3). Additionally, these properties vary depending on the substrate material which is used because of different surface properties. Usually, the properties have to be discovered experimentally for every single molecule-substrate combination, which is one subject of this work.

One concept to evaluate whether the Schottky-Mott limit in a particular system holds, is to determine the slope parameter S, given by [20]:

$$S = \frac{\mathrm{d}E_F}{\mathrm{d}\phi} = \frac{1}{1 + 4\pi e^2 D(E_F)\delta/A} \tag{2.3}$$

where e is the elementary charge, $D(E_F)$ the induced density of states at the Fermi energy E_F, δ the distance between the molecule and the substrate and A is the interface area of the molecule. Consequently, the degree of pinning at the interface can be characterized by the dependence of the Fermi level position, and thus the hole injection barrier, on the metal work function ϕ. The slope parameter ranges from 0 to 1. At $S = 1$ the Fermi level is free to move within the gap (Schottky-Mott limit). A value of $S \neq 1$ indicates the existence of interface dipoles. The border case of $S = 0$ denotes the Fermi level is pinned at one point in the gap regardless of the metal work function (strict Fermi level pinning). By plotting the measured HIB of a molecule in combination with different metal substrates versus the according metal work function, the slope parameter can be determined from fitting the resulting data points.

2.4 Elements of organic layer growth

The ordering within an organic film has a significant impact on its electronic properties. Especially, highly ordered structures are of great interest. In such structures the defect density is notably low which improves the charge transport by increasing the charge-carrier mobility. Therefore, investigations of the ordering behavior within the bulk crystal and at interfaces between different materials are vitally important. Especially, at the organic-metal interface the alignment and ordering of molecules can be considerably different from that of the bulk structure. Many molecules show the tendency to arrange in ordered structures on surfaces without the influence of external sources, which is referred to as self-assembly of molecules on surfaces. The resulting structure lowers the overall energy of the molecular layer on the surface and is therefore thermodynamically stable. Interestingly, the defect density within self-assembled structures is considerable low due to the high order. Most of the molecular structures presented in this work are formed by self-assembly at surfaces.

The key factor which drives the ordering behavior is the interaction strength. In particular, the ratio between the inter-molecular and the molecule-metal interaction strength determines the formation of different structures at the interface compared to the bulk, which consequently also affects the electronic properties. General interaction types of the molecule-metal interaction are physisorption and chemisorption which are described in the following two sections (section 2.4.1 and section 2.4.2). Usually, the inter-molecular interaction is rather weak and can be described in the same way as physisorption (section 2.4.1). Depending on the interaction ratio between the inter-molecular and molecule-metal interaction, three different growth modes are observed, which will be discussed in section 2.4.3.

2.4.1 Physisorption

Physisorption, the short term for physical adsorption, describes weak interactions between the adsorbing molecule and the substrate as well as between two molecules. A major contribution to physisorption comes from van der Waals interactions, but also includes long range electrostatic as well as short range repulsive forces. Usually, physisorption dominates in long range interactions. The energy gain upon physisorption is typically lower than the energy needed to break a bond within a molecule [21]. Consequently, physisorption retains the chemical structure of a molecule. Even so, the weak interactions might still lead to distortions of the molecule.

The origin of van der Waals forces are dipole-dipole interactions of polarized or polarizable molecules and substrate surface atoms. The following description will be given for the example of two molecules, but is also valid for molecule-substrate interactions. In principle three different cases can be considered. In the first case the two molecules are assumed to already have intrinsic permanent dipoles, e.g. caused by an uneven distribution of electrons within the molecule such as found in the water molecule. If the dipoles are called μ_1 and μ_2 and their distance is r, the potential energy V between them is as follows:

$$V(r) = \frac{\mu_1 \mu_2 f(\theta_1, \theta_2, \Phi)}{4\pi\epsilon_0} \cdot \frac{1}{r^3} \tag{2.4}$$

with the electric constant ϵ_0 and function f, which depends on the angles $\theta_{1,2}$ between the line joining the dipoles and the axis of the respective dipole and Φ which is the azimuthal angle between the dipoles [22]. This equation is valid for dipoles which are fixed in orientation. If these dipoles are free to rotate, the potential modifies to:

$$V(r) = -\frac{2\mu_1^2\mu_2^2}{3(4\pi\epsilon_0)^2kT} \cdot \frac{1}{r^6} \tag{2.5}$$

which is then also dependent on the temperature T. This is also known as the Keesom interaction [21]. Furthermore, in the second case, two molecules are also able to interact if just one of them has a permanent dipole μ_1. This molecule can then induce a dipole μ_2' in the other one, which causes an interaction between the dipoles. Consequently, it is called the dipole-'induced-dipole' interaction. The induced dipole will follow the inducing dipole immediately, resulting in a temperature-independent potential. For the potential energy one finds:

$$V(r) = -\frac{\alpha_2\mu_1^2}{4\pi\epsilon_0} \cdot \frac{1}{r^6} \tag{2.6}$$

with the polarizability volume α_2 of the second molecule [21]. Finally, in the last case, two molecules which have no permanent dipole at all are also able to interact in this way, known as the 'induced-dipole'-'induced-dipole' interaction. Since electrons are not fixed in reference to the positive core of their molecule, but will travel within their orbitals, the molecule has a fluctuating dipole. On average the molecule is still not polarized, but taking a snapshot of its configuration will reveal a temporary dipole. Hence, two molecules will always show weak attractive interaction because of the coupling of their transient dipoles, following a potential energy of:

$$V(r) = -\frac{3}{2}\alpha_1\alpha_2\frac{I_1 I_2}{I_1 + I_2} \cdot \frac{1}{r^6} \tag{2.7}$$

which again involves the polarizability of the two molecules $\alpha_{1,2}$ and additionally the respective ionization energies I_1 and I_2 [21]. Apparently, equation 2.5, 2.6 and 2.7 show the same distance dependence of $V \propto r^{-6}$. They are the most prominent contributions to the van der Waals interaction. Taking into account also short ranged repulsive forces, caused by the Pauli principle and Coulomb repulsion, the interaction is often expressed in general by the Lennard-Jones-Potential:

$$V(r) \propto \left[\left(\frac{r_0}{r}\right)^{12} - \left(\frac{r_0}{r}\right)^{6}\right] \tag{2.8}$$

where r_0 is the separation between the molecules at which $V = 0$. The first term takes into account the short range repulsion and the second term the long range attractive forces. Although this is a simplified model, it has been successfully used for modeling of physisorption processes of organic molecules on surfaces [23].

2.4.2 Chemisorption

Chemisorption, which is the abbreviation for chemical adsorption, describes interactions which involve the formation of chemical bonds. Depending on the extent of electron transfer, chemisorption has either predominant covalent or ionic character. Ionic bonding includes a pronounced charge transfer between molecule and substrate, whereas in covalent bonds electrons are shared between them. The typical energy gain in chemisorption is about ten times higher than that of physisorption [21]. Therefore, chemisorbed molecules may undergo chemical modifications. In return the interaction has much shorter range than found in physisorption, but often also reduces the distance between substrate and molecule because of strong bonding. Molecules can be intentionally designed including special reactive parts to force them to show chemisorption on selected surfaces. This way very stable adsorption layers can be achieved, but also the electronic properties may be significantly altered at the interface compared to the bulk.

2.4.3 Growth modes

Depending on the ratio of the interaction strength among the molecules themselves and between molecule and substrate, different growth modes occur. First of all, one can make a principle consideration. Conjugated molecules with oriented molecular π-system, such as rod-like or disc-shaped molecules, show the tendency to have different orientations on the surface depending on the type of substrate. When adsorbed on metal substrates they tend to arrange into flat lying layers with their molecular π-orbitals perpendicular to the surface plane (Figure 2.4a). The origin of this behavior is found in a rehybridization of molecular orbitals with substrate orbitals [24]. This takes place only within the first monolayer of the adsorbate on the substrate. In contrast to this phenomenon, adsorbing the same molecules onto a weakly interacting substrate like SiO_2 often leads to upright standing molecules (Figure 2.4b) [25]. The exact angle formed between the long molecular axis and the substrate plane is strongly dependent on the inter-molecular interaction.

Apart from the former principle considerations, three different motifs have been found for thin film growth. Which of them occurs is commonly

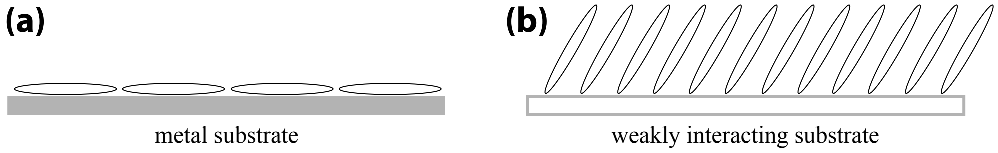

Figure 2.4: Schematic drawing of stick-like molecules on different substrates. (a) Flat lying molecules on a metal substrate. (b) Inclined molecules on a weakly interacting substrate.

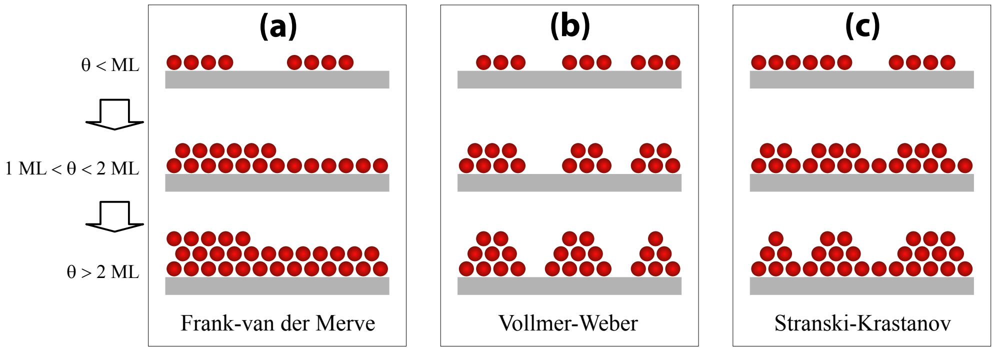

Figure 2.5: Molecular assembly according to the different growth modes depending on the film thickness θ. (a) Layer-by-layer or Frank-van der Merwe growth. (b) Island or Vollmer-Weber growth. (c) Layer-plus-island or Stranski-Krastanov growth.

determined by the ratio of the inter-molecular interactions compared to the molecule-substrate interactions. An illustration of the different growth modes is found in Figure 2.5. In detail, the following modes are distinguished:

(a) **Frank-van der Merve growth:** In the first motif the interaction between molecule and substrate is stronger than between the molecules. As a result, molecules will form a completed layer on the surface before they start filling the second layer. The adsorbed molecular layer may still serve as a strong interacting template due to the modified properties caused by the interaction with the substrate. Then again the second layer will be completed prior to growing in the next higher one and so on. Therefore this mode is also called *layer-by-layer growth*. Main growth in this mode proceeds in two dimensions. As it turned out, this growth motif is very rarely found for organic-metal interfaces, because of the strong attenuation of the substrate interaction with increasing layer thickness.

(b) Vollmer-Weber growth: The other extreme is the case for which the interaction between molecules is stronger than with the substrate. Additional molecules will then just try to attach on existing clusters of already adsorbed molecules. Thus, immediately multilayers begin to form. Clusters will grow in width as well as in height, leading to three dimensional growth of islands. Therefore this mode is often just called *island growth*. Island growth is a phenomenon which is very often found for molecules that exhibit only weak interaction with the substrate.

(c) Stranski-Krastanov growth: The last mode is an intermediate process of the two modes discussed before. The interaction strength between a molecule and the surface weakens with increasing distance of the molecule from the surface. In particular, the surface is efficiently screened from the molecule if it lies on top of already completed molecular layers. Hence, even if completed layers are formed according to the Frank-van der Merve growth there is a critical layer thickness at which the inter-molecular interaction will dominate. Then island formation just like in Vollmer-Weber growth will dominate the further growth process. This often happens already after the first or second completed monolayer (ML). Sometimes it is called *layer-plus-island growth*. This growth motif is often observed for molecular systems on metal surfaces, because the molecule-metal interaction strength within the first layer is often strong, but significantly lowered already at the second layer.

The former described growth modes are very important for investigations of thin films presented in this work. In case of pronounced island growth direct observation with scanning tunneling microscopy (section 3.1) is often difficult. Predictions about the growth motif can frequently be derived already from electron spectroscopy experiments (section 3.4). These methods will be explained in detail in the following chapter.

3 Methods

In this chapter a brief overview of the experimental techniques used in this work will be presented. For structural analysis of thin molecular films scanning tunneling microscopy (section 3.1) in conjunction with low energy electron diffraction (section 3.3) was used. Thick molecular films were analyzed by atomic force microscopy (section 3.2). Electronic properties of samples were investigated using photoelectron spectroscopy (section 3.4.1). Furthermore, for the determination of the molecular orientation near edge X-ray absorption fine structure spectroscopy (section 3.4.2) as well as the interpretation of spectral features in photoelectron spectroscopy (section 3.4.1) were used.

3.1 Scanning tunneling microscopy

One very important technique used in this work for the analysis of thin molecular films was scanning tunneling microscopy (STM). This method was developed by Binnig and Rohrer in the early eighties of the twentieth century, for which they were awarded the Nobel Prize in Physics in 1986 [26, 27], and had a high impact on the whole field of surface science. Today it represents a rather common technique, which is still one of the most important ones for direct observation of structures at the nano-scale. Basic principles of STM will be discussed briefly in the following subsections.

3.1.1 Quantum tunneling

Quantum tunneling is a pure quantum mechanical effect. It describes the ability of a particle to overcome a potential barrier even though, from the classical point of view, the energy of the particle is not sufficient to do so. One main principle of quantum mechanics is the dualism to describe all matter either as a particle or as a wave. Therefore, from a quantum mechanical point of view a neat explanation is to discuss the particle as a wave function

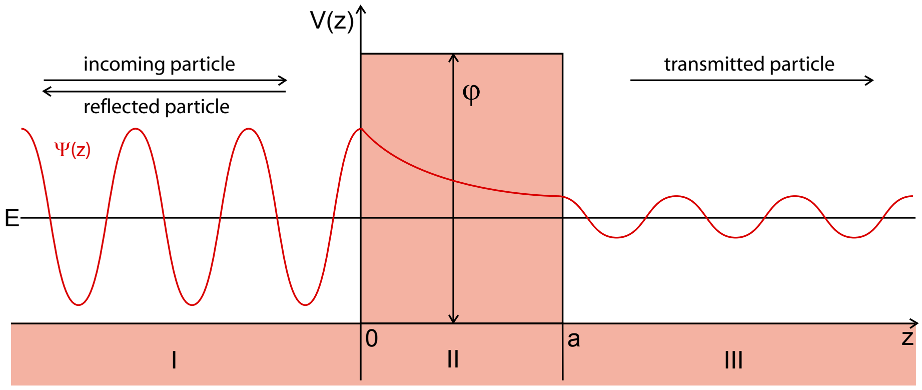

Figure 3.1: Schematic model of an one-dimensional tunneling barrier with rectangular potential wall. The wave function of the particle is sketched by the red line.

which fulfills the Schrödinger-equation (equation 3.1). In this case no certain place for the particle can be specified, but the probability to find the particle in the considered interval has to be declared. This probability is defined as square absolute value of the wave function and is therefore proportional to the square of the amplitude. If the wave function enters the area of a potential barrier which exceeds the energy level of the wave, it will decrease exponentially within this area. For small barriers the wave function may still have a non-zero amplitude at its endpoint and hence a non-zero probability to find the particle. A sketch of this scenario is shown in Figure 3.1.

An alternative explanation of this effect can be given on basis of the Heisenberg uncertainty principle. It links the uncertainty of energy ΔE with the uncertainty of time Δt using the Planck constant h via $\Delta E \Delta t \geq h/4\pi$. Within the short interval of time uncertainty the particle can 'borrow' some energy from its environment to overcome the barrier and then releases this energy again. As long as the Heisenberg uncertainty is fulfilled the fundamental principle of conservation of energy is not broken.

Already this simple model explains the main principle of scanning tunneling microscopy. There the potential barrier is simply given by the spacing between a very fine metallic tip, which is the probing tool, and the conducting sample surface that should be investigated. A brief theoretical description of the tunneling effect will be given in next subsections.

3.1.2 One-dimensional quantum tunneling

A good starting point is always the simplest model. Hence, at first tunneling in one dimension through a rectangular potential barrier as shown in Figure 3.1 will be discussed. The theoretical description will be given considering the tunneling electron as a wave function ψ, which has to fulfill the Schrödinger equation:

$$H\psi = -\frac{\hbar^2}{2m}\frac{d^2\psi}{dz^2} + V(z)\psi = E\psi \tag{3.1}$$

Here, m represents the mass, E the energy of the particle, z the space coordinate, H the Hamiltonian and $\hbar$ the reduced Planck constant (h divided by 2π). The potential barrier is taken into account by the space dependent function $V(z)$. To achieve a rectangular barrier the potential is set $V(z) = \varphi$ within the interval $0 \leq z \leq a$ and $V(z) = 0$ outside. Considering the incoming, reflected and transmitted wave, the ansatz in the appropriate regions (cf. Figure 3.1) is chosen as follows [28]:

$$\text{Region I:} \quad \psi_1 = e^{ikz} + Ae^{-ikz} \quad \text{with} \quad k^2 = \frac{2mE}{\hbar^2} \tag{3.2}$$

$$\text{Region II:} \quad \psi_2 = Be^{-\kappa z} + Ce^{\kappa z} \quad \text{with} \quad \kappa^2 = \frac{2m(\varphi - E)}{\hbar^2} \tag{3.3}$$

$$\text{Region III:} \quad \psi_3 = De^{ikz} \tag{3.4}$$

The solution has to preserve the continuity of the wave function ψ as well as that of its derivative $\frac{d\psi}{dz}$ at points $z = 0$ and $z = a$. Then the unknown parameters A, B, C and D can be determined. The tunneling probability is described by the transmission coefficient T, which is equal to the absolute square of the transmitted amplitude $|D|^2$. Under the assumption of a strongly attenuating wave function within the barrier ($\kappa a \gg 1$) one finds [28]:

$$T(E) = \frac{16k^2\kappa^2}{(k^2+\kappa^2)^2} e^{-2\kappa a} \sim \exp\left(-\frac{2}{\hbar}\sqrt{2m(\varphi - E)}a\right) \tag{3.5}$$

Already in this simple model fundamentals of quantum tunneling are included. An exponential dependence of the tunneling probability on the width a and the square root of the barrier height φ is found.

A more general solution for potentials of arbitrary shape $\varphi(z)$ is derived using the WKB-approximation, named after its developers, the physicists Wentzel, Kramers and Brillouin. It provides a solution of the one-dimensional Schrödinger equation. The use of this approximation is valid when the de Broglie wavelength of the particle is small compared to the length scale at

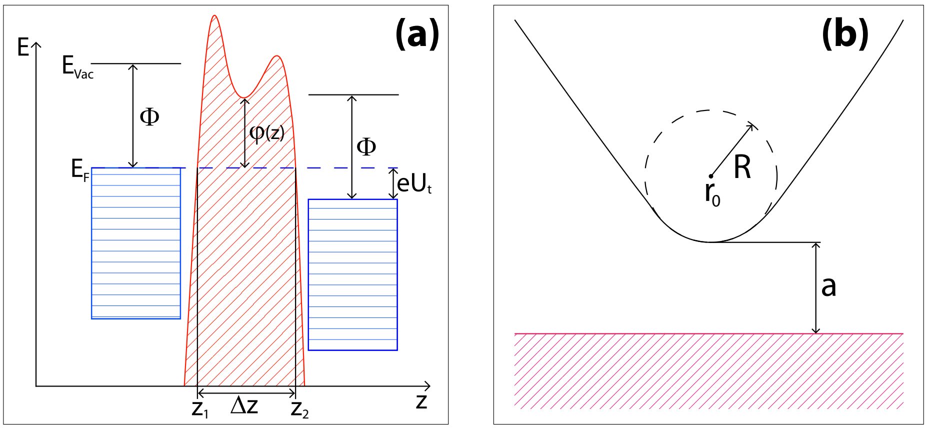

Figure 3.2: (a) Model of quantum tunneling as discussed by Simmons [29]. Displayed are the density of states of two identical electrodes with work function Φ, which are separated by a potential $\varphi(z)$. By applying a voltage U_t the Fermi energies E_F of the electrodes are shifted against each other. (b) Geometry of the tunneling tip according to the model of Tersoff and Hamann.

which the potential $\varphi(z)$ varies. An explicit theoretical calculation of the scenario found in STM was given by John G. Simmons in 1963 [29] (long time before the invention of STM). His formalism describes the particle flow between two identical metal electrodes which are separated by a potential $\varphi(z)$ and energetically shifted against each other by the tunneling voltage U_t. A sketch of this scenario is shown in Figure 3.2a. In this model z_1 and z_2 represent the classical reversal points of the potential whereas $\Delta z = z_2 - z_1$ would be equal to a in case of the rectangular barrier of the previous example. For simplification the potential $\varphi(z)$ can be substituted by an average barrier height $\bar{\varphi} = \frac{1}{a}\int_{z_1}^{z_2}\varphi(z)dz$. In conjunction with the WKB-approximation, while assuming an experimental temperature of 0 K (which is a suitable approximation in this case, because the Fermi temperature is much higher than the temperatures used in the real experiments) and the use of only small voltages ($eU_t \ll \bar{\varphi}$), the general expression of the one-dimensional tunneling current density is found to be:

$$J_z \approx \frac{e^2\sqrt{2m}}{4\pi^2\hbar^2}\sqrt{\bar{\varphi}}\frac{U_t}{\Delta z}\exp\left(-\frac{2}{\hbar}\sqrt{2m\bar{\varphi}}\Delta z\right) \tag{3.6}$$

In this formula all fundamental characteristics of the tunneling current are found:

- As already mentioned for the tunneling probability an exponential dependence from barrier width Δz and hence distance of the two electrodes is found. In a scanning tunneling microscope these electrodes are provided by the sample surface on the one hand and the probing tip on the other hand. Quantitative analysis of (3.6) shows that already an increase of the tunneling distance a of only 1 Å leads to a decrease in the tunneling current by a factor of 10. Hence, only the lowermost atom of the tunneling tip contributes to the tunneling current.

- Also the exponential dependence from the square root of the average barrier height $\bar{\varphi}$ is found. This is very important for the experiments. Variations in the tunneling current originate not only from height differences of the surface profile, but may be also caused by local variations of electronic probabilities of the sample.
- Taking a look at the borderline case of very small voltages, $J_z \sim U_t$ is found. This is the behavior of an ohmic resistor.

3.1.3 Three-dimensional quantum tunneling

One advantage of STM is even found in its ability to gain three-dimensional information by scanning across the surface (cf. section 3.1.4). Additionally, the tip which is used for the tunneling process has no punctual shape but rather defined three-dimensional geometry. Hence, for the description of the real experiment one has to consider the tunneling process in all three dimensions. First theoretical works on this topic were presented by Tersoff and Hamann [30, 31] shortly after the invention of the scanning tunneling microscope. This time the ansatz comes from first-order perturbation theory:

$$I_t = \frac{2\pi e}{\hbar} \sum_{\mu,\nu} \{f(E_\mu)\,[1 - f(E_\nu + eU_t)]\}\,|M_{\mu\nu}|^2\,\delta(E_\nu - E_\mu) \tag{3.7}$$

Here, $f(E)$ represents the Fermi-Dirac distribution, U_t again the applied tunneling voltage and $M_{\mu\nu}$ the tunnel matrix element between quantum state ψ_μ of the tip and ψ_ν of the sample. E_μ and E_ν are the according energies of quantum states ψ_μ and ψ_ν at the starting point apart from the tunneling contact. Using the Dirac delta function $\delta(E)$ provides conservation of energy in case of elastic tunneling. The main problem to solve equation (3.7) lies in the matrix element $M_{\mu\nu}$. This was given by Bardeen [32] as:

$$M_{\mu\nu} = \frac{-\hbar^2}{2m} \int d\mathbf{S}(\psi_\mu^* \boldsymbol{\Delta}\psi_\nu - \psi_\nu \boldsymbol{\Delta}\psi_\mu^*) \tag{3.8}$$

There an integration is found, which is done over the cross sectional area S between tip and sample. To solve this equation the wave functions ψ_μ

of the tip and ψ_ν of the sample have to be given, which is usually difficult. To overcome this problem Tersoff and Hamann approximated the tip with a sphere at position $\mathbf{r}_0$ with radius R and applied only spherical wave functions for the tip states (cf. Figure 3.2b). For modeling surface states they used Bloch waves. Furthermore, they assumed to have low temperatures as well as low voltages, which lead to a total tunneling current I_t of:

$$I_t = \frac{32\pi e^2}{\hbar} U_t \frac{\Phi^2}{\kappa^4} D_T(E_F) R^2 \rho(\mathbf{r}_0, E_F) \exp\left(2\kappa R\right) \tag{3.9}$$

with the work function Φ (for simplicity set equal for tip and surface) and $\kappa = \frac{\sqrt{2m\Phi}}{\hbar}$. Furthermore, the density of states of the tip D_T and the local density of states of the sample $\rho(\mathbf{r}_0, E_F)$ were introduced. The latter one can be written as:

$$\rho(\mathbf{r}_0, E_F) = \sum_\nu \left|\psi_\nu(\mathbf{r}_0)\right|^2 \delta(E_\nu - E_F) \tag{3.10}$$

At first glance the characteristics which were already concluded for the one-dimensional case are found. Because of $\left|\psi_\nu(\mathbf{r}_0)\right|^2 \sim \exp(-2\kappa(R+a))$ in (3.10) and applying to (3.9), the already in one dimension derived proportionality can be shown (cf. equation 3.6):

$$I_t \sim \exp\left(-2\kappa a\right) = \exp\left(-\frac{2}{\hbar}\sqrt{2m\Phi} a\right) \tag{3.11}$$

Also the ohmic resistance for small voltages can be found in (3.9). Additionally, some new characteristics appear:

- The tunneling current now depends also on the local density of states (LDOS) $\rho(\mathbf{r}_0, E_F)$ of the sample. Hence, by setting the tunneling current constant while scanning across the surface, a contour map of the surface is derived.

- Furthermore, the geometry as well as the electronic structure of the tip are affecting the tunneling current. As it turns out, the tip radius has significant influence on the lateral resolution of the scanning tunneling microscope. In case of sharp tips, which have a small curvature radius R at the end, the resolution is determined by the distance between tip and surface a and therefore the width of the tunneling barrier (equation 3.11). Instead, if a blunt tip with high radius is used, the tip radius R will determine the resolution (equation 3.9).

The model discussed here involves a couple of simplifications. For example, the assumption of using only spherical orbitals to describe the tip is in rather strong discrepancy to reality. Typical tip materials have density of states at the Fermi-edge coming mainly from d-states [33], which do not have spherical symmetry. Several alternative models were developed, which for example take into account multiple pathways for the tunneling electrons [34] and inelastic scattering on electrons and phonons [35]. A detailed discussion of these models would go beyond the scope of this work. Since the main princliples are already explained by the simple model of Tersoff and Hamann [31], it should be sufficient as theoretical description at this point.

3.1.4 Principle of scanning tunneling microscopy

Based on the tunneling effect, the aim of a tunneling scanning microscope is to derive information about the surface structure. As already explained, the tunneling process takes place between probe and sample surface, where the tunneling barrier is simply created by the spacing between both. The probe is given by a fine metallic tip. Ideally, this tip consists of only one atom at its very end. The tunneling current I_t is then generated by applying a tunneling voltage U_t between tip and sample. Because the tunneling current is very small, the tip has to approach the surface down to a distance of just a few Ångströms (here, this refers to z-direction). Thanks to the exponential dependence of the tunneling current on the width of the tunneling gap (cf. section 3.1.2), the current becomes detectable at such small distances. In order to realize such a close approach controlled and precisely, a very accurate drive for positioning and a feedback circuit to stabilize the tip is needed. It was found that piezo ceramics are able to perfectly fulfill the task of precise positioning. Piezo ceramics have the special characteristic to stretch in dependence of an applied voltage. This opens the possibility to change their dimensions in the range of sub-Ångströms. Furthermore, to regulate the distance between tip and sample within several Ångströms, an automated feedback between measured tunneling current and stretching of the piezo, i.e. applied voltage to the piezo, is needed. This is done by the so called feedback electronics.

Measurements on tunneling contacts at just one fixed point were done already long before the invention of tunneling scanning microscope. As already indicated by its name, the specific strength of this instrument lies in the ability to derive information about a whole area of the surface by scanning over it. To achieve this, the tip is moved within a specified area line by line across the surface. Usually the tip is driven along the x-direction, detecting the tunneling current at a defined number of points and returns to its original position after completing one line. Then the position is changed by moving the tip by a defined step in y-direction and scanning in x-direction

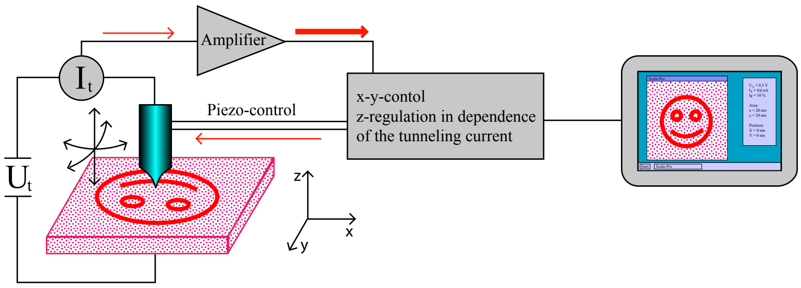

Figure 3.3: Principle sketch of a scanning tunneling microscope. The sample is painted in red and the cyan tube represents the tip. Surrounding symbols show the operation principle of the feedback circuit. The resulting signal is visualized on the screen sketched on the right.

is repeated. This way a lateral image of the tunneling current $I_t(x, y)$ is created. The specific characteristics of these images are found in the sensitive dependence of the tunneling current on the width of the tunneling barrier (according to equation 3.11). Hence, also tiny changes in the distance between tip and surface lead to significant changes of the measured tunneling current. Even the outline of two adjacent atoms can be detected. For positioning the tip in x- and y-direction on the length-scale of atoms, additional piezo-ceramics are used. In combination with a feedback electronics the required precision is achieved. A principle sketch of the instrument is shown in Figure 3.3. When interpreting measured data special attention has to be given to the fact that the tunneling current is determined not only by the barrier width but also by the local electronic structure (LDOS) of the sample as discussed before (section 3.1.3).

3.1.5 Operation modes

The use of the feedback electronics as described in the former section allows to operate the scanning tunneling microscope in two different general modes. In each measurement the user defines the tunneling voltage as well as an initial tunneling current. This parameter pair is called setpoint. To start the tunneling process, at first the tip automatically approaches the surface until the setpoint is reached. Now, one possibility is to disable the feedback electronics, leaving the tip at its initial height. When scanning lateral across the surface in this mode, only the tunneling current is altered according to changes in the width of the tunneling gap, i.e. height differences, and variations in the LDOS. Consequently, this mode is called *constant height mode*.

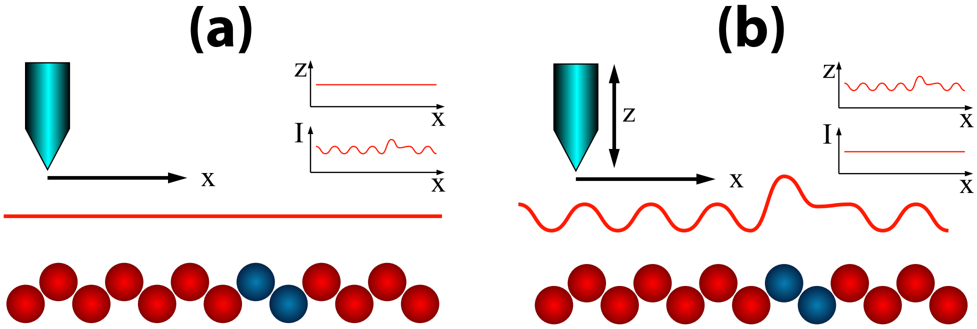

Figure 3.4: Operation modes of the scanning tunneling microscope. The surface is sketched as a chain of balls with alternating height, where blue balls present points with increased tunneling probability due to different LDOS. (a) Constant height mode. (b) Constant current mode.

Surface features are recorded in the current images within this operation (Figure 3.4a). Since the only task of the electronics in this mode is to drive the tip laterally, this movement can be done comparably fast. An advantage of fast scanning lies in its better suppression of image distortion caused by thermal drift. In return the tip is not able to react on height changes of the surface, which may result in loosing the contact or even crashing into the surface.

The other possibility is to continuously adjust the tip height in order to remain at the setpoint while lateral scanning. This would lead to a completely constant tunneling current. Consequently, this mode is called *constant current mode*. In this case all surface features are found in the height images (Figure 3.4b). Advantageous in this mode is the ability to image surface structures with strong corrugation, but this has to be done slowly in order to allow the electronics to adjust the tip height while moving. Therefore, the scanner drift usually leads to significant distortion of images in constant current mode.

In reality it turns out that none of both modes are strictly usable as they are defined. On the one hand the feedback electronics needs finite time to adjust the tip height, making it impossible to achieve pure constant current mode in reasonable time. Additionally, the tip easily starts to vibrate in resonance due to permanent z-stimulation by the electronics. On the other hand pure constant height mode is not recommended because the sample is never perfectly flat. Even if its corrugation is reasonably small, the surface plane is usually not perfectly parallel to the plane in which the lateral movement takes place. Therefore, the tip height has to be permanently corrected in order to avoid crashing into the surface or loosing contact to it. Hence, in real scanning tunneling microscopy a mixture of both modes is used which can be optimized by the user. Usually, height images as well as current images contain both substantial information about the surface and should be considered both. As it is highlighted in Figure 3.4 again, not only topographic but also electronic deviations of the surface influence the measured signal. In principle height images and current images in both pure modes contain the same information and it should be pointed out again, that height images are not to be interpreted as pure topographic information in general.

3.1.6 Tunneling through molecules

Apart from imaging surfaces of conducting solid state materials, also molecular adsorbates can be investigated by scanning tunneling microscopy, which is part of this thesis. In this case molecules reside inside the tunneling barrier between tip and sample surface. Also non-conductive molecules may be visualized if the local density of states of the substrate is modified by interactions between molecules and the surface. This effect was explained by a model proposed by Spong *et al.* [36]. For molecules which are polarizable or contain polarizable parts a charge displacement within the molecule can be induced by applying the tunneling voltage. The resulting dipoles may influence the substrate local density of states which can be measured. Consequently, indirect information about the adsorbate can be derived.

Alternatively, Mizutani *et al.* [37] developed a model which also explains the contrast derived from physisorbed, i.e. weak interacting, molecules (cf. section 2.4.1). By insertion of molecules into the tunneling gap, which themselves exhibit molecular orbitals, new states are introduced into the formerly empty gap. As a consequence the tunneling barrier is split into two parts. The first barrier is given by the geometrical relaxation of the molecule with respect to the substrate surface, while the second is determined by the tunneling parameters. In ground state with tunneling voltage set to zero, tip and sample Fermi-energy are perfectly aligned. HOMO and LUMO of the molecular adsorbate in the ground state are generally not symmetrical with respect to the Fermi-level (cf. Figure 3.5a). Now, if for example a negative tunneling voltage is applied to the sample, states of tip and sample will be shifted relative to each other, leading to a tunneling current (cf. Figure 3.5b). Because of the linear voltage drop from sample to tip, also the molecular states will be shifted. Once the tunneling voltage is sufficient that the HOMO faces empty states of the tip, the tunneling current increases significantly due to the increased tunneling probability (cf. Figure 3.5c). This effect is referred to as resonant tunneling. Interestingly, for the molecular states as shown

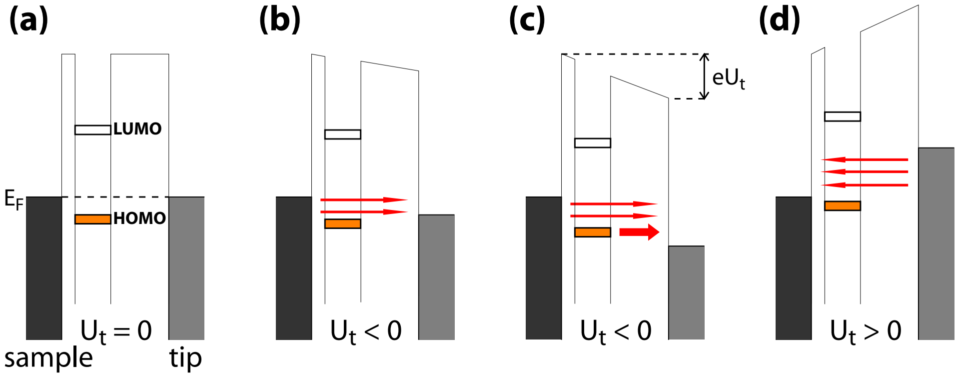

Figure 3.5: Principle of resonant tunneling through a molecular adsorbate sketched as energy level diagrams. (a) Ground state without tunneling voltage applied. (b) Small negative tunneling voltage applied to the sample. (c) By increasing the negative voltage resonant tunneling is achieved. (d) Applying of positive tunneling voltage with same absolute number as in (c) leads not to resonant tunneling due to the asymmetry of molecular states with respect to the Fermi-level.

in Figure 3.5, by just changing the voltage sign, i.e. positive sample bias, while remaining at same absolute voltage as was used in the former case, no resonant tunneling is achieved (cf. Figure 3.5d). Due to the asymmetry of the molecular orbitals with respect to the Fermi-level and also the asymmetric position of the molecule within the tunneling gap, direct tunneling into the LUMO requires a higher absolute voltage than was needed for resonant tunneling into the HOMO.

3.2 Atomic force microscopy

To overcome the limitations of STM Binnig, Quate and Gerber developed a technique which they called atomic force microscopy (AFM) [38], today also known as scanning force microscopy (SFM). In principle this technique is just an enhancement of STM. Again, a sharp tip is used to probe the sample surface down to atomic scale. But this time the tip is mounted at the end of a cantilever which acts as a spring. Bringing this tip close to the surface the cantilever will be bent by interaction forces between tip and surface atoms. To detect this bending most atomic force microscopes make use of a laser spot which is reflected by the very end of the cantilever into a position sensitive photo detector (Figure 3.6). This mechanical amplification of tip movements

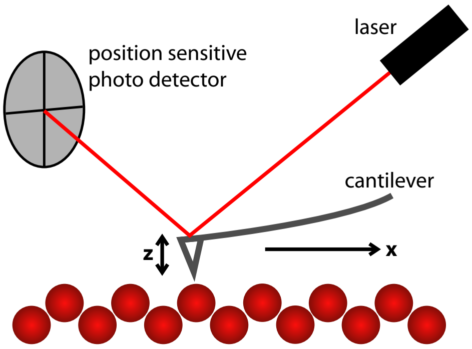

Figure 3.6: Principle sketch of an atomic force microscope. The surface structure is indicated by red balls.

enables to detect changes in cantilever bending down to sub-Ångström range. Lateral movement is accomplished in the same way as already described for STM (cf. 3.1.4). Since no tunneling is needed by this technique, one of the biggest advantages is found in the ability to probe also insulating samples. Additionally, the design of AFM usually allows to scan larger areas of the sample and still safely image surface structures and adsorbates with huge height variations. Because of these properties AFM has spread over a wide range of scientific fields, especially in biological science.

As already found for STM, also here different operation modes are possible. Either the tip is moved across the surface remaining at the initial height and detecting the bending of the cantilever or the laser spot is hold always at the same point in the photo detector by adjusting the tip height accordingly, which is recorded as a surface profile. Since the principle as well as most of the setup is similar to STM, details on how the feedback and scanning process is working can be read in section 3.1.4. The main difference lies in the generation of the feedback signal by interaction forces between tip and sample.

3.2.1 Tip-sample forces

Forces between tip and sample are the basis of AFM. Quite a number of forces are discussed in the book of Israelachvili [39], but just the most relevant should be mentioned here. Basically, these forces can be divided into *long range* forces and *short range* forces. This leads to two different operation regimes, depending on the tip-sample distance. Generally, this behavior can be theoretically described by a Lennard-Jones potential in analogy to

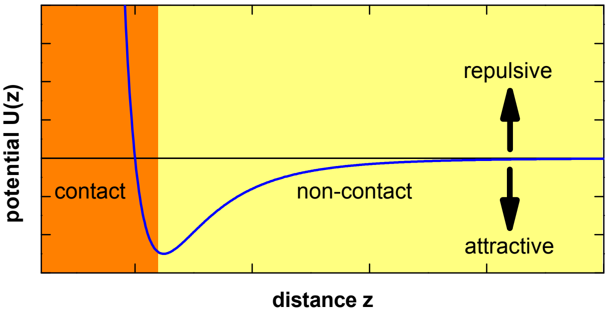

Figure 3.7: Lennard-Jones potential visualizing the distance dependence of forces between cantilever and sample for an AFM.

physisorption (cp. section 2.4.1):

$$U(z) \propto (Az^{-12} - Bz^{-6}) \tag{3.12}$$

Here, A and B represent empiric parameters and z is the distance between tip and sample. An example sketch of this potential is shown in Figure 3.7.

The first term with z^{-12} refers to forces which dominate at short distances, where mainly repulsive forces affect the tip. On the one hand coulombic repulsion occurs due to the incomplete screening of nuclear charges when the electronic clouds of two nuclei overlap. On the other hand Pauli repulsion, originating from the Pauli exclusion principle, is found. According to the Pauli exclusion principle, two electrons within same quantum state can not occupy the same orbital. Hence, the overlap of two orbitals may be prohibited leading to repulsive forces. Generally, these forces are relatively strong but also rapidly attenuated when going to higher distances above the surface. To detect these forces the tip has to be nearly in touch with the surface. Therefore, this operation is called *contact mode*.

The second term with z^{-6} represents long range forces, which have mainly attractive character. Usually this term refers to Van der Waals forces, which are significant on the scale of a few up to several hundreds of Ångströms. Again coulombic interaction may occur, leading to electrostatic forces ranging up to thousands of Ångströms. Depending on the materials involved, these forces may be attractive as well as repulsive. Since the tip in this mode will operate comparatively far away from the surface, it is called *non-contact mode*. This mode was usually used within this work to characterize samples with thick molecular films.

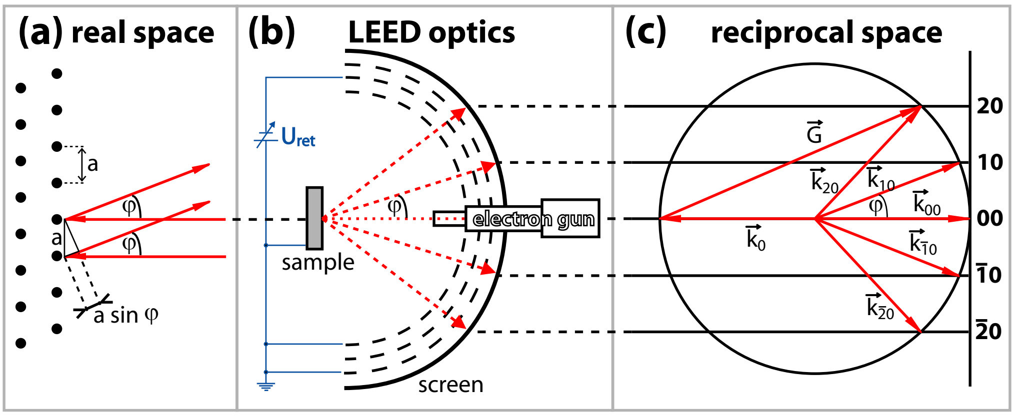

Figure 3.8: Schematic drawing of LEED optics and resulting diffraction spots. (a) Schematic electron diffraction in real space. (b) Sketch of a typical LEED optics. (c) Electron diffraction in reciprocal space constructed by an Ewald sphere.

3.3 Low energy electron diffraction

Diffraction of light at obstacles, e.g. slits or gratings, are well known since the 19th century. Effects like interference become observable when the wavelength is in the order of the size of the diffracting object. In 1924 de Broglie proposed that moving particles can be associated with a wave having a wavelength depending on their kinetic energy, which was awarded with the Nobel Prize in 1929 [40]. Hence, by choosing the right energy it is possible to observe diffraction effects on gratings as small as the atomic lattice of a solid state body. Already in 1927 Davisson and Germer published a first work on diffraction of electrons with low energy [41, 42]. Due to the lack of affordable, high quality ultra high vacuum (UHV) the further development of low energy electron diffraction (LEED) as a tool for surface analysis was delayed by more than thirty years. Up to today LEED has become one of the standard techniques to probe ordered surface structures.

A sketch of a typical LEED optics can be found in Figure 3.8b. Electrons are usually emitted thermally from a cathode in the electron gun. Inside the gun these electrons are focused to a beam with adjustable kinetic energy. The electron beam is directed perpendicular onto the sample surface where the electrons are diffracted (red dashed lines in Figure 3.8b) by the surface lattice. Reflected electrons travel through three concentrical grids onto a fluorescence screen. The first innermost grid is grounded just like the sample itself. Thus, the space between sample and first grid is free of electrical fields, allowing electrons to travel straight forward in the direction they were diffracted. At the next grid a retarding potential U_{ret} is applied. Here, electrons which were inelastically scattered at the sample surface are suppressed by increasing this voltage until they are not able to pass the grid. The third grid is set to ground potential in order to accelerate the electrons again before they hit the screen. In case of an ordered crystal surface clear spots will be visible on the screen where they can be recorded by a camera.

Spots on the LEED screen indicate points at which the incoming electron wave shows constructive interference due to the diffraction at a two-dimensional structure. The diffraction pattern can be easily constructed when described in reciprocal space. In reciprocal space a three-dimensional crystal is build by a pattern of periodic Bragg points. Because this periodicity is broken at the surface, atoms at the surface form so called Bragg rods which stick out of the surface plane. According to the Laue equation, constructive interference is obtained if the difference of the incoming wave vector $\vec{k}_0$ and the wave vector of the diffracted electron $\vec{k}_{hk}$ is equal to a vector of the reciprocal lattice $\vec{G}$:

$$\vec{k}_{hk} - \vec{k}_0 = \vec{G} \tag{3.13}$$

A simple visualization of this constraint is given by the Ewald sphere construction (Figure 3.8c). First, the incoming wave vector $\vec{k}_0$ is plotted at the point of incidence and then a circle with radius equal to the vector length and center at the starting point of the vector can be constructed. Now, every intersection point of the circle with the rods represents one possible direction of the diffracted wave vector $\vec{k}_{hk}$. Because the diameter of the Ewald sphere depends on the energy of the electrons, the behavior of LEED spots at different electron energies can be easily understood. If the diameter is smaller than the distance of two rods, only the reflection of electrons in opposing direction can be detected, which is called zero-order spot ($\vec{k}_{00}$). By increasing the energy the Ewald sphere will cross the first rods, leading to first-order spots ($\vec{k}_{10}$ and $\vec{k}_{\bar{1}0}$). Further increasing the energy will bring the first-order spots closer to the center and by crossing the next rods, higher-order spots will appear ($\vec{k}_{20}$, $\vec{k}_{30}$ and so on).

Alternatively, the spots at which interference occurs can be described by Braggs's law (cf. Figure 3.8a):

$$n\lambda = a\sin(\varphi) \tag{3.14}$$

Here, n represents the order, λ the wavelength of the electrons, a the spacing of the lattice and φ the angle of the scattered wave with respect to the surface normal, where $a\sin(\varphi)$ is equal to the path difference of two neighboring waves. Considering the de Broglie wavelength of an electron, the wavelength is given by:

$$\lambda = \frac{h}{p} = \frac{h}{\sqrt{2m_e E_{kin}}} \tag{3.15}$$

with Planck's contant h, the momentum p, the mass m_e and the kinetic energy E_{kin} of the electron. Now, equation (3.14) can be rewritten:

$$\sin(\varphi) = \frac{h}{\sqrt{2m_e}} \frac{n}{a\sqrt{E_{kin}}} \approx 1.226 \frac{n}{a[nm]\sqrt{E_{kin}[eV]}} \tag{3.16}$$

which gives a direct relation between the adjustable electron energy, the measured angle of the diffracted electron and the unknown lattice parameter.

The penetration depth of electrons is in the range of just a few Ångströms at typical energies of 10-200 eV. Therefore, LEED is very surface sensitive. Due to the diameter of the electron beam of about 1 mm, LEED provides averaged information of a relatively large area compared to the very local character of STM or AFM. Of course, only periodic structures contribute to the LEED pattern. Amorphous structures and a high density of surface defects will just increase the overall underground. Complex structures with reconstructions or different domains may lead to also very complex LEED patterns, which are often only explainable by comparison with simulated patterns. In combination with information derived by direct STM observations the structure of surfaces can be nicely characterized.

3.4 Electron spectroscopy

Already in 1839 a new phenomenon, which today is called photoelectric effect, was observed by Becquerel. Further systematic investigations were done in 1886 by Hertz and his assistant Hallwachs [43]. They were able to show that metal surfaces can be stimulated to emit electrons by irradiation with light. Not understood at this time was the dependence of the electrons' kinetic energy on the color, and therefore energy of the light, rather than its intensity as predicted by Maxwell's wave theory of light. This seemingly paradox phenomenon was solved 1905 by Einstein, who proposed that light has to be considered as a particle in this particular case [44]. He called these particles photons and claimed the energy E_ν would be proportional to its frequency ν:

$$E_\nu = h\nu \tag{3.17}$$

with a proportionality constant h which was later called Planck's constant. An electron is ejected from the metal only if its frequency is sufficient to

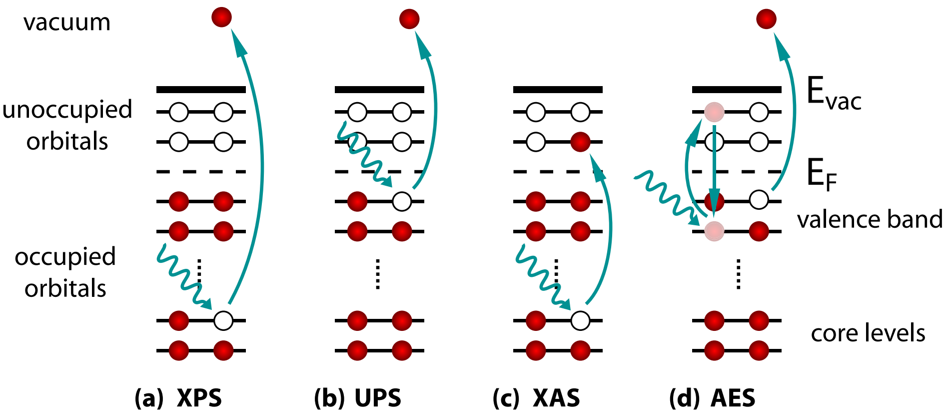

Figure 3.9: Schematic drawing of different effects in electron spectroscopy.

overcome a certain energy threshold. This brave hypothesis later lead to the revolution of quantum theory and Einstein was awarded with the Nobel Prize in 1921. Today, several experimental techniques have been established, which are all based on the same principle. In all cases the sample is irradiated with light of a certain energy. The most relevant processes which may take place are sketched in Figure 3.9. If the energy of the photon is sufficient to ionize the molecule, a free electron will be created (Figure 3.9a and b). This process is called photoelectric effect and consequently the free electrons are called photo-electrons. The according techniques are summarized as photoelectron spectroscopy (PES) and will be discussed in detail in the next section. If the energy is not sufficient to eject electrons, but to excite one electron from an occupied state to an unoccupied orbital, the photon may be absorbed as well (Figure 3.9c). This process is used in X-ray absorption spectroscopy (XAS) and one such technique will be discussed in section 3.4.2. Usually, an electron stays in an excited state just for a very short time. In most cases it will fall back in its original state, giving its excitation energy away. This transition is accompanied either by emitting a photon of the original energy (which may then subsequently interact with other molecules) or free of radiation. One process of radiation free transitions is the Auger effect (Figure 3.9d). There the relaxing electron passes its energy directly onto another electron for which the energy is sufficient to be ejected from the molecule. This effect is used in Auger electron spectroscopy (AES) which provides useful information about the sample, but won't be discussed in detail here.

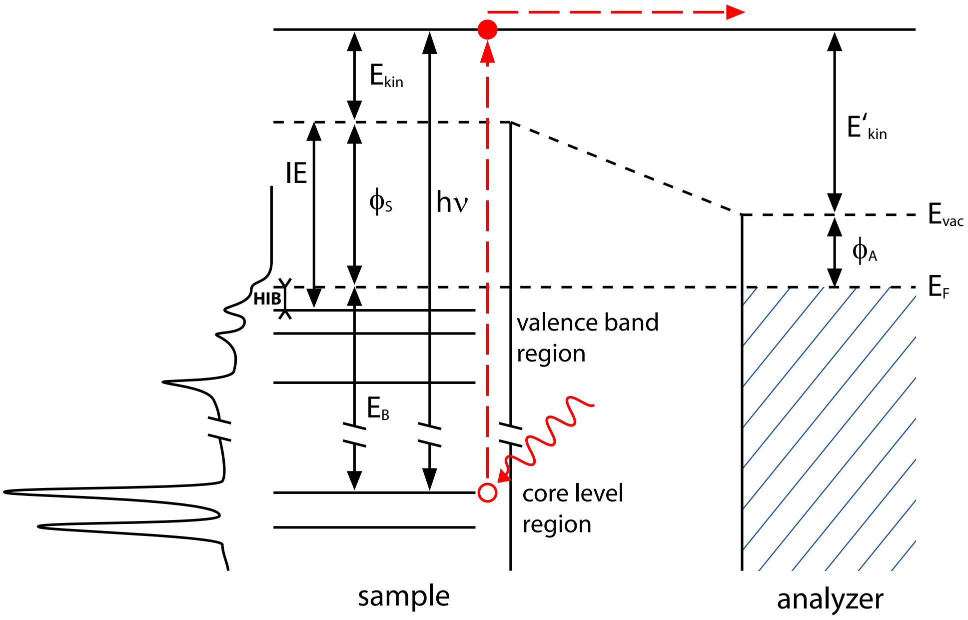

Figure 3.10: Sketch of the energy levels typically found in the experimental setup for photoelectron spectroscopy. The red line shows a photoelectron which is excited in the organic material and then travels to the analyzer.

3.4.1 Photoelectron spectroscopy (XPS, UPS)

As already mentioned before, in photoelectron spectroscopy an electron is ejected from the molecular layer by the absorption of an incoming photon. For this process the photon needs sufficient energy E_ν to remove the electron from its molecular state. A principal sketch of energy levels of the situation typically found in organic materials is shown in Figure 3.10. First of all, depending on the molecular orbital in which the electron is bound, it has a certain binding energy E_B, which is the difference of the considered energy level and the Fermi level E_F. The Fermi level simply separates occupied from unoccupied orbitals (cf. Figure 3.9). In case of a metal, electrons are filling a continuum of states up to the Fermi level, like shown for the analyzer on the right side in Figure 3.10. Since an organic molecular layer behaves like a semiconductor, usually the highest occupied molecular orbital (HOMO) is still well below the Fermi level, thus having a certain amount of binding energy. This is comparable to the ionization energy of a single molecule. When talking about a solid state, additionally, the electron has to overcome the work function of the material ϕ_S. The work function is defined as the minimum energy which is needed to eject an electron from a metal, i.e.

the difference in energy between the Fermi level E_F and the vacuum level E_{vac}. Although, in an organic solid the Fermi level is in general not equal to the energy of the highest occupied level, an analogous definition is applied. All energy in excess of these both compounds in difference with the initial photon energy E_ν converts into kinetic energy of the electron E_{kin} (left side of Figure 3.10). Hence, the energy balance for the ejection of an electron from the organic material can be written as:

$$E_{kin} = h\nu - E_B - \phi_S \tag{3.18}$$

This energy cannot be measured directly as the situation in a real experiment is more complicated. At this point the analyzer for determining the kinetic energy can be treated like a black box which behaves like a metal solid with a usually unknown work function ϕ_A. Of course, in general the work functions of the sample ϕ_S and the analyzer ϕ_A are not equal. This changes the situation for electrons which travel into the analyzer. In order to have defined conditions, sample and analyzer are held at the same potential. This leads to an alignment of the Fermi levels in thermodynamic equilibrium. Still, the vacuum level will change from sample to analyzer, implicating a change of the kinetic energy of the electrons, too. However, for a given experimental setup ϕ_A remains constant and therefore the measured kinetic energy of the electron E'_{kin} is only dependent on the constant potential difference between sample surface and analyzer:

$$E'_{kin} = h\nu - E_B - \phi_A = E_{kin} - (\phi_A - \phi_S) \tag{3.19}$$

By keeping the photon energy $h\nu$ fixed, the energy distribution of the sample can be measured by simply sweeping the measured kinetic energy E'_{kin} while counting the number of electrons for a defined time interval at each energy. This way a full range spectrum containing the electron energy distribution as shown exemplary in Figure 3.11 can be obtained. The scale can be easily converted into binding energy by referring to the measured kinetic energy of the Fermi edge $E_B = E_F^k - E'_{kin}$. No electrons are counted for kinetic energies either above the kinetic energy of the Fermi edge E_F^k, because no more occupied states are found there, as well as below the so called secondary electron cut-off (SECO), marked by the onset E_{CO}^k. This lowest kinetic energy is generated by secondary electrons originating mainly from photoelectrons which were inelastically scattered within the sample. Of course, also electrons from states which barely exceed the vacuum level after photon absorption, will contribute to the SECO. In fact, in a real experiment the different work functions of sample and analyzer are important again. If the work function of the analyzer is higher than that of the sample, the initial kinetic energy E_{kin}

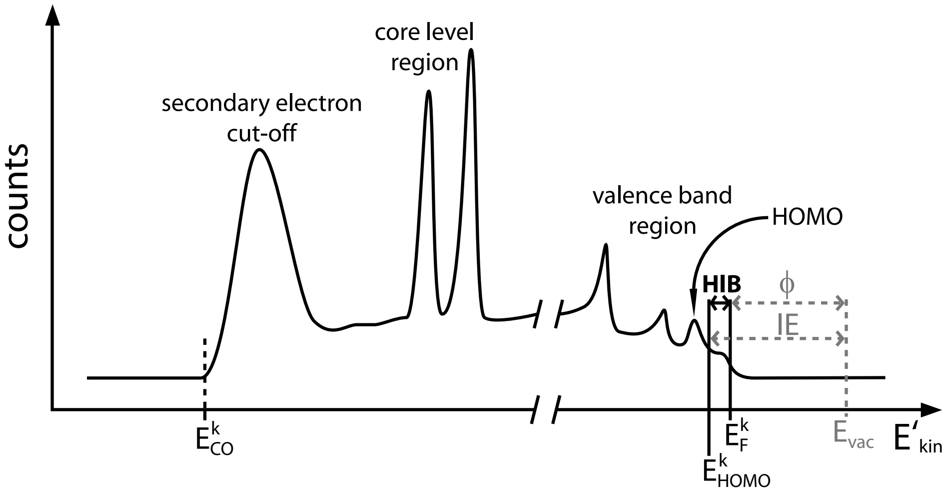

Figure 3.11: Typical full range spectrum derived by photolectron spectroscopy.

of electrons with kinetic energies close to the SECO is not sufficient to enter the analyzer ($E_{kin} < \phi_A - \phi_S$). Therefore, in order to ensure the real SECO can be detected, a negative potential U_{off} is applied to the sample resulting in a rigid upward shift of sample states with respect to the analyzer. Then the real SECO E^k_{CO} is calculated from the shifted one E^{off}_{CO} by:

$$E^k_{CO} = E^{off}_{CO} - U_{off} \tag{3.20}$$

Now the work function of the sample can be determined (cf. Figure 3.11):

$$\phi_S = h\nu - (E^k_F - E^k_{CO}) \tag{3.21}$$

In principle, the minimum kinetic energy of an electron ejected from the sample and therefore the SECO are expected to be zero. Due to the potential difference between sample and analyzer, this is not the case. Hence, in order to determine the sample work function the SECO has always to be measured, too. Other parameters of interest derived from photoemission spectra are the ionization energy (IE) and the hole injection barrier (HIB). Both are referring to the onset of the HOMO E^k_{HOMO} and are calculated as follows:

$$IE = h\nu - (E^k_{HOMO} - E^k_{CO}) \tag{3.22}$$

$$HIB = E^k_F - E^k_{HOMO} \tag{3.23}$$

Depending on the photon energy used for photoelectron spectroscopy, different energetic levels can be measured. To derive information about core levels of a sample, X-rays are needed. This is done in X-ray photoelectron spectroscopy (XPS). Core electrons are tightly bond to the nucleus and therefore not directly involved in the bonding to other atoms. Orbitals of core levels have nearly atomic character due to their high binding energy and exhibit defined energies depending on the chemical compound. Nevertheless, the detailed position of core levels depends also on the chemical environment, leading to so called chemical shifts of core levels. Thus, XPS is often used to identify unknown species of a sample, determine relative quantities of a compound and gather information about its chemical environment. Of course, information about low binding energy levels of the valence band are already included in XPS spectra. However, for probing the valence band the use of photon energy in the same energetic region is recommended due to the gain of much higher sensitivity. For this usually ultraviolet photoelectron spectroscopy (UPS) is used, which utilizes ultraviolet light. Since valence electrons are relatively weak bond, they are directly involved in the binding between neighboring atoms and the valence levels are strongly affected by chemical interactions. Especially the position of the HOMO is of great interest as it is crucial for the electronical properties of organic semiconductors in devices.

PES is one of the most widely used techniques to investigate the chemical structure of samples and gain information about fundamental electronic properties of materials and their combinations. For detailed interpretation of the spectra often quantum chemical calculations are needed.

3.4.2 Near edge X-ray absorption fine structure spectroscopy

Another important spectroscopic technique is near edge X-ray absorption fine structure spectroscopy (NEXAFS). In NEXAFS the irradiated material is not ionized directly by the incoming photon beam. Instead, the photon energy used in this technique is only sufficient to excite core level electrons (cf. Figure 3.9c). Therefore, X-rays are needed. Unlike the PES techniques, the photon energy in this case is not constant but sweeps over an interval around the binding energy of the appropriate investigated element. In organic molecules typically the carbon edge is probed. Sample spectra are shown in Figure 3.12. Since no electrons are ejected by the primary absorption process, also the detection has to be different from PES. One possibility is to measure the light absorption by detecting the intensity of the reflected or transmitted light and compare it to the initial intensity. Usually, it is easier to detect the products of secondary processes. Excited electrons will relax to its initial

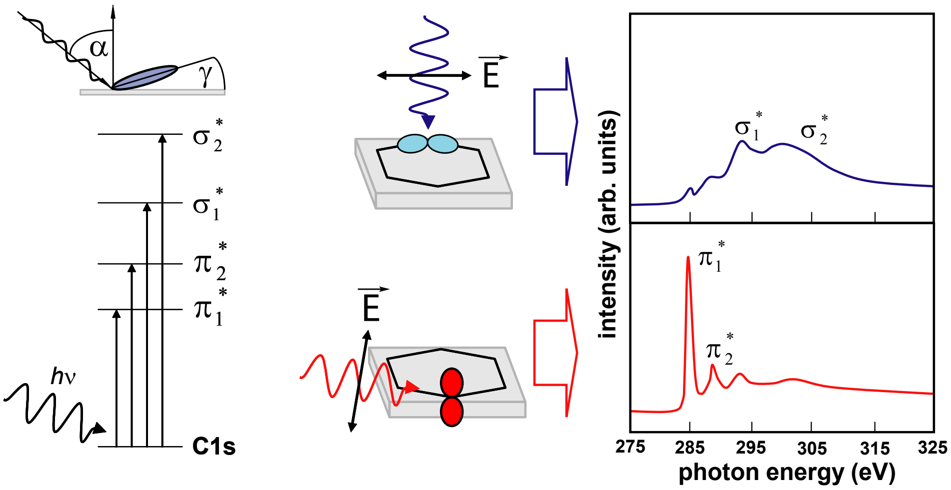

Figure 3.12: Angular dependence of NEXAFS spectra on the orientation of molecules. On the left schematic energy levels of the sample are presented. In the middle the coupling of the incoming photon to molecular orbitals is sketched for two different angles. Appropriate sample spectra for flat lying benzene on Ag(110) according to Stöhr [45] are shown on the right.

state after a short period of time by releasing its excitation energy again. This is done by emitting a photon or by an Auger process. Thus, also the fluorescence light and Auger electrons can be used for probing the absorption process. The typical penetration depth of the incoming light is up to 500 Å. This is much higher than the maximum escape depth of electrons, which is up to 50 Å depending on their energy. Therefore, many electrons will undergo further excitation or scattering processes. Also the reemitted photon may interact with the material again. Consequently, a broad spectrum of low energy secondary electrons are generated. Hence, detection of either the total electron yield or secondary electrons at specific kinetic energy is most effective. Now, starting with a photon energy below the lowest possible excitation, no signal can be detected (except the background). Once the photon energy reaches the energy difference of the first possible excitation (from a core level to π^*) the signal will show a sharp rise (cf. Figure 3.12), which is called the absorption edge. By further increasing the energy, the signal will decrease again until the next possible excitation is reached. This way all unoccupied states within the measured range are mapped. Since these states depend on their chemical environment, NEXAFS may be used to analyze the chemical bonding within the material.

More important for this work is another advantage of NEXAFS. If polarized light is used to irradiate the sample, a strong dependence of the measured signal on the angle of the incoming light is found for molecules with defined ordering of their orbital system. This is illustrated in Figure 3.12 for benzene on Ag(110). In this example the molecular ring lies flat on the surface. The σ-orbitals lie in-plane while the π-orbitals stick out-of-plane. Linear polarized light has an electric field vector which is perpendicular to the incoming beam direction. Irradiating the sample from the side leads to most efficient coupling between the beam and the π-orbitals (bottom in Figure 3.12), while perpendicular incidence will generate efficient coupling between beam and the σ-orbitals (top in Figure 3.12). Since the energetic levels of the excited states π^* and σ^* have distinct different heights, the different states can be distinguished in the spectra. By taking a series of incidence angles, a series of peak intensities I will be generated. For example the π^*-state will show following dependence [46, 47]:

$$I_{\pi^*} \propto P\left[\sin^2\gamma\sin^2(90^\circ-\alpha)+2\cos^2\gamma\cos^2(90^\circ-\alpha)\right]+(1-P)\sin^2\gamma \quad (3.24)$$

Here, P represents the degree of photon beam polarization which is characteristic for the beam source, α is the angle of the incident photon beam with respect to the surface normal and γ is the angle of the molecular plane with respect to the surface plane (cf. Figure 3.12). Once the orientation of orbitals within the investigated molecule is known, NEXAFS may be used to determine the molecular orientation with respect to the surface. One prerequisite is that the molecules have a regular orientation on the surface. In case of amorphous growth NEXAFS will just provide information about the averaged angle of all orientations found within the irradiated area.

For further details about NEXAFS spectroscopy please refer to the comprehensive book of Joachim Stöhr [45].

4 Experimental Details

In this chapter details about the experimental setups used within this work will be presented (section 4.1). Additionally, the preparation of samples is described (section 4.2), some details about the processing of the appropriate data (section 4.3) and in the end brief remarks about the theoretical calculation are given.

4.1 Experimental setup

To study the effects at the molecule-substrate interfaces and fundamental properties, special care has to be given to the environment of the experiment. Consequently, the use of ultra high vacuum is often necessary and was used for all experiments in this work. A general introduction is given in the following section. Then details of appropriate setups used for the different experimental techniques will follow.

4.1.1 Ultra high vacuum

In general, there are two reasons for using ultra high vacuum (UHV). First, samples have to be absolutely free of contaminants. This is the only way to ensure that properties and effects measured in an experiment have their origin just only in the materials which were originally intended to be used. One possibility to achieve this is to handle samples under controlled atmosphere of an inert gas (typically argon). There the usual atmosphere is nearly completely replaced by the gas. But an even better approach is to remove the atmosphere completely, thus generating vacuum. Complete removal of all particles in a volume to achieve perfect vacuum is technically not possible (even outer space still contains many particles). Therefore, the quality of vacuum is expressed by its pressure above zero, where 1013 mbar[1] refers to

---

[1] In vacuum science pressures are commonly expressed in mbar, which is accepted for the use with the SI and 1mbar = 1hPa.

atmospheric pressure. The development of vacuum-pumps took a long time. Hence, UHV is defined historically to be the pressure range which lies below 10^{-7} mbar. In fact, today UHV systems typically work in the range of $10^{-9} \ldots 10^{-11}$ mbar. This refers to a density of particles which is $10^{8} \ldots 10^{5}$ molecules per cm^{3}. To get a better impression of the 'emptiness' one can imagine the mean free path of a particle, which is the distance a particle will travel before interacting with another particle. At todays typical UHV pressure the mean free path is about $10^{1} \ldots 10^{4}$ km. Therefore, the probability for particles to interact with each other within the volume of a usual vacuum chamber is almost zero. Still, the probability for one particle to hit the sample in the chamber is much higher. As a result also at pressure of 10^{-11} mbar the sample will be contaminated by a monolayer of carbon within days.

A second benefit of using UHV is the accessibility of a number of techniques, which need vacuum to be conducted or are much more complicated under ambient conditions. For example, all techniques which involve irradiation with or detection of electrons are possible in ambient condition only with great difficulties and limitations. Again, in this case the mean free path plays an important role. Typically, electrons have to travel distances in the order of centimeters before they reach the sample or detector. Using UHV ensures they will not interact with residual gas molecules on this way. In fact, from this point of view STM and AFM measurements would have been possible also in ambient conditions, which is not the case for LEED and electron spectroscopy measurements.

Typical UHV pumping systems today, such as the systems used within this work, consist of at least 3 stages. The first stage is a pump for rough vacuum down to 10^{-3} mbar. For this, usually a rotary vane pump or scroll pump (for oil free applications) is used. These pumps remove the major part of gas from the chamber by simply forcing the volume to move in a defined direction. In the second stage already UHV is reached by using a turbomolecular pump, which ranges down to typically 10^{-9} mbar. Because in this operation range the gas has no real volume anymore but consists more of non-interacting molecules, the working principle is different. That kind of pump is build like a turbine with a series of rotors which rotate at high speed. Once a molecule is hit by a rotor, it will be given a momentum in direction out of the chamber. This leads to very efficient extraction of all molecules that reach the pump. The last pumping stage is no more mechanical. It consists of an ion getter pump which can reach pressures of 10^{-11} mbar. Molecules passing the pump will be ionized by a high electrical field and accelerated onto an electrode which is coated with a reactive material in the same field. Usually, titanium is used for this purpose, which then binds the

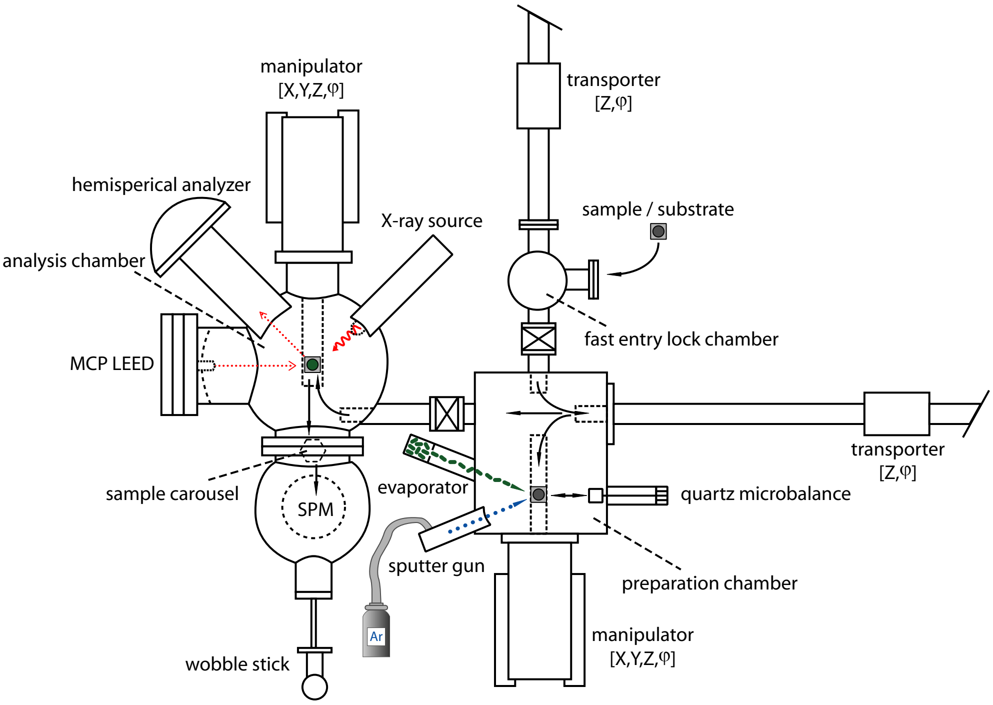

Figure 4.1: Schematic drawing of the UHV system used at Humdoldt University Berlin.

molecule. One advantage of this technique is the vibration free operation. Consequently, this is the only pump which can still run while doing scanning probe microscopy. To decrease the pressure furthermore or shorten the time until reasonable pressure is reached, in all systems used within this work a titanium sublimation pump was available. This pump simply evaporates titanium from a heated titanium filament onto the chamber walls. Again, molecules which hit the titanium coating will be bound, leading to a decrease in pressure.

4.1.2 Multiprobe chamber at the HU-Berlin

For most experiments a commercial UHV multiprobe chamber at our home institute at the Humboldt University in Berlin was used. A schematic drawing of this chamber is shown in Figure 4.1. It consisted of two main parts, where one was a preparation chamber (base pressure 10^{-9} mbar) and the other an interconnected analysis chamber (base pressure 10^{-11} mbar). For easy exchange of samples and SPM-tips, a small fast entry was attached to the preparation chamber, which could be pumped independently. Besides the deposition of molecules, the samples could be cleaned, heated and sputtered in the preparation chamber (cf. section 4.2). Samples were then transferred to the analysis chamber without breaking UHV conditions. The equipment of the analysis chamber allowed for carrying out several complementary techniques.

The core piece of the system was the commercial *VT UHV SPM* from Omicron. In this instrument not only STM measurements could be done, but also beam deflection AFM using an infrared laser. The abbreviation VT stands for variable temperature. According to the instrument specification, the working range stretches from 25 K, using liquid helium, up to 1500 K by heating the sample by a current flowing directly through the sample. Although, some cooling experiments at the lower edge of this temperature range were carried out, none of them is presented in this work because they did not provide additional information about the presented material systems. Vibrational damping was achieved using an internal spring suspension system with eddy current damping. No additional external vibration isolation was needed. Switching between STM and AFM was easily achieved by simply changing the probing tip and choosing appropriate settings in the scanning software. By using different cantilevers it was possible to do contact as well as non-contact mode AFM. The combination of STM and AFM allowed for observations of single molecules within sub-monolayer deposition up to huge islands of multilayers. For data acquisition the Omicron Scala 5 software was used.

While SPM always reveals only very local ordering of the substrate surface, the averaged periodicity of larger areas of the sample can be studied by LEED. For this purpose a commercial *Omicron MCP LEED* was attached. Unlike conventional LEED systems diffracted electrons are not directly visualized on a phosphor screen. Instead, they have to pass a multi channel plate (MCP) in front of the screen. The advantage of this modification is found in the ability to visualize also electron beams with very low current. Organic materials are often very sensitive and may easily be destroyed by electron beams of high intensity. Therefore, low current of the initial electron beam is preferred. Consequently, diffracted electrons exhibit even lower beam currents, leading to weak illumination of the phosphor screen, which makes it hard to observe diffraction spots. By using a MCP the electron current is amplified and leads to detectable illumination of the screen. In this particular case the LEED system was equipped with a single MCP. Spots on the screen were recorded as a photograph by digitizing the image with a CCD-camera via the Omicron SpectaView software.

To analyze the chemical composition and chemical reactions of the organic-substrate interface a commercial XPS system from SPECS was used. One part of it was the X-ray source *XR 50* in combination with the power unit *XRC 1000*. The source included a twin anode comprising two different anode materials (Al and Mg). It was operated at a fixed voltage of 12 kV, while the emission current was varied typically between 2 mA and 15 mA. Additionally, the source was movable towards the sample by a z-drive. Hereby, the electron yield could be increased. Photoelectrons were detected by a *PHOIBOS 100* using the *HSA 3500* power supply. This is a 180° hemispherical analyzer with 100 mm radius. The resolution in XPS mode is about 1 eV and electrons were counted by five simultaneously working single channel electron multipliers. Spectra were recorded using the SPECS SpecsLab 2 software which already preprocessed the signal of the five channeltrons to generate one signal.

4.1.3 UPS at HASYLAB Hamburg

Some of the UPS measurements were done at the FLIPPER II endstation at the synchrotron light source HASYLAB in Hamburg. Similar as before the UHV chamber consisted of an analysis chamber (base pressure 10^{-10} mbar) connected to a preparation chamber (base pressure 10^{-9} mbar). Light from the synchrotron source was monochromatized by a combination of mirrors and a grating which lead to efficient depressing of higher order contributions in the monochromated beam. The energy could be adjusted in the range between 10 eV and 300 eV. Typically an excitation energy of 22 eV was used. Electrons were detected by a double-pass cylindrical mirror analyzer with resolution of about 200 meV. Data acquisition was carried out using a PDP-11 terminal.

4.1.4 NEXAFS/PES at BESSY Berlin

Additional UPS and XPS measurements were carried out at endstation SurICat (beamline PM4) at the synchrotron light source BESSY in Berlin. There spectra were collected with a hemispherical electron energy analyzer *Scienta SES 100* with an energy resolution of 120 meV. The typical excitation energy used at this endstation was 41 eV. NEXAFS measurement have also been done at BESSY using the equipment of another endstation at the Russian-German beamline. The excitation energy was varied by sweeping the monochromator simultaneously to the measurement. Spectra were detected at a selected kinetic energy of 6 eV using a *PHOIBOS 150* from SPECS including 25 channeltrons. Again, both systems were build of a separated analysis (base pressure 10^{-10} mbar) and preparation chamber (base pressure 10^{-8} mbar).

4.2 Sample preparation

For studies presented in this work the cleanliness of samples was of particular importance. All presented results were obtained at the interface of an organic molecule and a metal single crystal as the substrate. In particular, only single crystals of (111) orientation were used. Irrespective of their surface-reactivity and how long they have been under low pressure since they were placed into the vacuum system, all crystals are originally covered by at least one or more monolayers of carbon. This defines the requirement of a cleaning process to get rid of all contaminations at the surface. An easy way to achieve this goal is to sputter the surface. Sputtering is a process which removes atoms from a surface by the bombardment of high energetic ions. When an ion with a defined momentum impacts a surface atom, it will transfer its momentum leading to ejection of the targeted atom. For this process a high atomic mass of the ion is of advantage. Because the bombarding ion should not replace the surface atom but also leave the surface, the use of an noble gas is mandatory. Usually, argon is used for this purpose. To avoid further contamination, highly purified gases are needed, which are commercially available. The gas flow into the system is controlled by a leak valve. In the sputter gun Ar is first ionized and then accelerated in an electric field. By tuning the acceleration voltage the deposited energy can be easily controlled. All crystals in this work were sputtered at an energy of 600 eV for 40 min in one cycle. Even though, at this energy the sputtering is rather gently, the surface will be roughened by this process. For experiments shown here atomically flat surfaces are advantageous. In principle, the smoothing will take place itself by diffusion of surface atoms and resulting redistribution in rather large terraces which are energetically preferred. This process is also called healing of the surface. To increase the diffusion rate and consequently shorten the healing time, the surface atoms can be given energy by simply heating the sample, which is called annealing. The annealing time and maximum temperature depends on the material and was in the range of 350 °C to 550 °C for about 0.5 h up to 1.5 h. Best results were achieved when the cycle of sputtering and annealing was repeated at least two or three times, depending on the degree of contamination. The cleanliness of the crystal was then verified by photoemission experiments, LEED and STM, if available at the appropriate experimental setup. For example a clean gold-crystal shows only contributions of the Au-core levels in XPS, while the C1s state has vanished.

After making sure the substrate is clean, the molecules were applied to the surface. In this work all molecules were sublimated from pinhole sources.

Pinhole sources are small letter shaped cases made of tantalum foil with tantalum legs at each side and a small hole at the top. The source is filled with the required molecules as powder. Heating of the source is established by applying a voltage between both legs, resulting in a current flowing trough the source. Because of the non-zero resistance the source will then heat up. By varying the heating current the sublimation point of the molecule can be reached and an evaporation rate adjusted. Due to the orientation of the hole, molecules have a momentum in direction towards the sample and will deposit onto the sample surface. Of course in this simple technique the deposition rate can not be predicted from the heating power. To control the amount of deposition, a quartz crystal microbalance (QCM) is moved into the intended position of the sample prior to the actual deposition. If properly adjusted the QCM records the amount of molecules per time interval. However, QCM and sample will always have slightly different properties like the sticking coefficient, which are not always completely determined. Hence, the reading of the QCM gives always the nominal amount of molecules. Once the molecular flux is adjusted with the QCM and remains stable, the sample is placed at the same position. In case of thick films, which involves higher deposition times, it turned out to be more accurate to place the QCM next to the sample while deposition runs. Then possible fluctuations of the molecular beam during longer periods can also be taken into account.

Using the preparation procedure described before, samples of high purity were produced with molecular depositions tuned in the range of submonolayer up to multilayer. Once a sample was prepared it was usually measured immediately. Sometimes further treatment of samples like annealing the molecules was needed. Although, samples will be slowly covered by carbon from inside the UHV system, it turned out that SPM measurements on molecular films could be reproduced over the period of days.

4.3 Data processing

In this section an overview about the treatment of the appropriate data after acquisition should be given. This includes all general steps applied to the data. If special further processing was applied it will be mentioned at the point of presentation of the according data.

4.3.1 Processing of SPM/LEED-images

For processing SPM-images mainly the commercial software SPIP (Image Metrology) was used. In some cases additional analysis was done using

WSxM (Nanotec Electronica S.L.) [48]. Presented images are raw data except for some standard corrections. First, a plane was subtracted from all images to correct the tilting of the sample plane with respect to the scanning plane. To improve this process sometimes line-wise correction was also applied, depending on the success of this correction estimated from the resulting image. Second, the distortion of the image due to thermal drift of the piezoelectric scanner had to be corrected in most images. The difficulty is to find the right correction parameters. Depending on the available information parameters were determined by comparing the structure to simultaneously achieved known structures, such as the atomic lattice of the substrate or known reconstructions. If appropriate data was available the molecular lattice was extracted from LEED measurements. For the case where information about the undistorted lattice were available, the distorted lattice was corrected by applying the correction to the two-dimensional Fourier-transformation and then calculate the inverse transformation into real space. LEED images themselves were also loaded into SPIP to determine the distance between spots, from which then real space values were calculated. If not stated otherwise STM pictures presented in this work are height images and AFM was conducted in non-contact mode.

4.3.2 Fitting of XPS-spectra

After exporting XPS-spectra to ASCII-format, they were loaded into WinSpec 2 (University of Namur, Belgium). There the peaks could be fitted as a convolution of Lorentzian and Gaussian functions. Known dependencies between peaks, for example fixed peak splittings or intensity ratios, could be set as prerequisite in the software, which greatly improves the fitting quality. To address the underground of the spectra a Shirley background was added. Peak positions were then derived from the positions of the maxima in the appropriate fittings, while the area under the peaks was used to compare relative peak intensities (Figure 4.2a). Measured kinetic energy was converted to binding energy using the excitation energy and given analyzer work function in case of the SPECS system. For measurements at the synchrotron the work function was not given. However, binding energy could be calculated using a substrate peak with known binding energy as reference.

4.3.3 Analysis of UPS-spectra

Spectra were first converted to ASCII-format and then imported into Origin 8 (OriginLab) for further processing. The Fermi energy was determined as middle point between the intersection points of a straight line fitted into

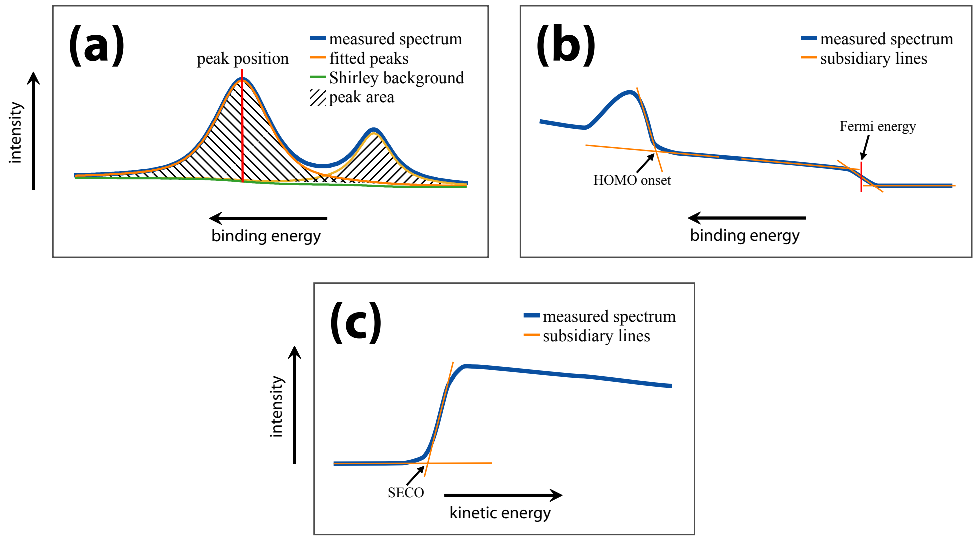

Figure 4.2: Schematic drawing of the construction procedure to derive the different parameters from the spectra for (a) core levels (b) valence band regions and (c) secondary electron cut-offs.

the Fermi-edge and the two extended lines of the ground signal and the signal below the Fermi-edge respectively (Figure 4.2b). For declaration of the HOMO position the onset of the HOMO-peak was used, meaning the intersection point of a straight line fitted into the slope of the HOMO-peak and a line fitted into the signal at lower binding energy (Figure 4.2b). In the same way the secondary electron cut-off was determined (Figure 4.2c). Kinetic energy was converted into binding energy by simply using the determined Fermi-energy as reference point.

4.3.4 Processing of NEXAFS-spectra

NEXAFS spectra have to be very carefully evaluated. In order to gain reliable results all spectra have to be calibrated in energy and normalized in intensity following the usual procedure described by Schöll *et al.* [49]. The measurement of a single spectrum took about half an hour. Because the intensity of synchrotron radiation decreases significantly on this time scale, monitoring the beam current while the measurement is running is mandatory. This change can then be eliminated by normalizing the spectra to the beam current. Another problem is found in residual carbon contamination within the chamber. In general, carbon is covering everything inside the chamber with at least one monolayer. This also includes windows and gratings which the beam has to pass. Because in the work with organic molecules the resonances at the C1s edge are of interest, spectral features caused by residual carbon contaminations have to be eliminated. To achieve this, spectra were simply normalized to the step edge spectrum of the cleaned substrate, which should not contain any carbon at all. Carbon features found in these spectra apparently originate from residual carbon contamination in the chamber. Additionally, typical features found in the background could be used for the energy calibration. In fact the photon beam energy may vary slightly between two subsequent injections. Since system specific contributions to the carbon signal are independent of the sample preparation, all spectra could be calibrated to identical energy scale by superimposing these features. As last step the spectra were additionally normalized to the intensity at 320 eV, at which they are expected to be independent from angular variations.

4.4 Theoretical calculations

In extension of the experimental work, theoretical calculations have been done for some of the systems. These were carried out by Norbert Koch (calculations of molecular orbitals) and Oliver T. Hofmann (simulation of STM and DOS calculations). Only a brief description of the appropriate methods will be given here. For further, more detailed information please refer to the according references.

Molecular orbitals to determine HOMO and LUMO in section 5.1 and section 5.3, as well as to retrieve the energy consumption of different molecular conformations in section 5.1 were calculated within the framework of density functional theory (DFT). This was done for the relaxed geometry restricted in symmetry for certain conformations. The B3LYP functional [50] in conjunction with a 6-311G** basis set was used. Calculations were performed with GAUSSIAN 03 [51].

Theoretical calculations in section 5.4 were done with the VASP (Vienna Ab-initio Simulation Package) code, using the PW91 exchange-correlation functional [52–55]. A plane-wave basis set with a cutoff energy of 20 Ryd was used. For the valence-core electron interaction the projector augmented-wave method (PAW) [56, 57] was applied, which allowed for the low kinetic energy cutoff for the plane-wave basis set. The unit cell was sampled by a Monkhorst-Pack grid of $2 \times 2 \times 1$ k-points [58] for the self-consistent field calculations together with a Methfessel-Paxton occupation scheme [59] (broadening of 0.2 eV). All calculations were done in a non spin-polarized manner. The geometry of the individual molecules was obtained by a geometry optimization of a single molecule in a $7 \times 4\sqrt{3}$ unit cell. Relaxation was performed on a three layer metal slab, where all atoms of the molecule as well as of the uppermost metal layer were fully relaxed using a damped molecular dynamics scheme until the remaining forces were smaller than $0.02\,\mathrm{eV/Å}$. The relaxed geometry was then extended to a five layer metal slab in order to obtain a more reliable description of the electronic structure.

Furthermore, from STM experiments in section 5.4, a packing density of ca. $0.44\,\mathrm{molecules\,/\,nm^2}$ was inferred. For the calculation of the density of states and the simulation of STM pictures, a hexagonal $4\sqrt{3}\times 4\sqrt{3}R30°$ unit cell was employed, containing 2 molecules forming a honeycomb pattern. The molecule was rotated by 10° counterclockwise with respect to perfect alignment of the C_2-axis to correctly account for the experimental structure.

The atomic orbital-projected density of states (PDOS) in VASP was determined by projection of each Kohn-Sham orbital onto spherical harmonics inside spheres around each atom and weighing the contribution of that atomic orbital to the DOS accordingly. To obtain the DOS projected onto the molecule (molecular DOS, MDOS), all non-metallic contributions were summed up.

To obtain simulated STM pictures, the Tersoff-Hamman [30, 31, 60] approach was employed. Within this method, constant current images are given by integration of the local density of states between the tip bias and the Fermi energy. In order to maintain a realistic situation, the STM-tip was modeled as a finite size, spherical object with ca. 2 Å diameter. Within this region, 69 points were sampled and then averaged. More details to this method are given elsewhere [61].

5 Results & Discussion

In this chapter all results accompanied with appropriate discussions are presented. A brief introduction of the substrate used for the experiments is given at the beginning of the respective sections. Then the actual experiments will follow. The first molecular system will deal with the influence of alkylation on the ordering behavior of sexithiophene on Au(111), presented in section 5.1. Secondly, the structural and electronic changes in dependence of the molecular film thickness will be discussed at the exemplary sample system of hexa-*peri*-hexabenzocoronene on Ag(111) in section 5.2. Then it will be shown in section 5.3 that fluorination of pentacene leads to strong chemical reactivity of the molecule on Cu(111). Finally, a completely new approach of reducing the interaction of C_{60} with the metal substrate Ag(111) by introducing a template layer will be presented in section 5.4. Conclusions derived from the investigations of the different molecular systems are included in the appropriate sections.

5.1 Alkylation effects on self-assembly

At first, the influence of the substrate on self-assembly of molecules should be investigated. For this purpose Au(111) was chosen as substrate material, because it has some advantageous properties. On the one hand gold exhibits only low reactivity, while on the other hand providing an interesting structural template due to its surface reconstruction. In this reconstruction two different length scales occur, which may be exploited for directed self-assembled growth (details will be discussed in the next subsection). Consequently, for these experiments two different molecules were chosen which fit into the two reconstruction patterns. The first one is α-sexithiophene (6T). The chemical structure of this molecule is presented in Figure 5.1a. It simply consists of six thiophene subunits which are connected by single bonds. The length of this molecule almost matches the short distance reconstruction pattern of Au(111) (see Figure 5.2d). By addition of alkyl chains at the very

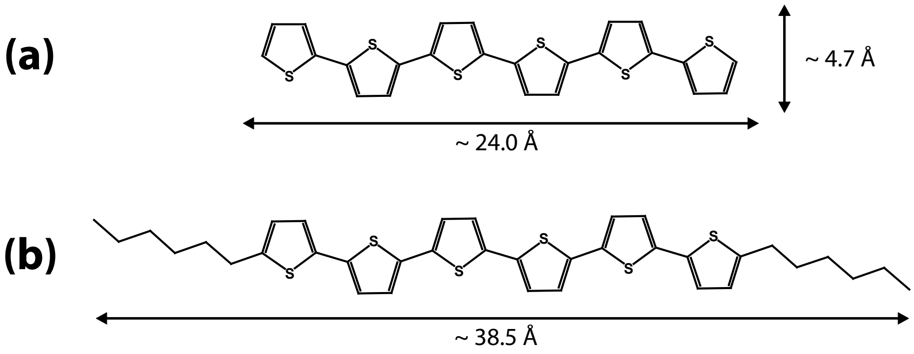

Figure 5.1: Chemical structure of (a) α-sexithiophene (6T, $C_{24}H_{14}S_6$) and (b) α,ω-dihexyl-sexithiophene (DH6T, $C_{36}H_{38}S_6$). Numbers of the molecular size include the hydrogens, which are not painted.

end of 6T the length can be adjusted to fit the second reconstruction pattern. The resulting molecule is α,ω-dihexyl-sexithiophene (DH6T) and its chemical structure is shown in Figure 5.1b. Still, the conjugated core of the molecule remains the same, while the alkyl chains act as spacers. Studying the adsorption behavior of both molecules in comparison will provide information about the influence of alkylation, which should be helpful for future molecular design of directed self-organization schemes.

Moreover, the class of oligothiophenes is of interest in terms of organic and molecular electronics since it has been shown that materials thereof possess interesting electronic and optical properties. In particular, using 6T molecules in organic electronics demonstrated their rather high charge carrier mobility of about $0.02\,\mathrm{cm^2V^{-1}s^{-1}}$ [62] and absorption and emission in the visible range for potential use in OLEDs [63]. Quite several investigations on thin films of 6T adsorbed on different substrates have already been published in recent years, e.g. on Ag(110) [64], Ag(111) [65], Cu(110) [66], Au(110) [67] and Au(111) [68, 69]. Many interesting structures and ordering behaviors of 6T were revealed. In contrast to previous studies, in this work a detailed analysis of the molecular growth starting from sub-monolayer coverage was conducted. In comparison with the growth of DH6T, new insight in the growth mechanism will be achieved. Although the chains of DH6T are rather short, they have substantial influence on the properties and ordering behavior of the molecule. Due to the lack of conjugation in alkyl chains they are not only acting as spacers, but have also isolating character. Consequently, their conductivity along the long molecular axes is rather poor. In direction of their short axis, which is usually the stacking axis, the conductivity is a factor of 120 higher, reaching a charge carrier mobility of $0.05\,\mathrm{cm^2V^{-1}s^{-1}}$

[70]. Although, these properties are quite promising, comparatively little is known about DH6T [70–74]. Therefore, investigations of DH6T are of special interest.

5.1.1 Au(111)

Because of its substantial importance for this study, at first the structural properties of the substrate material will be discussed. The gold crystal has a face-centered cubic (fcc) lattice as shown in Figure 5.2a with lattice constant of $a_{Au} = 4.07\,\text{Å}$. Cutting the crystal in (111)-direction leads to the plane indicated by the grey shaded triangle. The resulting surface lattice has hexagonal symmetry with lattice constant of $a_{Au}/\sqrt{2} = 2.88\,\text{Å}$. A high resolution image of the atomic lattice is shown in Figure 5.2b. In the inset the appropriate LEED image is displayed. Real crystal surfaces always possess a miscut, leading to the formation of step edges as shown in Figure 5.2c. The Au(111) crystal used in this work had a typical terrace width of up to 150 nm. The step height between two layers in (111)-direction of gold is $a_{Au}/\sqrt{3} = 2.35\,\text{Å}$. One special feature of Au(111) crystals is the appearance of a surface reconstruction. Due to the broken symmetry at surface the surface lattice relaxes to a structure which is different compared to the bulk in order to minimize its energy. In this case the surface is contracted in the $[1\bar{1}0]$ direction, leading to a $23 \times \sqrt{3}$ reconstruction [75, 76]. This reconstruction is clearly visible in Figure 5.2d. It is composed of two different alternating atom packings occurring at the surface. Two packing structures are separated by small corrugation lines respectively, visible as bright stripes in Figure 5.2d. These lines are already visible in Figure 5.2b appearing as intensity variations of the surface atoms. They are also included in Figure 5.2c, but are not visible in this presentation due to the already high contrast between the topmost and lowest terrace in this image. Two closer lines with a distance of ca. 2.5 nm comprise hcp packing, whereas in the wider-distance of ca. 3.8 nm fcc packed atoms are confined. These two patterns match with the length of the chosen molecules for these experiments, i.e. 6T and DH6T. Because of the typical occurrence of orientation changes by 120° about every $(15 - 20)$ nm this structure is commonly called ‘herringbone’ reconstruction. Apart from creating a pattern for directed self-assembly, the advantage of this reconstruction lies in the fact, that it is often still visible in STM even if no atomic resolution is achieved or a monolayer of molecules is adsorbed on top. Thus it provides the possibility to determine the crystal orientation and was also used to calibrate the length scales in STM images.

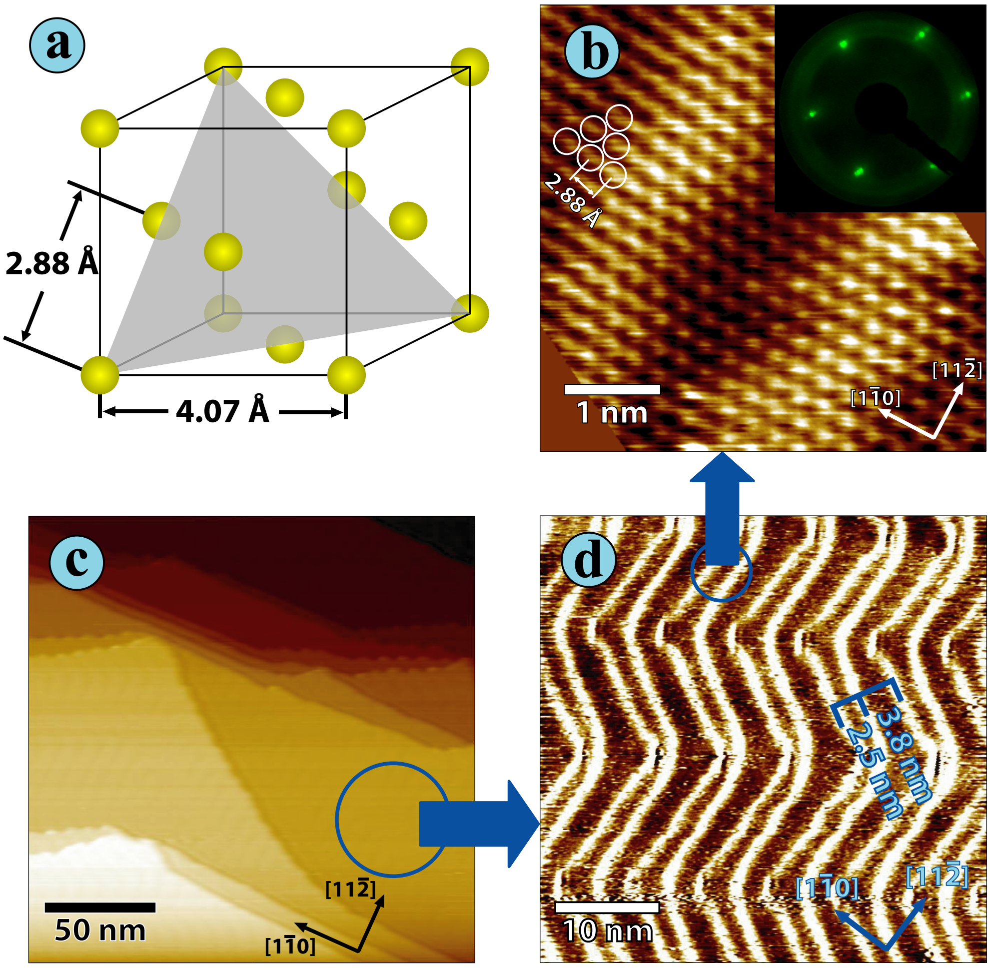

Figure 5.2: Au(111) model and STM-images. (a) Schematic model of the crystal lattice. (b) High resolution image revealing single gold-atoms of the hexagonal surface lattice. The variation in brightness is caused by the herringbone reconstruction. ($U_t = -0.3\,\mathrm{V}$, $I_t = 1.4\,\mathrm{nA}$) In the inset a LEED image of the surfac taken at 110.0 eV electron energy is shown. (c) Step edges of the crystal surface. ($U_t = -0.5\,\mathrm{V}$, $I_t = 0.5\,\mathrm{nA}$) (d) Herringbone reconstruction of the Au(111) surface. ($U_t = -0.09\,\mathrm{V}$, $I_t = 1.0\,\mathrm{nA}$)

5.1.2 6T/Au(111)

As the starting point a nominal mass thickness of 1 Å was deposited onto the Au(111) surface, which corresponds to sub-monolayer coverage. At this film thickness no ordered molecular clusters or domains were observed on the substrate terraces. To explain this absence, two possible reasons typically apply at such low molecular coverages. First, it is expected that the area density of these ordered domains is rather low due to pronounced diffusion and aggregation of 6T molecules on the surface. Since characterization of surfaces with STM includes only a finite number of defined sample points and the area imaged at these points is quite small, it might happen that ordered domains were simply not found within the experiments. Furthermore, another reason for the apparent absence of molecular clusters at low coverages is frequently observed. At room temperature molecules are often just too mobile to be imaged with STM. They are diffusing laterally on the surface in a 2D molecular gas phase, merely increasing the overall tunneling background [77, 78]. When cooling the sample down significantly, molecules can be freezed out on the surface. Indeed, single 6T molecules adsorbed at terraces have been observed at substrate temperatures below 10 K [79]. However, along some of the substrate step edges bright features, separated by dark ones, were found (Figure 5.3a). The average length of the bright features is about (2.6 ± 0.2) nm, which is in good agreement with the length of a single 6T molecule. Therefore they are attributed to 6T molecules stabilized at the Au(111) step edges. Interestingly, every second feature along the step edge appears dark. The average distance between two bright features is (3.7 ± 0.2) nm, which corresponds to the length of one dark feature. Hence, the one dimensional periodicity of the molecules is 6.3 nm, in full agreement with the periodicity of the herringbone reconstruction. In fact the herringbone corrugation lines are also visible in Figure 5.3a, but possess only poor contrast due to the limits of the color scale when displaying several steps. To avoid this problem, part of the image is shown at top of Figure 5.3c after additional flattening of the data. There the corrugation lines of the herringbone are clearly visible and have been highlighted by black lines at the right. Additionally, the molecules have been pigmented in yellow and marked by black ellipses to clarify their relative arrangement. Obviously the positions of 6T molecules are clearly correlated with the smaller-distance line periodicity of the Au(111) herringbone reconstruction, i.e. hcp-packed areas. Consequently, the STM image (Figure 5.3a) suggests that interrupted 6T molecular chains are stabilized along Au(111) step edges modulated by the Au(111) surface reconstruction. This leads to the occupation of only every second available position, namely the hcp-packed areas, which obviously is energetically preferred

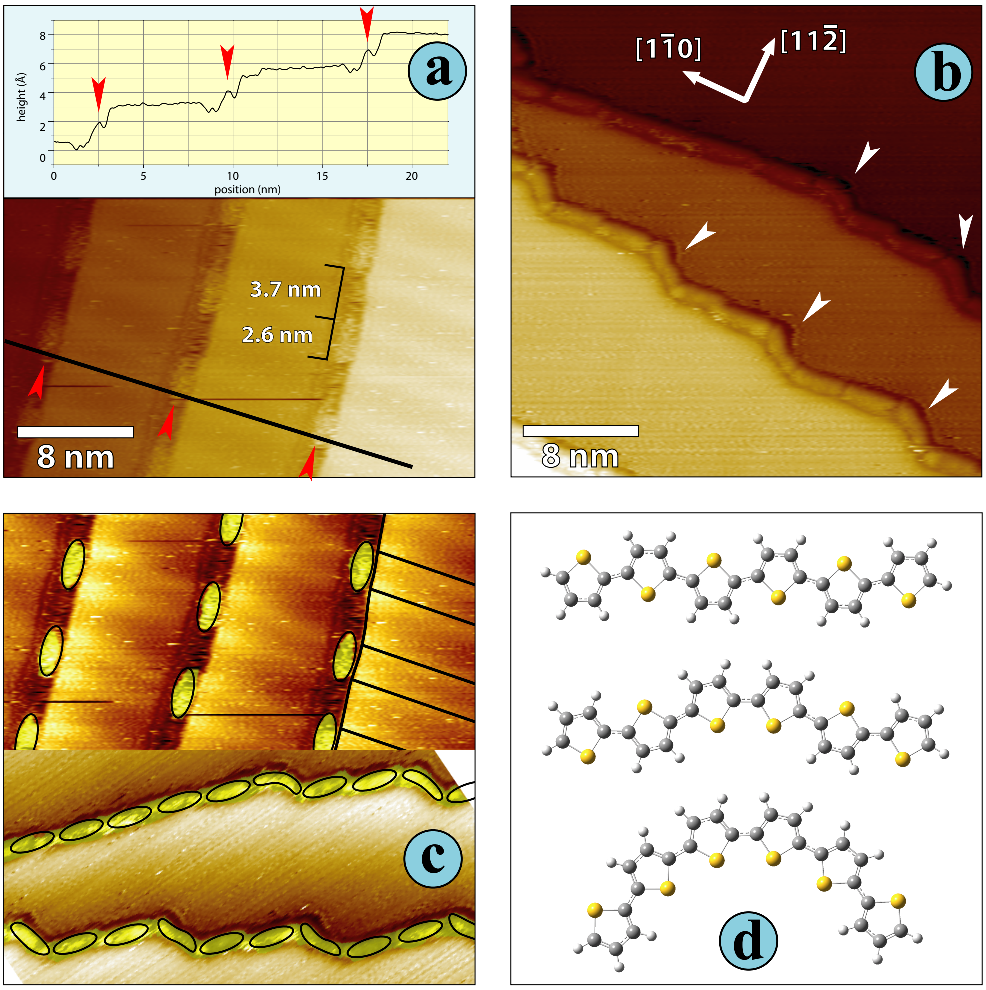

Figure 5.3: STM images of sub-monolayer coverage 6T on Au(111). (a) Single molecules occupying every second position along the substrate step edge. ($U_t = -1.5\,\mathrm{V}$, $I_t = 0.06\,\mathrm{nA}$) The inset shows the line profile corresponding to the black line. Positions of the molecules are marked by red arrows. (b) Closed 6T chains along the step edges. ($U_t = -1.6\,\mathrm{V}$, $I_t = 0.15\,\mathrm{nA}$) Positions where molecules are bend to fit the shape of the edge are marked by white arrows. (c) Cutouts of the images in (a) and (b) with enhanced contrast. Additionally, molecules are marked by black ellipses and at top right reconstruction lines are also highlighted by black lines. (d) Different 6T geometries used to calculate the energy difference between straight and bent conformations.

over fcc-packed ones. At top of Figure 5.3a the line profile corresponding to the black line in the image below is shown. Single 6T molecules are marked by red arrows, proving that molecules are residing at the bottom of the step edge, which nicely confirms the previously proposed notion that 6T layers on Au(111) terraces start to grow from the bottom of step edges [68]. A similar behavior has been reported for other systems such as Cu-phthalocyanine on Au(111) [80], perylene-3,4,9,10-tetracarboxylic-3,4,9,10-dianhydride and N,N'-dimethylperylene-3,4,9,10-bis(dicarboximide) on Ag(111) [81] and C_{60} on Au(11 12 12) [82], where the molecules also formed chains sitting next to step edges, in the last specific case on fcc sites.

Within the same deposition just at other positions on the sample, also closed chains along step edges were found as shown in Figure 5.3b. There the dark features discussed previously are filled with molecules, too. Obviously, after occupying all hcp-sites the next preferred absorption site is given by the fcc positions along the step edges. Nevertheless, all molecules exhibit the same tunneling contrast, irrespective of their position. Notably, the step edge shown in Figure 5.3b has no straight shape but offers a couple of parallel shifts in $(11\overline{2})$-direction. Surprisingly, the molecules sitting at such positions follow the exact shape of the step edge (indicated by arrows in Figure 5.3b). Obviously, to fit to the step edges they deviate from their straight conformation, which they possess in the gas phase as well as in the bulk. A contrast enhanced image with the molecular shape highlighted by black lines is shown at bottom of Figure 5.3c. Bent conformation can be simply achieved by rotations around the inter-ring C-C bonds by 180°. This change in molecular conformation requires energy, which in turn must be gained by the specific interaction around a curved step edge. In order to estimate a lower limit of this energy, the difference in energy of three individual conformations of 6T, as shown in Figure 5.3d, were calculated. Apart from the straight conformation (top), as optimized in the gas phase, the molecule was rotated around the central C-C bond by 180° (middle) and additionally around the two next to central inter-ring bonds again by 180° (bottom). Although, the last conformation is not found as such in STM, it is taken into account to get a feeling of the energies needed for the conformational changes. As it turned out, the energy required per inter-ring rotation was smaller than 40 meV in all cases. As this value was obtained by subtracting the energies of two different molecular conformations, negligible errors due to possible underestimations of total molecular energies [83] are expected as bond orders for all conformations were conserved. This energy can be regarded as lower limit for the stabilization energy gained by a 6T molecule adopting a bent conformation to follow the Au-step edge. Indeed, this energy is rather close to the thermal energy at room temperature, which

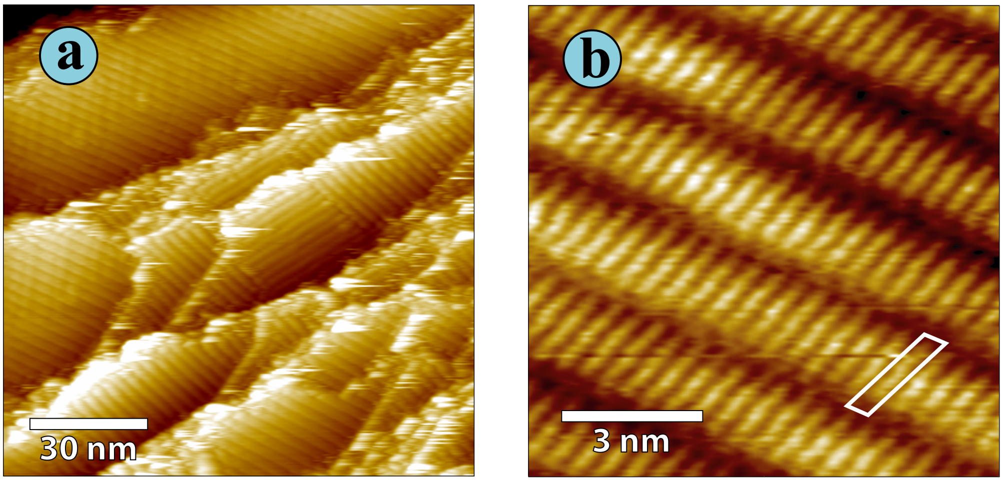

Figure 5.4: STM images of monolayer 6T on Au(111) revealing a continuous 'molecular carpet'. (a) 6T domains extending over several step edges of the substrate. The orientation of molecular rows within one domain depends on the orientation of the step edge where the initial 6T chain is formed. One exception from this growth motif is found in the middle of this image (for discussion see text). ($U_t = -1.4\,\mathrm{V}$, $I_t = 0.2\,\mathrm{nA}$) (b) Magnification of the ordered molecular layer. The white box marks the unit cell calculated from this structure, which contains one molecule. ($U_t = -1.4\,\mathrm{V}$, $I_t = 0.2\,\mathrm{nA}$)

is about 26 meV. Since the bent 6T molecules yielded highly stable STM images even at room temperature, the actual stabilization energy may well be larger. In fact, Liu *et al.* [84] reported that the adsorption energy of a thiophene molecule on a Au(111) defect site, such as a step edge, is ca. 85 meV larger than the adsorption energy on a terrace. This fully supports the STM observation and the calculated energy required for the 6T conformation changes (<40 meV per inter-ring bond rotation) along step edges. In addition, a non-negligible energy barrier may exist for thiophene units to switch between the two different conformations. In the general context of 'molecular wires', the ability of 6T to adopt the shape of the Au step edge by changes in molecular conformation is remarkable, since most reports on wires made of organic molecules feature mainly straight lines that do not conform to a substrate mediated bent shape [85–87].

As the next step, the nominal 6T coverage was doubled to 2 Å. Subsequent STM measurements revealed that this was sufficient to form a continuous layer of 6T on Au(111). Two examples of the structures found at the surface are shown in Figure 5.4. Apparently, the molecules form highly ordered structures which cover the whole terraces. In Figure 5.4a several domains are visible which extend over several step edges. Within each domain the molecules arrange in parallel rows. A magnification of such domain is displayed in Figure 5.4b. Single molecules can be clearly identified in this image. Obviously, 6T molecules lie parallel to each other in the direction of their long molecular axes, while in the direction of their short molecular axes they are perfectly aligned with the next neighboring molecule. The unit cell derived from this structure is $a = (2.3 \pm 0.2)\,\mathrm{nm}$ and $b = (0.5 \pm 0.1)\,\mathrm{nm}$ including an angle of $\alpha = (65 \pm 2)^\circ$. Apparently, the molecules pack rather tight in this structure, as the size of the unit cell already matches the footprint area of a single flat-lying molecule. From STM images of larger areas and the study of many different sample points it can be concluded that this ordering persists also on large terraces. In almost every case the molecular domain starts to grow straight from the bottom of the next higher step edge extending to the next lower one as it is evident from Figure 5.4a. This perfectly matches with the previously found behavior, i.e. molecules adsorbing at the step edges, which then serve as the initial nucleus for directed self-assembled growth. Notably, in about the middle of Figure 5.4a one domain with different orientation is visible, which includes molecular rows rotated by nearly 90° compared to the rows in neighboring domains. Most probably the growth of this domain was initiated at a defect site within the terrace. This confirms the assumption, that the growth direction is defect mediated. As already mentioned, the rotated domain in the middle of Figure 5.4a was the exception, as all other domains where aligned with respect to the adjacent next higher step edge. Apparently, the two dimensional, defect mediated self-assembled growth of the molecular layer is commonly directed by the initial one dimensional molecular chains at the step edges.

Under certain conditions, STM images of the domains on a larger scale enabled the observation of the underlying herringbone reconstruction of the Au(111) substrate at the same time, as shown in Figure 5.5. When using tunneling parameters which were optimal for imaging the molecules, usually the herringbone reconstruction provided only weak contrast in STM images as is the case in Figure 5.5a. Nevertheless, the contrast in this image can be significantly enhanced by first separating the different features in the Fourier-transformation, then coloring them differently and as last step overlay them again. The result of this processing is shown in Figure 5.5b where yellow rods present the molecular layer while the herringbone in the background is gray. From this contrast enhanced image the relative alignment of the molecular layer with respect to the herringbone reconstruction can be derived. There an angle between the reconstruction lines of the herringbone and the long molecular axis of about $\delta = (83 \pm 3)^\circ$ is found (cf. Figure 5.5b). No clear

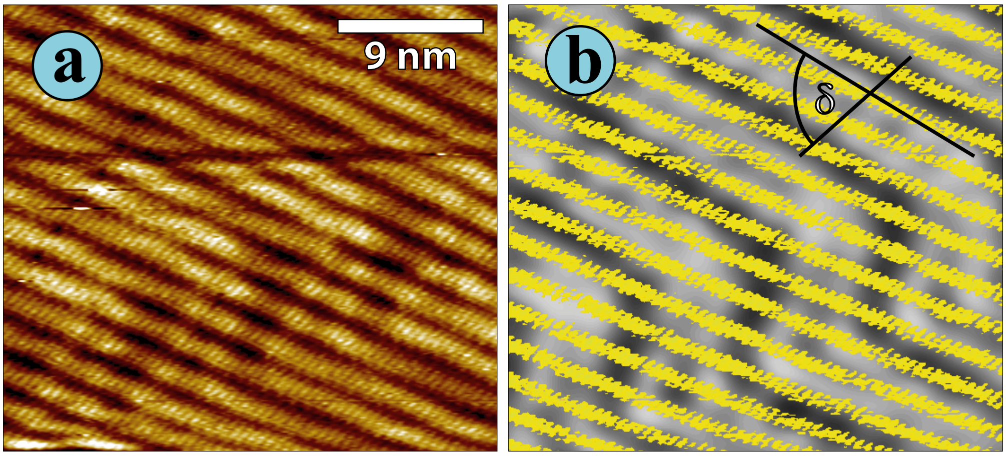

Figure 5.5: STM images of 6T monolayer where the underlying Au(111) herringbone reconstruction is visible simultaneously. (a) The reconstruction is visible as slight height variations. ($U_t = -1.4\,\mathrm{V}$, $I_t = 0.2\,\mathrm{nA}$) (b) Same image as (a) with enhanced contrast by applying different coloring to by Fourier transformation formerly separated parts.

alignment of the molecular layer with respect to the substrate reconstruction is observed. Instead, the monolayer is obviously not influenced by orientation changes of the substrate's herringbone reconstruction, derived from the fact that the rows do not follow the direction of the herringbone. Consequently, the interaction between the 6T monolayer and the reconstructed gold surface has to be lower than the inter-molecular interaction. Starting from molecules adsorbed at the step edges, subsequent molecules align to already stabilized ones, forming large ordered domains, rather than taking care of the underlying substrate reconstruction.

After increasing the nominal amount of 6T molecules up to 8 Å the structures observed in STM had mostly the same appearance like already found for the monolayer deposition. Additionally, a new structure was observed at some points of the sample. A STM image showing both structures at the same time is presented in Figure 5.6. In this image, molecules which correspond to the structure discussed for the monolayer are found on the right as well as at the bottom of the image on the next higher terrace. A magnification of this area (marked by box B) is shown at the right of the image. In contrast, in the left part of the STM image appears an area with a less dense packing of molecules. The according magnification (marked by box A) is also presented at the right. Apparently, only every second position along one molecular row is occupied by a molecule in this structure. This can be explained by the model shown on the very right. As it was already found,

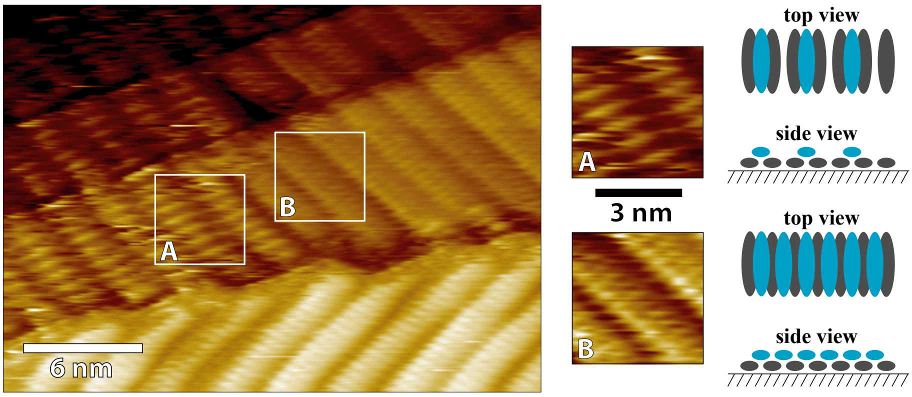

Figure 5.6: STM image of two different 6T layer appearances within a molecular film at nominal mass thickness of 8 Å. ($U_t = -1.2\,\mathrm{V}$, $I_t = 0.3\,\mathrm{nA}$) Appropriate magnifications of the areas label A and B are presented at the right. The according model of the molecular arrangement is shown next to it.

the molecules within the monolayer tend to maximize the packing density by aligning their molecular bodies next to each other. By putting molecules on top of this layer, two general growth motifs are possible. First, the next layer could grow perfectly like the first one with the molecules on exactly the same positions, but just shifted in the third dimension. Second possibility would be, that molecules in the next higher layer are always occupying the positions in between two molecules of the underlying molecular layer. This scenario is sketched at the bottom right of Figure 5.6. This way the molecular interaction is maximized and maximum packing density is retained. Therefore, the second packing motif would lower the overall energy of the system and should be preferred over the first model. Now, the structure in the left domain of Figure 5.6 (box A) can be easily explained by the assumed packing model. In this case only every second position is occupied by a 6T molecule (sketched on the right top in Figure 5.6). Due to the interaction with two molecules of the underlying layer, the stabilization of a molecule at these point is already sufficient. Therefore, the observation of the structure in box A fully matches with the assumptions of the proposed packing model. Overall, the ordering in up to about the third to fourth layer was found to remain the same as already observed for the monolayer.

Under good tunneling conditions, which are mostly defined by the tip shape, the observation of sub-molecular features was possible. There two different appearances were found, which are displayed in Figure 5.7. In Figure 5.7a three bright spots are visible within a single molecule. Similar obser-

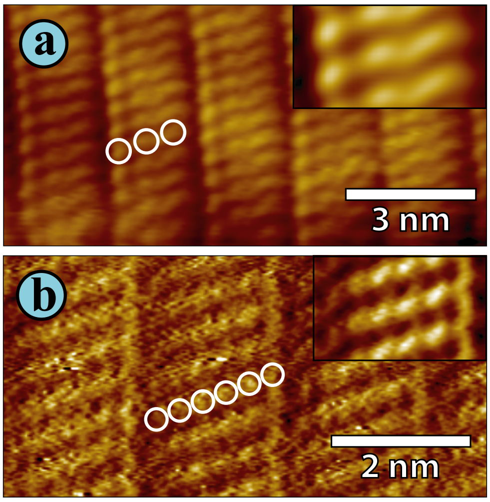

Figure 5.7: STM images of 6T showing sub-molecular contrast. The appropriate insets present the molecular structure derived from correlation averaging of the large images. (a) Molecules with three clearly visible inner structures. ($U_t = -1.1\,\mathrm{V}$, $I_t = 0.6\,\mathrm{nA}$) (b) Current image exhibiting six inner structures within one 6T molecule corresponding to the six thiophene rings of 6T. ($U_t = -2.0\,\mathrm{V}$, $I_t = 2.0\,\mathrm{nA}$)

vation was reported by Mäkinen *et al.* [68], also for 6T on Au(111). There it was explained by interference effects between the metal surface and the molecules. However, the tunneling conditions, determined mainly by the tip shape and tunneling parameters, play the most important role for the contrast and therefore the appearance of molecules in STM experiments. This is exemplified by a second type of sub-molecular contrast observed for the same sample, which clearly shows six inner structures within one molecule (Figure 5.7b). This perfectly corresponds to the six individual thiophene units of 6T.

5.1.3 DH6T/Au(111)

In order to achieve a systematic comparison of 6T with its alkylated derivate DH6T, the same approach has been chosen. First, a molecular amount in the sub-monolayer range was sublimed onto Au(111). Unfortunately at this regime no molecules were found on the sample, even though considerable effort has been spend on finding them. Neither at the step edges nor on the terraces any indication of molecules was observed. Here the same explanation, as given for sub-monolayer deposition of 6T, holds. Although, as

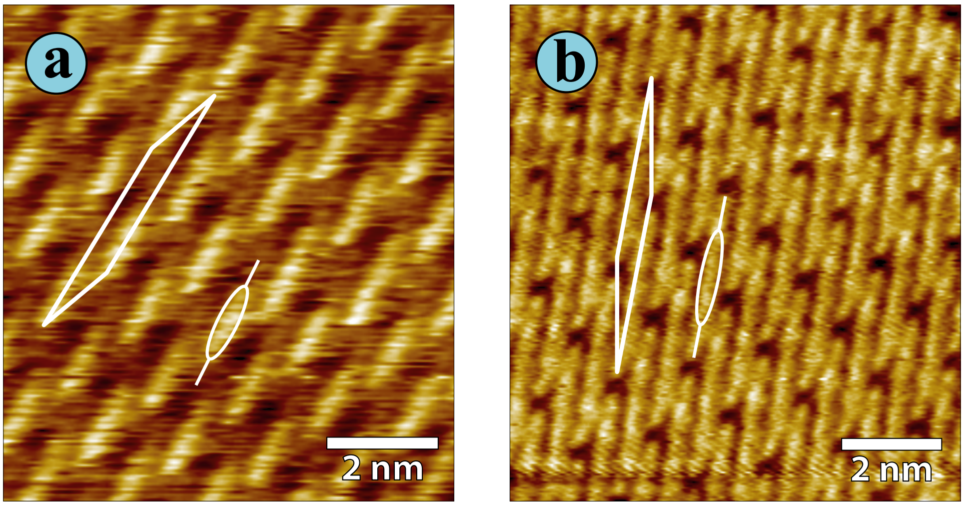

Figure 5.8: STM images of monolayer DH6T on Au(111) at two different imaging contrasts. White boxes indicate the appropriate unit cell, whereas the white ellipse marks the 6T core of one molecule with white lines presenting the alkyl chains. (a) Only the 6T cores of the molecules are visible. ($U_t = -0.5\,\mathrm{V}$, $I_t = 0.4\,\mathrm{nA}$) (b) Brick like appearance of DH6T where hexyl chains also contribute to the tunneling current. ($U_t = -1.0\,\mathrm{V}$, $I_t = 0.3\,\mathrm{nA}$)

usual for STM, the existence of molecules at step edges somewhere on the sample surface can not be excluded completely, the absence of such structures in the experiments might already indicate that the step edges are not preferred adsorptions sites for DH6T. Consequently, the deposition of DH6T was increased to about 2 Å nominal mass thickness. Analogous to the 6T experiments, at this coverage completed monolayers were observed as displayed in Figure 5.8. Depending on the tip and tunneling conditions, the molecules showed two different appearances. In the first case, corresponding to Figure 5.8a, bright rods surrounded by comparatively dark areas were found. Determination of the length of the bright parts with $(2.2 \pm 0.2)\,\mathrm{nm}$ revealed them to correspond to the 6T cores of DH6T. Apparently, the alkyl chains are simply not contributing to the tunneling current, making them invisible in the STM image. This was the common appearance of DH6T. Under certain conditions, which includes not only the tunneling parameters, but was apparently also accompanied by a sudden change of the tip, a second appearance was observed as presented in Figure 5.8b. In this case molecules show up as long bright sticks forming a very compact structure. The length of these sticks with $(3.7 \pm 0.2)\,\mathrm{nm}$ already corresponds to the length of DH6T including the alkyl chains. Interestingly, here the alkyl chains are not only visible, but furthermore no difference in contrast compared to the 6T core can be distinguished. However, the unit cell in both cases is absolutely identical, with $a = (3.7 \pm 0.2)\,\mathrm{nm}$, $b = (1.5 \pm 0.1)\,\mathrm{nm}$ and $\alpha = (18 \pm 2)^\circ$ as indicated by the white boxes in Figure 5.8. For clarification of the molecular position DH6T is additionally sketched as ellipse presenting the 6T core and white lines marking the alkyl chains in the appropriate images. Compared to the 6T monolayer a significant difference in the arrangement of the molecules relative to each other is observed. While the molecules are still aligned parallel to each other along their long molecular axes, the conjugated cores of neighboring molecules are shifted relative to each other along this direction. Overall this ordering leads to a brike-wall-like appearance. This way neighboring molecules have very limited side-by-side overlap of thiophene units.

The monolayer structure of DH6T/Au(111) is in pronounced contrast to that observed for DH6T on highly oriented pyrolytic graphite (HOPG), which revealed a completely different packing [71]. There the molecules where also found lying flat on the surface, but in a lamella-like structure, comparable to what was found for 6T on Au(111) (section 5.1.2). Obviously, the interface between DH6T and HOPG allows an efficient side-by-side arrangement of the conjugated molecular moieties in contrast to DH6T on Au(111). Interestingly, maximized phase separation between saturated and conjugated molecular parts was also reported for DH6T assembled in thin films on Si [70]. Thus, the metal substrate Au(111) led to an entirely different packing motif, where hexyl and thiophene units exhibit maximized intermixing in two dimensions. This leads to a surface that exposes regularly mixed saturated and unsaturated patches on a molecular level, which may possibly be exploited for future directed self-assembly strategies.

On larger scale another interesting observation was achieved as presented in Figure 5.9. Apparently, the herringbone reconstruction of the underlying substrate is visible even more clearly than found for 6T/Au(111) (cf. Figure 5.5). Additionally, in Figure 5.9a several different domains can be identified which seem to depend on the herringbone reconstruction. A magnification of the area marked by a box in the upper left corner is shown in Figure 5.9b. Here, molecules forming lines along their long molecular axis as well as single molecules can be clearly identified. Apparently, the orientation of these molecular lines depends on the orientation of the underlying herringbone structure, leading to the formation of different domains. Kinks of the herringbone thereby define the boundaries between neighboring domains. Within one domain an constant angle of $\delta = (77 \pm 3)^\circ$ between the corrugation lines and the molecular long axis is found (cf. Figure 5.9b). Although, at first glance this value seems to be very similar to what was found for 6T

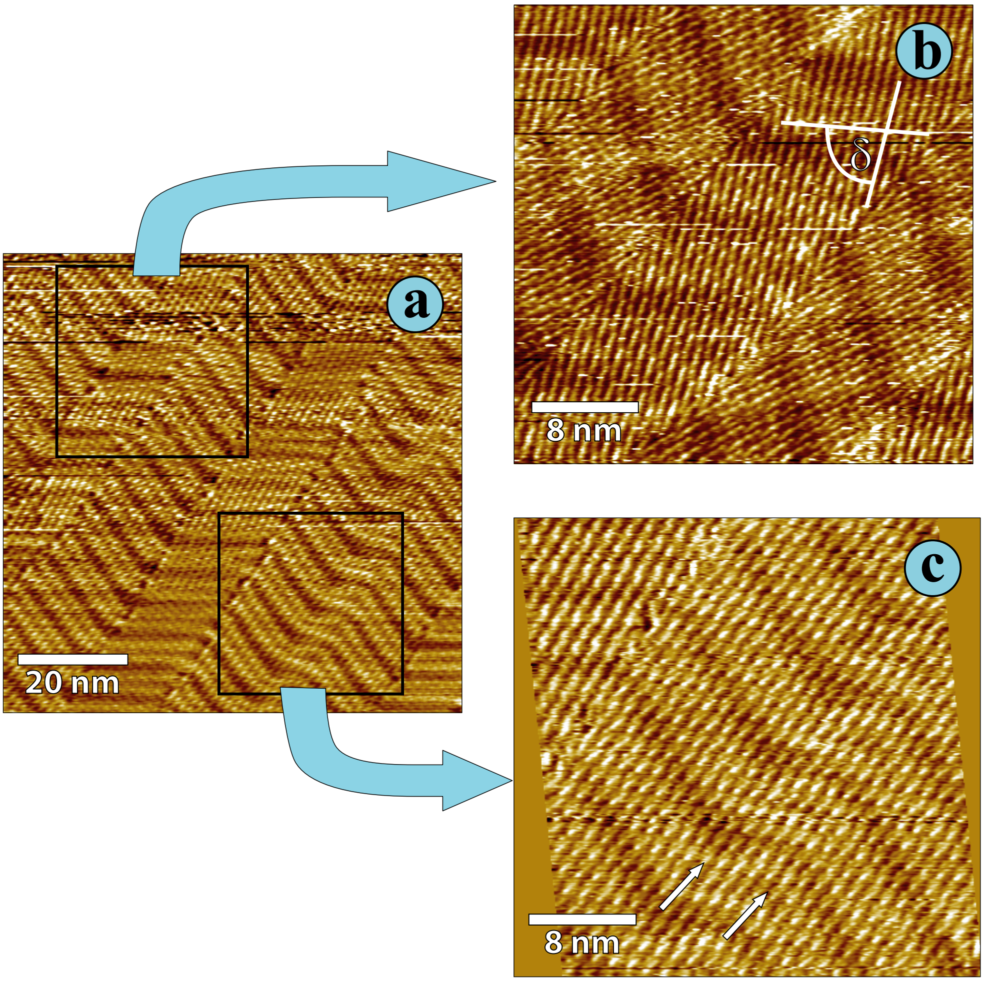

Figure 5.9: STM images of monolayer DH6T/Au(111) on larger scale, revealing also the underlying herringbone reconstruction. (a) Several different domains of molecular orientation are visible. The squares mark areas from which magnified images are shown in (b) and (c) accordingly. ($U_t = -1.1\,\mathrm{V}$, $I_t = 0.3\,\mathrm{nA}$) (b) The orientation of molecular lines clearly depends on the herringbone orientation. ($U_t = -1.1\,\mathrm{V}$, $I_t = 0.3\,\mathrm{nA}$) (c) The underlying herringbone exhibits a short distance double-kink (marked by arrows), which apparently does not influence the molecular orientation. ($U_t = -1.0\,\mathrm{V}$, $I_t = 0.3\,\mathrm{nA}$)

on Au(111), one has to remember that 6T did not take care of the underlying herringbone reconstruction. Consequently, the ordering of the DH6T molecular domain is significantly influenced by the underlying herringbone orientation, leading to a patch-work like appearance of the molecular layer in contrast to the continuous growth of 6T layers. Interestingly, in some special cases, exceptions from this growth regime were found. One exception is visible in the lower right corner of Figure 5.9a and a magnified image of this area is shown in Figure 5.9c. Here a double-kink of the herringbone reconstruction can be identified (marked by the arrows in Figure 5.9c), which apparently does not influence the ordering in the molecular layer on top. Usually, the typical distance between two neighboring Au(111) reconstruction kinks is about $(15 - 20)\,\mathrm{nm}$. In this particular case the distance is only ca. $6\,\mathrm{nm}$. As shown in a previous work by Tracz *et al.* [88], an ordered domain can only exist if the available area is large enough to accommodate the critical nucleus size. Typically three to five molecules are needed to reach this critical nucleus size [88]. Presumably, in the specific case shown in Figure 5.9c, the size of the critical nucleus is larger than the distance of two neighboring domains, which prevents the formation of a stable nucleus at this position.

Apparently, by the addition of alkyl chains to the conjugated core, the nucleation at step edges is suppressed. Instead, the kinks of the herringbone reconstruction define the nucleation sites and act as boundaries between different domains. Therefore, in this case the molecule-substrate interaction exceeds the inter-molecular interaction strength. Additionally, the alkyl chains lead to maximized intermixing of saturated and conjugated parts of the molecule.

At higher nominal coverages, which should be sufficient for the formation of a second and third layer, no new structures were observed. Possibly, higher order layers have exactly the same appearance as the first layer, similar to the behavior already found for 6T. Due to the fast attenuation of the substrate influence with increasing distance from the surface, this is not very likely. Another explanation is that higher layers could not be imaged in STM. With increasing distance from the surface the tunneling current decreases drastically. Taking into account the relatively bad conductivity of DH6T, the contribution of DH6T to the tunneling current from higher layers is rather low. As a consequence, the tunneling tip easily penetrates into the higher layers, without the feedback electronics being able to notice this. Still, stable tunneling conditions are derived close to the surface. Consequently, images taken at higher nominal coverage may still show the first layer instead of the top most, as this one exhibits the strongest contribution to the tunneling current.

Finally, also for DH6T sub-molecular contrast was observed. One appro-

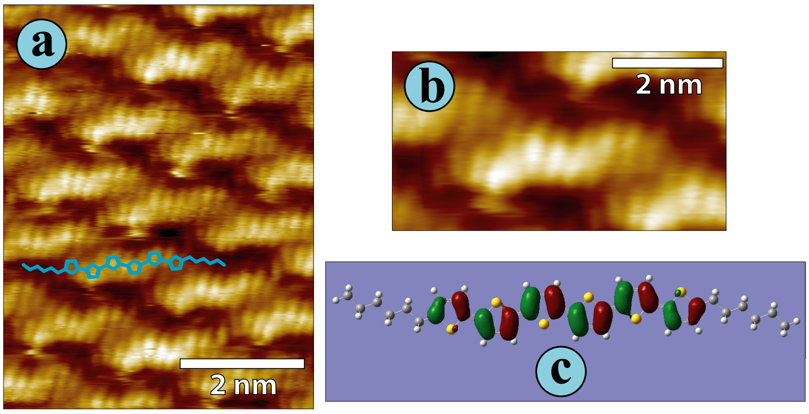

Figure 5.10: (a) STM image of DH6T on Au(111) revealing sub-molecular contrast with 12 inner structures. (U_t = −1.1 V, I_t = 0.3 nA) (b) Image of DH6T derived by correlation averaging of (a). (c) Calculated HOMO of DH6T.

priate image is shown in Figure 5.10a and a magnified molecule derived by correlation averaging in Figure 5.10b. In this case again, the alkyl chains remain invisible, leaving only the 6T core contributing to the tunneling current. Interestingly, 12 bright rod-like features are visible under these tunneling conditions instead of 6 as found for non-alkylated 6T (cf. Figure 5.7b). Comprising 6 thiophene units in the core, this corresponds to two bright features per thiophene ring. For comparison, in Figure 5.10c the calculated HOMO of DH6T is shown. There, exactly 12 lobes appear, which perfectly match with the 12 features derived from the STM observation. The small inclination between the molecular-orbital-derived lobes and the long molecular axes in the STM image, are possibly attributed to the convolution of the orbital shape and that of an elongated tip (the tip-sample geometry is fixed in the experiments). Apparently, the bright lobes do not form a straight line, but resemble a wavelike shape. This is expected for 6T cores where thiophene units are in the energetically favorable conformation as shown in the schematic of the DH6T HOMO (i.e. sulfur atoms of neighboring thiophene rings pointing in opposite directions, cf. Figure 5.10c) and thus nicely corroborates the assignment of these features to the DH6T HOMO.

5.1.4 Conclusions

The two oligothiophenes sexithiophene (6T) and its alkylated analog α,ω-dihexylsexithiophene (DH6T) adsorbed on Au(111) were investigated by STM.

Evidence is provided that alkyl-chain substitution of a conjugated molecule can have a dramatic impact on a number of fundamental physical properties of adsorbed layers. It was found that metal substrate step edges were preferred absorption sites for 6T, resulting in the stable formation of 6T chains of single-molecular width. In order to follow the overall shape of the edges, some 6T molecules exhibited bent conformations due to C-C bond rotations between neighboring thiophene units. These initially adsorbed molecules determined the growth direction of domains at higher coverage. Because the monolayer was apparently not affected by changes of the underlying herringbone structure, it was concluded that the lateral layer growth is dominated by stable nucleus formation at the Au step edges. In contrast, for DH6T only closed monolayers were observed, whose domain orientation relative to the substrate was strongly affected by the direction of the Au(111) surface herringbone reconstruction. Corresponding domain boundaries within the organic layer were present at kinks of the Au(111) herringbone reconstruction. Thus, the formation of stable nuclei for DH6T occurred at these kinks of the surface reconstruction, in contrast to the case of 6T. Within the DH6T monolayer, the conjugated molecular parts of neighboring molecules were separated from each other by hexyl chains, leading to a regular nano-pattern of conjugated and saturated surface-exposed patches. This surface-induced pattern formation on a molecular scale, which is markedly different from that of the bulk material, may be exploited in future directed self-assembly schemes.

5.2 Monolayer/Multilayer transition

In the previous section it was shown that the ordering behavior of molecules is very sensitive on the ratio between inter-molecular and molecule-substrate interaction strength. Since the influence of the substrate is strongly decreasing with increasing distance from the substrate surface, changes of the structural and electronic properties within the molecular layer are expected with increasing film thickness. To study this transition a prototypical molecule was chosen, which is called hexa-*peri*-hexabenzocoronene (HBC). The chemical structure of HBC is presented in Figure 5.11a. The molecule consists of thirteen benzene rings, where one benzene in the center is equally surrounded by the other twelve. Because of the disc-like structure and high-symmetry of this molecule, HBC has been shown to form highly ordered layers on many substrate materials, including, e.g., HOPG [90], Cu(111) [91], and Au(111) [92]. Interestingly, in the bulk crystal HBC was reported to pack in columns with the molecular discs in one column being tilted in one direction with respect

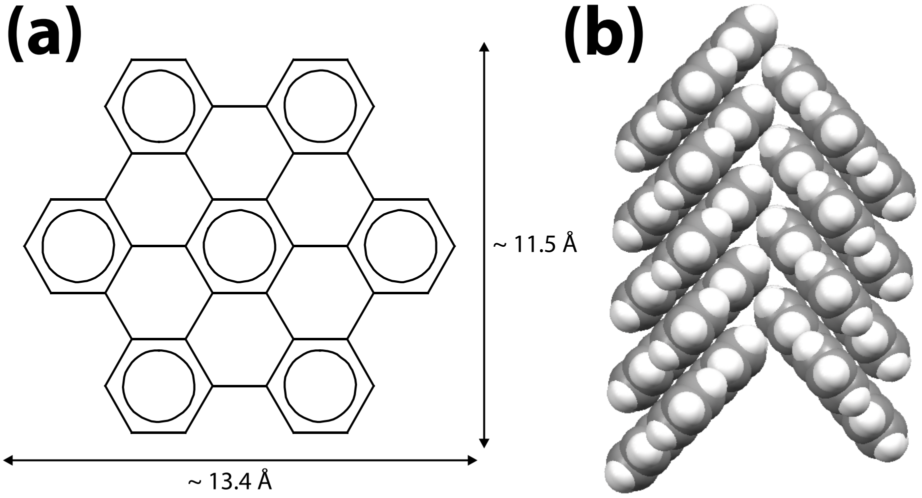

Figure 5.11: (a) Chemical structure of hexa-*peri*-hexabenzocoronene (HBC, $C_{42}H_{18}$). Numbers of the molecular size include the hydrogens, which are not painted. (b) Crystal packing of HBC viewed perpendicular to the mean plane through the molecules as found by Goddard *et al.* [89].

to the column normal, whereas in neighboring columns, the tilt direction is contrary [89, 93, 94]. The resulting herringbone packing is shown in Figure 5.11b. Because of the parallel stacking of the molecular π-systems in this structure, large charge carrier mobilities along the columns are expected [95]. An alkyl substituted derivate of HBC, hexakis-dodecyl-hexabenzocoronene (C_{12}HBC), has already been shown to exhibit a high one-dimensional charge carrier mobility of $0.5\,\mathrm{cm}^2\mathrm{V}^{-1}\mathrm{s}^{-1}$ [96]. The bulk structure of molecular crystals is usually achieved within thick molecular films. Therefore, the transition of structural and electronic properties from the monolayer to the multilayer of HBC is of special interest. Unfortunately, in the previous mentioned references such behavior was not reported. Consequently, in this work Ag(111) was chosen as substrate material, which was not investigated before. In order to obtain a consistent understanding of the interface behavior of HBC on Ag(111), several complementary techniques were used. The molecular orientation was determined by NEXAFS spectroscopy. To confirm the structural alignment, additional STM measurements were conducted on thin and AFM on thick molecular films of HBC. Information about the electronic structure were derived from UPS measurements.

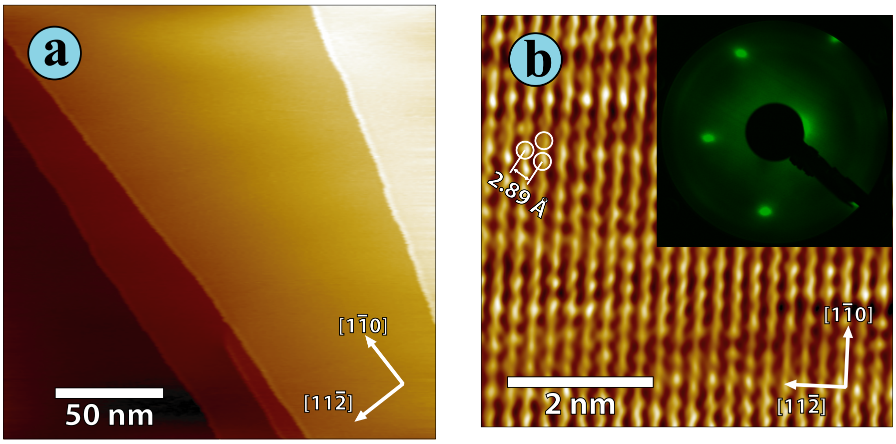

Figure 5.12: STM-images of Ag(111). (a) Step edges of the crystal surface. ($U_t = -0.1\,\text{V}$, $I_t = 0.6\,\text{nA}$) (b) Atomic lattice of the surface. To improve the image quality additional Fourier filtering was applied. ($U_t = -0.3\,\text{V}$, $I_t = 0.6\,\text{nA}$) In the inset a LEED image of the Ag(111) surface taken at 92.6 eV electron energy is shown.

5.2.1 Ag(111)

The silver single crystal is very similar to the gold single crystal. It also exhibits a fcc lattice with lattice constant of $a_{Ag} = 4.09\,\text{Å}$, which is almost the same as found for gold. Consequently Ag(111) also has a hexagonal surface lattice with just slightly different lattice constant of $a_{Ag}/\sqrt{2} = 2.89\,\text{Å}$. A STM image of the surface atoms is shown in Figure 5.12b, where the inset represents the corresponding LEED image. Monolayer steps of Ag(111) feature a height difference of $a_{Ag}/\sqrt{3} = 2.36\,\text{Å}$. Typical terrace width of the crystals used within this work were up to 150 nm (Figure 5.12a). Although, the crystal symmetry is broken at the surface as well, no observable reconstruction occurs. The work function of Ag(111) crystals is 4.6 eV [97].

5.2.2 Molecular orientation

To determine the molecular orientation of HBC on Ag(111), NEXAFS spectroscopy experiments were performed. Due to limited beam time at the appropriate synchrotron endstation only two samples could be analyzed. Therefore, a film thickness of 6 Å was chosen in order to surly derive a monolayer of HBC as first sample. To investigate the multilayer properties a nominal mass thickness of 30 Å was deposited onto Ag(111) as the second sample. Directly after deposition NEXAFS spectra for photon incidence angles α in the

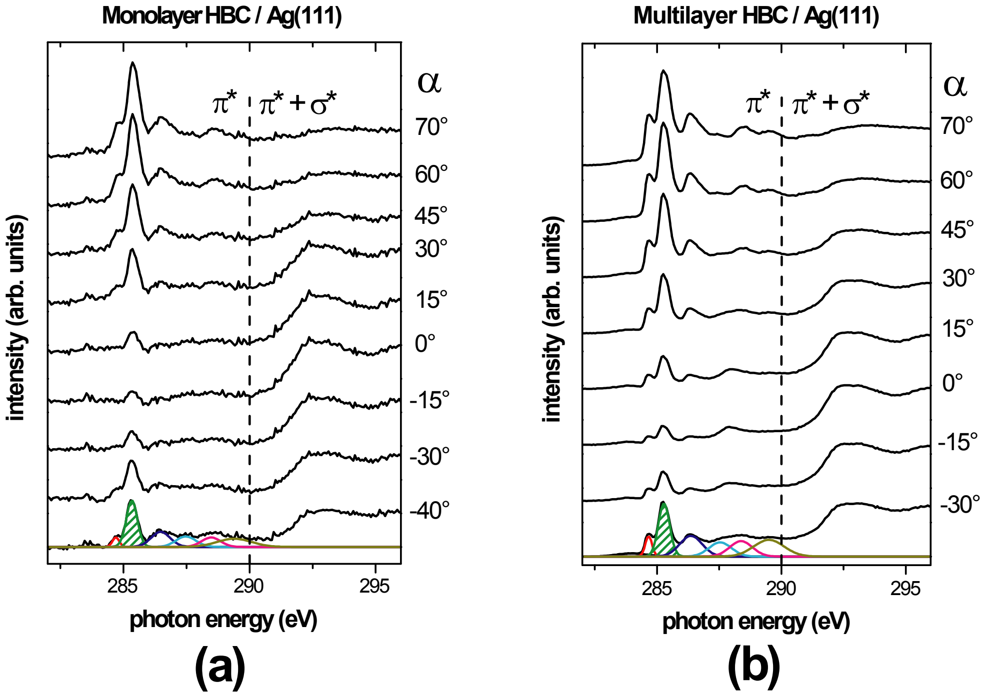

(a)

(b)

Figure 5.13: NEXAFS spectra of HBC on Ag(111) for different angles of photon incidence α for (a) monolayer HBC coverage and (b) multilayer coverage. The bottom spectra additionally show the results of fitting the π^* region with six Gaussian peaks. The peak at 285.3 eV (shaded) was used for quantification of the molecular orientation (see Figure 5.15).

range of $-40° \ldots +70°$ were recorded for both samples, which are presented in Figure 5.13 (for experimental geometry see Figure 5.14a). Several distinct absorption peaks are clearly visible near 285 eV below the C K-edge in both series of spectra. In Figure 5.14b a simulation of the HBC resonances in the same energetic region done by Luo *et al.* is shown [98]. They derived the different spectra by considering the different chemically inequivalent carbon positions within the molecule (shown at top of Figure 5.14b). The superposition of these spectra leads to the topmost spectrum in Figure 5.14b, which agrees well with the measured spectra in Figure 5.13. Note, that the energy scale in the simulation is shifted compared to the real measurement. Nevertheless, the experimental data agrees well with other published NEXAFS spectra of HBC [90], also in the energetic scale. Therefore, the shift in the simulation is just caused by a bad energy calibration. However, with the help of the theoretical calculations, the peaks below 290 eV in the measured spectra can be assigned to π^* resonances from the five inequivalent carbon

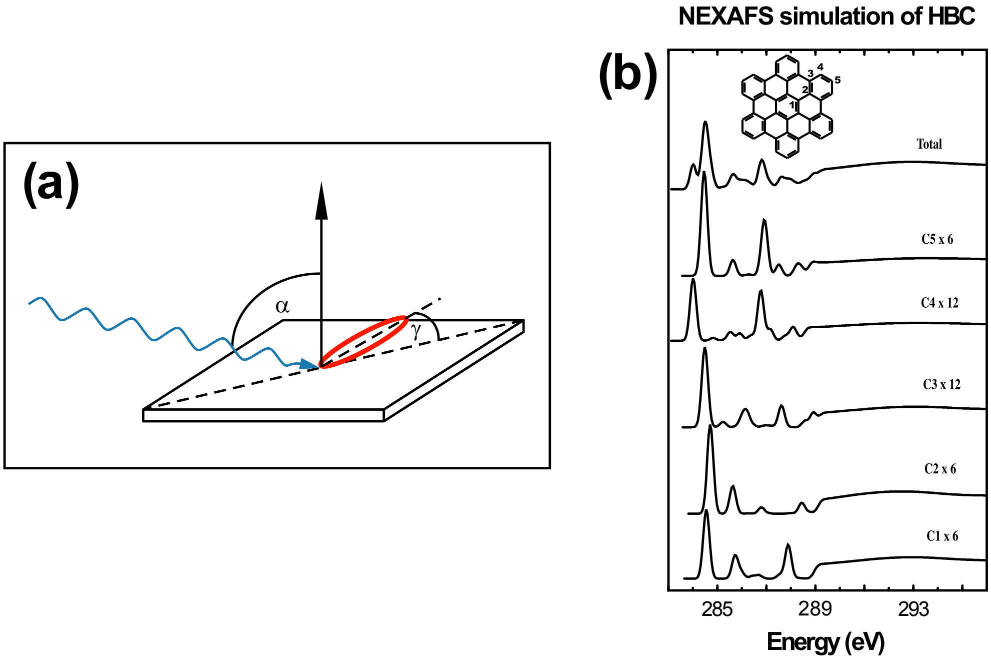

Figure 5.14: (a) Geometry used in the NEXAFS experiments showing the angle of photon incidence α with respect to the surface normal (arrow pointing upwards) and the angle of the molecular plane γ with respect to the sample (square at bottom). The molecule is sketched by the red ellipse. (b) Simulation of HBC resonances in NEXAFS done by Luo *et al.* [98]. At top the HBC structure is shown with different chemically distinguishable atoms marked. According simulated spectra are presented below, obtained by full core hole potential calculations.

sites within a HBC molecule. As evident from the experimental spectra (Figure 5.13), the intensity of the π^* peaks varies with α, and a clear minimum at $\alpha = 0°$, referring to perpendicular incidence, is found for both coverages. As already explained in section 3.4.2, for the transition of an electron from the C K-shell into π^* states (as is the case here), the maximum intensity is observed if the electric field vector of linearly polarized radiation is parallel to the long axis of the π^* orbital [45]. Since the π^* orbitals of HBC are oriented perpendicular to the molecular plane, low absorption intensity at small angles α indicates a small angle γ between the molecular plane and the sample surface (see Figure 5.14a for experimental geometry). Spectral fitting was accomplished by using six Gaussian functions to reproduce the π^* region situated below 290 eV, as shown in the bottom spectra of Figure 5.13. For quantitative analysis, the second peak at 285.3 eV (shaded in Figure 5.13) was chosen because it has the highest intensity and can also be reliably fitted for the 6 Å coverage spectra. The resulting dependence of this peak's area on α is shown in Figure 5.15 for the ca. monolayer (filled red squares) and the multilayer (open blue circles) sample. The relative peak areas were normalized to the one at 36°, for which the intensity is independent of the molecular orientation (cf. equation 3.24). The highest intensity and therefore strongest overlap between electric field vector and molecular π^* orbitals is found for large α, corresponding to small γ. The theoretical dependence of the intensity I_{π^*} on the angles α and γ is given by equation (3.24) already presented in section 3.4.2. For the beamline used at BESSY the degree of photon beam polarization was given with $P = 0.98$. According to this formula fits based on the experimental data are included in Figure 5.15, the bottom solid line (red) for the ca. monolayer and the upper solid line (blue) for the multilayer sample, respectively. For comparison, calculated dependencies according to equation (3.24) for $\gamma = 0°$ and 43° (this particular choice is justified further below) were also included as dotted lines. From the fitting procedure, the angle γ between the molecular plane and the sample plane is simply obtained as a fitting parameter and was determined to $\gamma_1 = (25 \pm 4)°$ for 6 Å coverage, corresponding to about a monolayer, and $\gamma_2 = (31 \pm 2)°$ for 30 Å coverage, corresponding to the multilayer.

Based on this data one could make a simple model now, which will be referred to as model 1. In this model, the HBC molecules in the monolayer regime are already tilted with respect to the sample surface by γ_1, and the tilt angle increases slightly to γ_2 in thicker films as shown in Figure 5.16a. However, this simple model may be easily challenged, since all reports available at present indicate that conjugated molecules in a monolayer favor to align their π-electron systems parallel to a metal surface [25, 69, 99, 100]. Furthermore, both angles, γ_1 and γ_2, do not occur in any known crystal

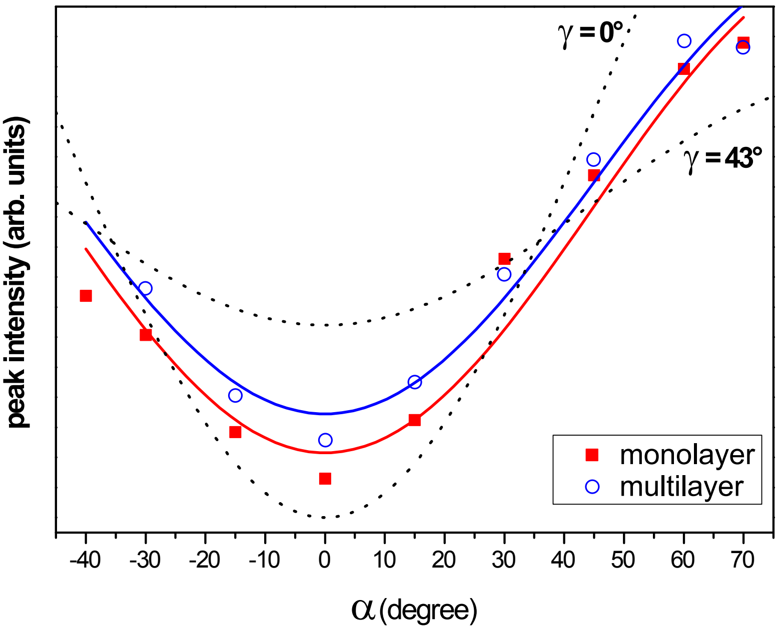

Figure 5.15: Peak intensity (obtained from the peak area of the NEXAFS feature at 285.3 eV in Figure 5.13) as function of the angle of photon incidence α. Filled red squares: ca. monolayer HBC coverage, open blue circles: multilayer HBC coverage. The red (bottom) and blue (upper) solid lines represent the best fits to the data. Dotted lines: calculated curves for $\gamma = 0°$ and 43°, according to equation (3.24).

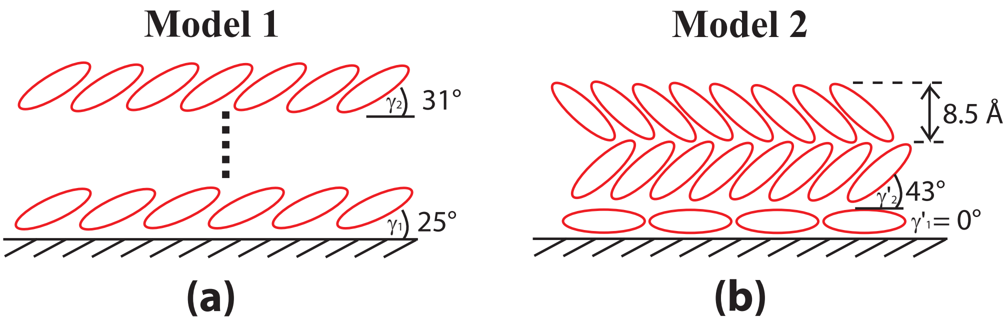

Figure 5.16: Different proposed models for the orientation of HBC on Ag(111) in the mono- and multilayer. (a) Model 1 as derived directly from NEXAFS data. (b) Alternative model 2 supported also by SPM measurements. Further explanation is given in the text.

structure of HBC [89, 93], which requires the presence of two yet unreported HBC polymorphs. Moreover, as a matter of fact, NEXAFS spectra are always composed of the signal of all molecules from which electrons are detected. Hence, the angle derived from the fitting represents an average of all orientations of molecules contributing to the signal. Thus, as an alternative, the HBC films on Ag(111) could be even amorphous with thickness-dependent average angles γ_1 and γ_2, which is rather unlikely for this type of discotic system. Therefore, a further alternative model, which will be referred to as model 2, is suggested, that is built on known fundamental interfacial mechanisms and HBC properties already established in the literature, together with the fact that NEXAFS spectra contain information on more than the topmost molecular layer simultaneously (cf. section 3.4.2). In this model, HBC molecules in the monolayer lie flat on the Ag(111) surface with $\gamma_1' = 0°$, in accordance with general expectations [92, 101]. Molecules in the multilayer have a different orientation because of a reduced interaction strength with the metal surface, which is screened by the monolayer. Well defined and considerable changes in molecular orientation between mono- and multilayer on metal surfaces have been reported, e.g., for pentacene [102, 103] and α,ω-dihexylsexithiophene [99]. For HBC, it can be expected that the multilayer aggregates in the known bulk crystal structure [89], with the substrate surface, now comprising the HBC monolayer on Ag(111), perpendicular to the HBC (010) net plane (see Figure 5.11b and Figure 5.16b). In this scenario, the molecular plane in the bulk crystal forms an angle of $\gamma_2' = 43°$ with respect to the surface plane [89]. The angular dependence of π^* resonances found in NEXAFS spectra are thus interpreted as being due to a superposition of these two molecular orientations in this model as shown in Figure 5.16b. In order to estimate the ratio of flat lying (proportion A) and inclined (proportion B) HBC molecules in the two samples, the data of Figure 5.15 is fitted again, this time as a superposition with the angles γ_1' and γ_2' fixed:

$$I_{total} = AI_{\pi^*}(\gamma_1' = 0°) + BI_{\pi^*}(\gamma_2' = 43°) \tag{5.1}$$

Here I_{π^*} refers again to the intensity of the π^* state given in equation (3.24). Since the number of free fitting parameters in equation (5.1) is identical to that of equation (3.24), the best fits are identical. The resulting proportional factors A and B now provide the possibility to calculate the ratio of the two conformations in the mono- and multilayer as shown in table 5.1. For 6 Å coverage most of the molecules (60 %) contributing to the NEXAFS signal are found to lie flat (proportion A), whereas at 30 Å coverage the ratio is about inverted, leading to the majority of molecules appearing to be inclined. Important to note at this point is that the applicability of model 2 requires island growth of the Volmer-Weber type (cf. section 2.4.3) of HBC on

	flat lying (proportion A)	inclined (proportion B)
6 Å	60 %	40 %
30 Å	43 %	57 %

Table 5.1: Ratio of flat lying to inclined molecules derived from the area of the NEXAFS feature at 285.3 eV in Figure 5.13 according to equation (5.1).

Ag(111), i.e. multilayer formation with inclined molecules setting in before the flat lying monolayer is completed. Consequently, increasing the coverage from 6 Å to 30 Å results in continued growth of the flat lying monolayer and inclined molecules in the multilayer, explaining the still substantial contribution of molecules in the monolayer to the overall spectrum at 30 Å coverage. In fact, this is fully consistent with UPS results presented further below. If layer-by-layer growth (Frank-van der Merve, cf. section 2.4.3) were the case, the attenuation of the monolayer component would be stronger than derived above.

Direct support for the validity of model 2 was obtained by STM and AFM investigations. For the monolayer regime, STM was used to directly determine the local structure of HBC on Ag(111). At the assumed ca. monolayer coverage (nominal mass thickness 4 Å), HBC spontaneously formed ordered structures on the 10 nm scale, as shown in Figure 5.17b. Here the local ordering of molecules is clearly visible. However, already in this image several defects are apparent. On a larger scale (e.g. Figure 5.17a) a high density of structural defects was observed. These defects were usually accompanied by structural instabilities, which sometimes caused complete changes between subsequent images. Either the tip modifies the surface structure due to interaction forces between tip and molecules or molecules are picked up, which often prevents from deriving molecular resolution anymore. Of course similar behavior was also found for other molecule-substrate combinations, but while it was usually the exception in other material systems, it was the rule for the ca. monolayer deposition of HBC on Ag(111). This indicates a rather weak bonding between HBC and the metal surface. Nevertheless, the obtained high-resolution images suggest the packing of individual HBC molecules in a short-range ordered structure with 6-fold symmetry and with lattice constants of $a = b = (1.36 \pm 0.06)$ nm and 2D unit cell angle of $\alpha = (60 \pm 2)°$, similar to that observed on other substrates (e.g. HOPG [104] and Au(111) [105]). Hence, flat lying molecules in the monolayer could be verified.

Of course, the multilayer could not be imaged by STM anymore, but AFM was used to directly gain information about the structure. There a

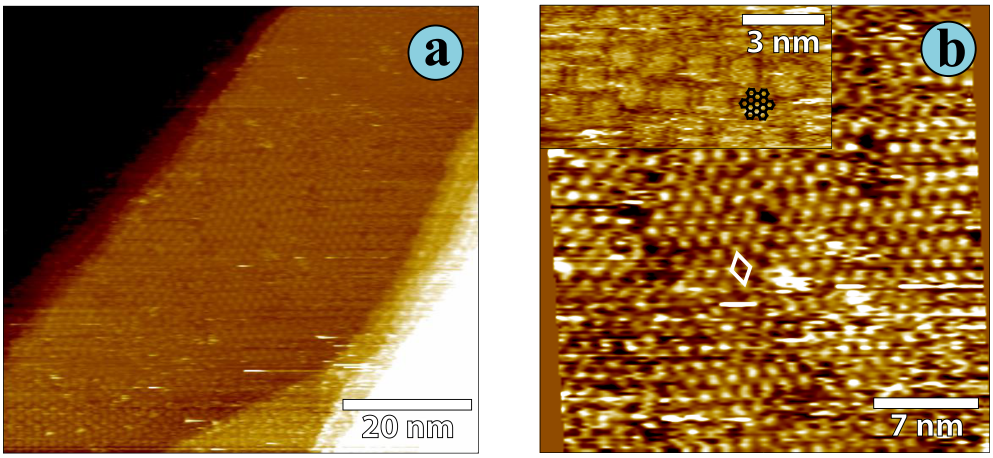

Figure 5.17: STM images of ca. monolayer HBC on Ag(111). (a) Long range scan revealing several steps of the Ag crystal covered by HBC molecules. (b) Magnification showing clearly visible short range order. The unit cell is marked by the white box. The inset presents a higher resolution image with one HBC molecule indicated. Tunneling parameters were $U_t = -1.2\,\mathrm{V}$ and $I_t = 0.4\,\mathrm{nA}$ for all images.

mass thickness of 30 Å HBC on Ag(111) was chosen. A representative AFM image of the structure found at this coverage is shown in Figure 5.18a. In this image islands of large flat terraces with well-defined step edges are observed. Apparently, island growth in the multilayer can already be confirmed. In order to derive the height of individual steps visible in the image the height-distribution histogram was evaluated shown in Figure 5.18b. Interestingly, the step heights were found to be integer multiples of $(8.5 \pm 0.6)\,\text{Å}$ (some of them marked in Figure 5.18b), which agrees perfectly with the expected height of lying HBC columns consisting of 43° tilted molecules in model 2 (i.e., 8.5 Å as indicated in Figure 5.16b). Note, that some of the peaks in the histogram (Figure 5.18b) can not be assigned to the steps in the AFM image (Figure 5.18a) and do not fit to multiples of the average step height. These peaks are mostly artifacts, e.g. caused by areas where the tip was not able to fully follow the contour of the structure. For example the dark appearing areas between most of the large flat terraces are just too small to allow the tip to fully penetrate into them, thus leading to a measured surface height which does not match the real one. Nevertheless, from the obtained AFM data the proposed multilayer growth in the bulk structure as described in model 2 as well as the island growth needed in this model can be fully confirmed.

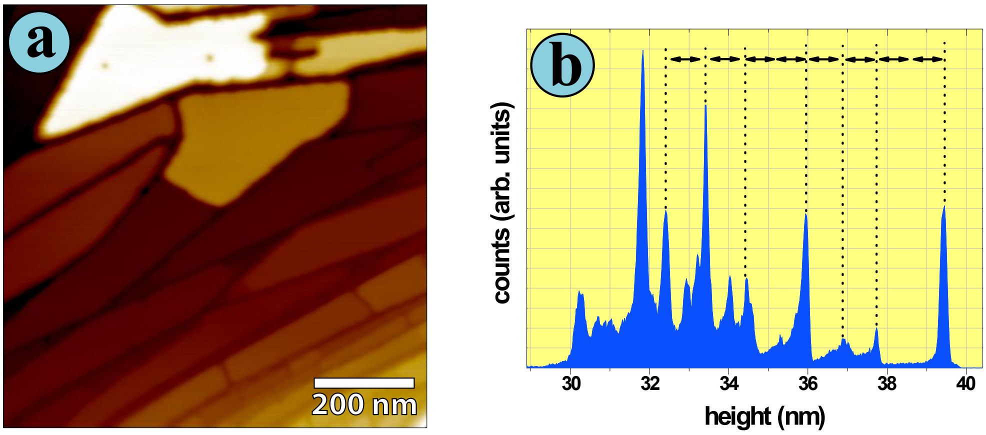

Figure 5.18: (a) AFM image (noncontact mode) of multilayer (30 Å) HBC on Ag(111) revealing several islands. (b) Height distribution histogram according to the AFM image in (a). Step heights are integer multiples of the HBC column width as shown in Figure 5.16b for model 2.

5.2.3 Electronic structure

The electronic structure was investigated by UPS. For this, starting with 2 Å HBC nominal coverage (θ) on Ag(111), the mass thickness was doubled after each deposition step up to a final mass thickness of 32 Å as presented in Figure 5.19a. The valence region spectra for $\theta = 2$ Å and 4 Å agree well with the simulated spectrum (bottom) of a single HBC molecule in the gas phase, derived by Gaussian broadening of molecular eigenstates obtained by semiemprirical AM1 calculations [51], after appropriate adjustment of the energy scale. Since a single molecule in the gas phase is not interacting at all, the agreement with experimental monolayer spectra is an additional indication for a relatively weak bonding of HBC on Ag(111), which is in agreement with the previous STM observations. The photoemission feature at lowest binding energy, centered at 2 eV, is derived from the two degenerate highest occupied π levels of HBC, and the feature at 2.5 eV corresponds to the next deeper lying π level. With increasing coverage θ, an additional peak appears at yet higher binding energy (2.8 eV, marked by an arrow in Figure 5.19a), whereas the intensity of the peak closest to the Fermi level (E_F) decreases, and the spectrum broadens overall.

A close look at the intensity of the Ag Fermi edge reveals that it is still nonzero at 32 Å HBC mass thickness, indicating an incomplete coverage of the Ag surface with molecules [106, 107]. Consequently, island growth for HBC/Ag(111) as postulated in model 2 above is confirmed. The transition

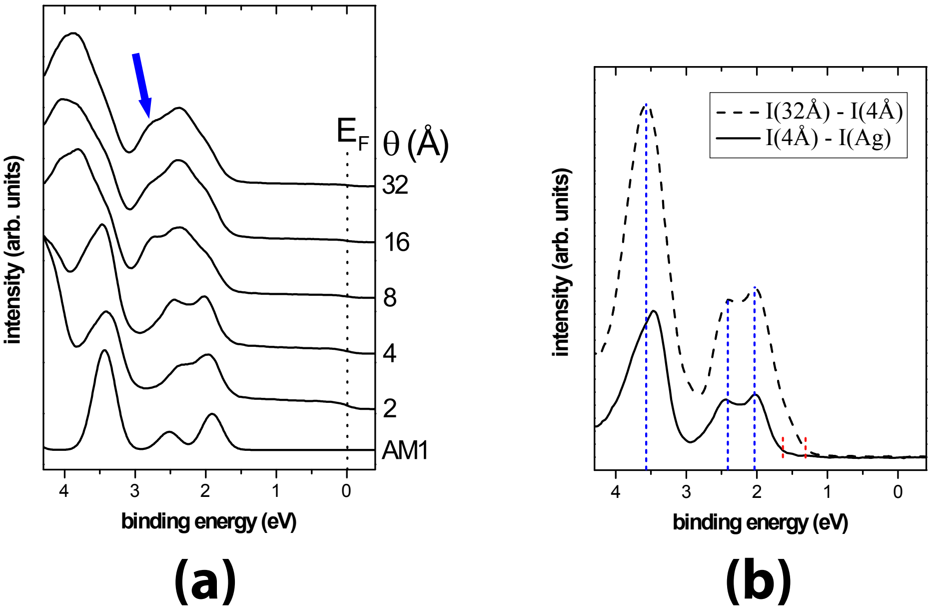

Figure 5.19: UPS spectra of HBC on Ag(111). (a) Spectra for increasing HBC coverage θ. The bottom spectrum (AM1) is a simulated UPS spectrum of a single molecule. (b) UPS spectra of the 'clean' monolayer (bottom solid line) and the 'clean' multilayer (top dashed line) HBC obtained by the subtraction procedure explained in the text. For easier comparison the multilayer spectrum was shifted by 0.3 eV toward lower binding energy to align the maxima of the highest occupied molecular levels (highlighted by blue dotted lines). The two red dotted lines at low-binding energy specify the onset of the HOMO-derived photoemission features, and thus indicate the level-broadening due to band formation.

from a valence spectral shape resembling single HBC molecules to a more complex shape occurs between 4 Å and 8 Å mass thickness. Fully consistent with growth model 2, in addition to flat lying HBC in the monolayer, vertically inclined HBC molecules are present for $\theta > 4$ Å. Thus, HBC molecules in the multilayer presumably give rise to the complex shape of UPS spectra for HBC $\theta \geq 8$ Å.

In order to verify that the photoemission spectra for high coverage are indeed a superposition of mono- and multilayer intrinsic HBC spectra, the following procedure was applied. First, all spectra were normalized to their intensity at the Fermi edge. Subsequently, the scaled pristine Ag(111) spectrum (not shown) was subtracted from the 4 Å HBC/Ag(111) spectrum in order to derive the 'clean' photoemission signal from the organic monolayer alone (displayed as bottom solid curve in Figure 5.19b). In order to remove metal substrate and HBC monolayer contributions from the 32 Å HBC/Ag(111) spectrum, the scaled 4 Å HBC/Ag(111) spectrum was subtracted. By this procedure the peak closest to the Fermi edge in the 32 Å spectrum completely vanishes. For better comparison, this 'clean' multilayer spectrum was shifted by 0.3 eV towards lower binding energy in order to align the lowest binding energy features (top dashed curve in Figure 5.19b). The comparison of 'clean' HBC mono- (solid line) and multilayer (dashed line) spectra in Figure 5.19b evidence that the multilayer spectrum is very similar to the monolayer spectrum (indicated by the blue dotted lines), except for the 0.3 eV shift in binding energy which was applied. The origin of this energy shift of the multilayer compared to the monolayer can be explained by changes of the polarization energy, i.e., weaker photohole screening due to a larger distance from the metal surface [108]. In addition, the 'clean' multilayer spectrum exhibits significant broadening of the feature derived from the HBC highest occupied levels toward lower binding energy (onsets are marked by red dotted lines in Figure 5.19b). By the subtraction procedure only the contribution of the monolayer is excluded from the 32 Å spectrum. Of course, contributions of layers between the first one and the layer of the highest deposition are still included. Since the screening efficiency will decrease with increasing film thickness, also different energetic shifts due to the photohole screening are expected for the different layers. Consequently, the broadening may be the consequence of the superposition of several different multilayer thicknesses with different screening efficiencies. Because the broadening is relatively strong with ca. 0.35 eV, another explanation might apply. As already mentioned in the introduction of this section, HBC molecules possess a defined stacking of their molecular π systems in the bulk structure. All previous results indicate that this structure is achieved in the multilayer of HBC on Ag(111) investigated in this work. Hence, the broadening of the highest occupied HBC levels in the multilayer may arise from one-dimensional electron band formation along the columnar stacking axis due to substantial intermolecular coupling [109] of neighboring HBC molecules in this structure.

5.2.4 Conclusions

The structural and electronic properties at the interface formed between hexa-*peri*-hexabenzocoronene and Ag(111) was investigated by NEXAFS, STM, AFM, and UPS. The following consistent picture of the interface was derived: The monolayer of HBC adsorbs flat lying on the metal surface and the molecular electronic structure resembles that of individual molecules due to weak molecule/metal interaction. The multilayer HBC grows in its bulk crystal structure on the monolayer HBC/Ag(111) template with an angle of 43° between the molecular planes and the substrate surface. This defined mono- to multilayer structural transition is accompanied by a 0.3 eV shift of the molecular levels towards higher binding energy. The formation of dispersing intermolecular electron bands in the crystalline multilayer is indicated by a broadening of the highest occupied HBC levels by ca. 0.35 eV compared to the monolayer, where no significant $\pi-\pi$ intermolecular overlap occurs.

Consequently, the fast attenuation of the substrate influence on the formation of molecular layers with increasing distance from the surface has been successfully demonstrated. Furthermore, the arrangement found in the multilayer exhibits promising electronic characteristics, which are of interest for using this material combination as the active layer in organic devices.

5.3 Surface reaction of polyacenes

Up to now molecular systems were presented, which possess only weak interaction with the metal substrate. In this section it should be demonstrated, how modifications of a molecule can initiate strong chemical interaction with the substrate. For this purpose the simple stick-like molecule pentacene (PEN) was chosen. The chemical structure of PEN is presented in Figure 5.20a. It simply consists of five linearly fused benzene rings. This molecule will be compared to a modified version in which all hydrogen atoms have been substituted by fluorine, leading to perfluoropentacene (PFP) shown in Figure 5.20b. Additionally, as substrate material Cu(111) was chosen, which has a lower standard electrode potential than Au(111) and Ag(111) and thus exhibits higher reactivity. If strong interaction with the substrate occurs, it will effect structural as well as electronic properties of the

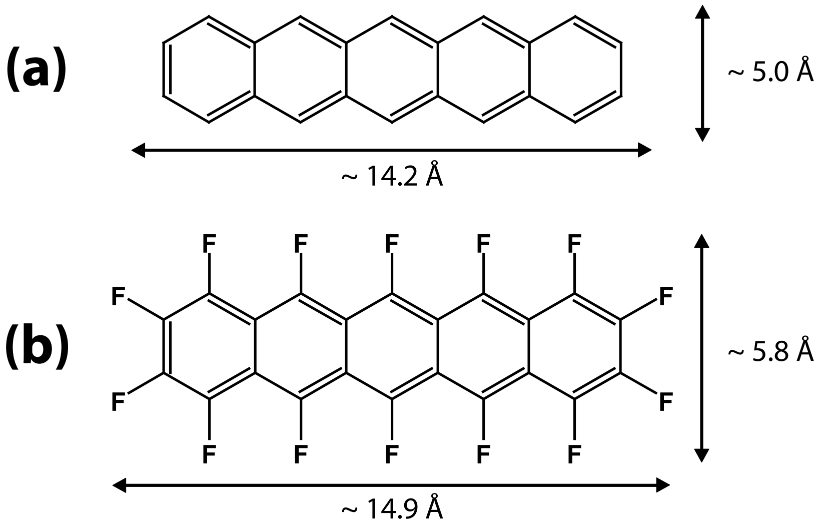

Figure 5.20: Chemical structure of (a) pentacene (PEN, $C_{22}H_{14}$) and (b) perfluoropentacene (PFP, $C_{22}F_{14}$). Numbers of the molecular size include the hydrogens, which are not painted.

molecules. Accordingly, STM was used for determination of the molecular ordering and photoelectron spectroscopy to gain information about electronic characteristics.

The use of PEN and PFP is further motivated by its potential application in organic electronics. Especially in the field of organic thin film field-effect transistors (OTFT / OFET) the charge carrier mobility plays a crucial role. In this context PEN has been widely studied as active layer material and shown to provide high hole mobilities of up to $5.5\,\mathrm{cm^2V^{-1}s^{-1}}$ in OTFTs [110]. Admittedly, as electron carrier PEN shows only poor mobility of $0.04\,\mathrm{cm^2V^{-1}s^{-1}}$ [111]. Alternatively, the use of PFP was investigated and relatively high electron mobilities of more than $0.2\,\mathrm{cm^2V^{-1}s^{-1}}$ [112] were found. For PEN many reports concerning electronic and structural characteristics on different materials are available, i.e. on Au(111) [113], Au(100) [100], Cu(119) [114], Cu(110) [115], Cu(111) [116] and Ag(111) [78]. Investigations of PFP on metal substrates focused mainly on their electronic properties so far, i.e. in combination with Au(111) [117] and Cu(111) [118]. Therefore, further investigations are valuable for the development and use of PFP as active material in organic electronics.

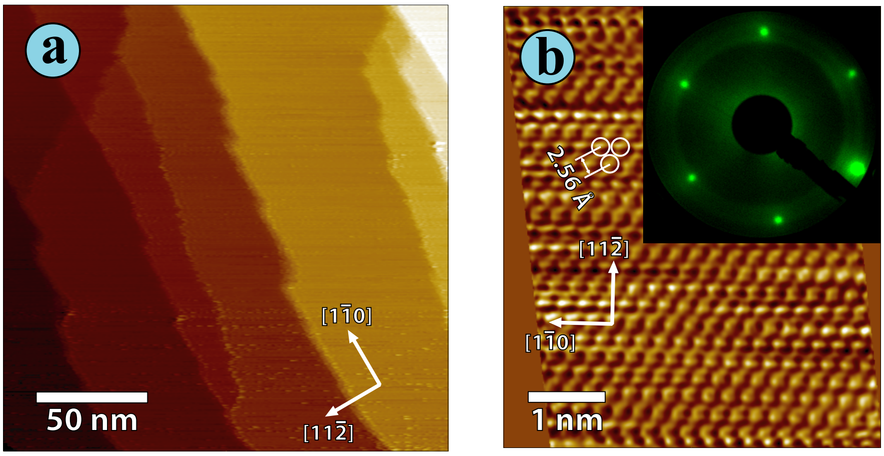

Figure 5.21: STM-images of Cu(111). (a) Step edges of the crystal surface. ($U_t = -0.1\,\mathrm{V}$, $I_t = 0.8\,\mathrm{nA}$) (b) High resolution image revealing the atomic lattice of the surface. An additional low pass Fourier filter was applied. ($U_t = -0.4\,\mathrm{V}$, $I_t = 1.2\,\mathrm{nA}$) In the inset the corresponding LEED image taken at 140.0 eV electron energy is shown.

5.3.1 Cu(111)

Also the copper single crystal fits into the series of the preceding two metals, i.e., Au(111) and Ag(111). Again, the crystal exhibits fcc packing, but in this case with significantly reduced lattice constant of $a_{Cu} = 3.62\,\text{Å}$. Due to the same crystal packing the (111) surface exhibits again hexagonal atomic symmetry with lattice constant of $a_{Cu}/\sqrt{2} = 2.56\,\text{Å}$. A high resolution STM image of the surface is shown in Figure 5.21b, where the inset represents the corresponding LEED pattern. The step height between two atomic layers in (111)-direction is $a_{Cu}/\sqrt{3} = 2.09\,\text{Å}$. For crystals used in the experiments a typical terrace width of about 100 nm was found (Figure 5.21a). Cu(111), just like Ag(111), features no observable surface reconstruction. The work function of Cu(111) is 4.9 eV [97].

5.3.2 PEN/Cu(111)

In a first experiment the thin film growth of pentacene (PEN) on Cu(111) was investigated by STM, in order to compare the results with the data of perfluoropentacene (PFP) presented in the next section (section 5.3.3). Although, strong organic/metal chemisorption was suggested by previously obtained XPS data [118], no molecules within the sub-monolayer regime were

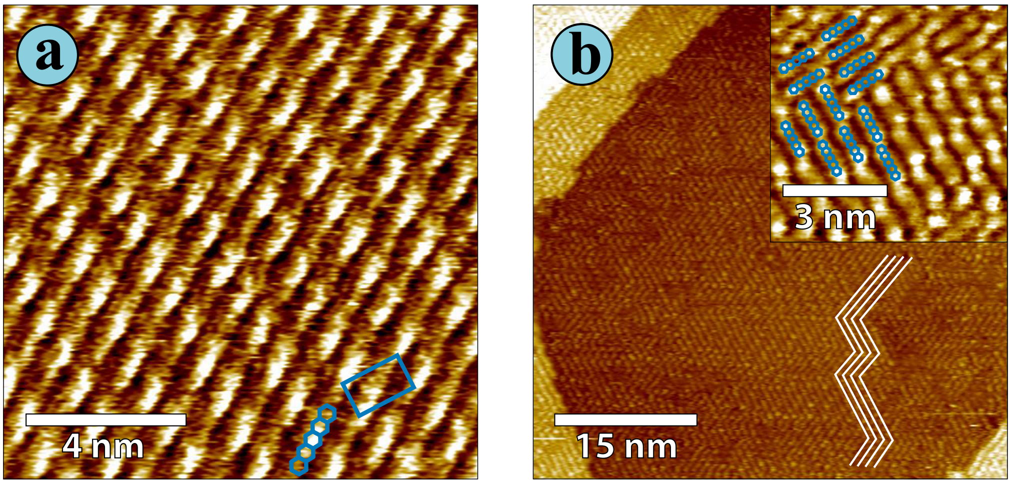

Figure 5.22: Monolayer deposition of pentacene on Cu(111). (a) STM image of the close packed molecular layer. Single PEN molecules can be clearly identified (for clarification one molecule is overlaid by its chemical structure at bottom). The blue box marks the unit cell according to the LEED data in Figure 5.23. ($U_t = -1.0\,\mathrm{V}$, $I_t = 0.6\,\mathrm{nA}$) Some horizontal noise was removed by additional Fourier filtering. (b) Zig-zag structure of PEN molecules. The white lines exemplary highlight the molecular orientation. In the inset a magnification is shown, where single molecules are clearly visible. To clarify the relative positions, some molecules were overlaid by their chemical structures. ($U_t = -1.2\,\mathrm{V}$, $I_t = 0.3\,\mathrm{nA}$)

observed by STM. Again, most probably at low coverage molecules stay in a two dimensional molecular gas phase and are therefore highly mobile on the surface. Note, that the observation of individual molecules on Cu(111) at sub-monolayer coverage was reported for low temperatures [116]. After increasing the nominal amount of molecules deposited onto the surface, a closed monolayer of PEN could be observed by STM (Figure 5.22). Two different domains comprising ordered molecules were found. Within the first kind of domain, shown in Figure 5.22a, molecules align close packed in a regular array forming rows perpendicular to their long axis. The unit cell (marked by the blue box in Figure 5.22a) was determined from LEED analysis to be $a = (1.6 \pm 0.1)\,\mathrm{nm}$, $b = (0.9 \pm 0.1)\,\mathrm{nm}$ and $\alpha = (89 \pm 1)^\circ$ (LEED images of this sample will be discussed further below). This kind of structure extended over large areas of the surface retaining the same orientation of molecules. Within the scanned area no domain boundaries were observed, even though, according to the substrate symmetry, different orientations of molecular rows are expected. Nevertheless, a different type of domain was often found, also comprising ordered molecules as shown in Figure 5.22b. In this structure molecules arrange in principle in about the same packing as already determined in Figure 5.22a, but repeatedly change their orientation, forming a zigzag structure. Every 2 nm - 5 nm in the direction of progression of this zigzag structure a kink of about 120° occurs. The progression is highlighted by white lines shown in Figure 5.22b. In the inset a magnification is presented, in which single molecules can be identified. For clarification they are partly overlaid by their chemical structures to highlight their positions relative to each other. Apparently, molecules appear as rods having a bright lobe at its two ends, referring to an enhanced tunneling conductance at the end parts of PEN as already described by Lagoute *et al.* [116]. According to the STM observations, this kind of ordering was the dominating one.

LEED images taken of this sample are presented in Figure 5.23a for two different electron energies. Because it was not possible to achieve all spots with acceptable contrast in one image alone, a reconstruction of the important LEED spots is presented on the right of Figure 5.23a. There, the color of the spots refers to the appropriate spots marked exemplary by open circles on the left. At first glance the LEED pattern is similar to what is expected from a hexagonal lattice, which would be in contrast to the STM observations. Although, they were not observed at the same time in STM, according to the substrate symmetry three different orientations of the rectangular lattice can occur. In Figure 5.23b the according three reciprocal lattices are shown on the left. Every cross point of such lattice marks the position of one LEED spot. The superposition of these three lattices leads to the construction shown on the right in Figure 5.23b. Interestingly, the resulting spots form a hexagonal pattern. Moreover, some of the spots are a superposition of all three reciprocal lattices (marked by surrounding dashed black circles in Figure 5.23b). Taking a closer look at the experimental LEED images again (Figure 5.23a) reveals, that at exactly these positions spots with brighter appearance are found. Therefore, the existence of a rectangular lattice can be confirmed from LEED analysis in full agreement with the STM observations. Lattice parameters derived from these images were already presented further up.

5.3.3 PFP/Cu(111)

Now, the behavior of perfluoropentacene (PFP) on Cu(111) should be investigated. Following the same systematic, first a molecular deposition of PFP in the sub-monolayer regime was used. Also here no laterally ordered structures or big clusters were observed. But in this case, single molecules and small clusters were found, which aggregated at step edges and presumably

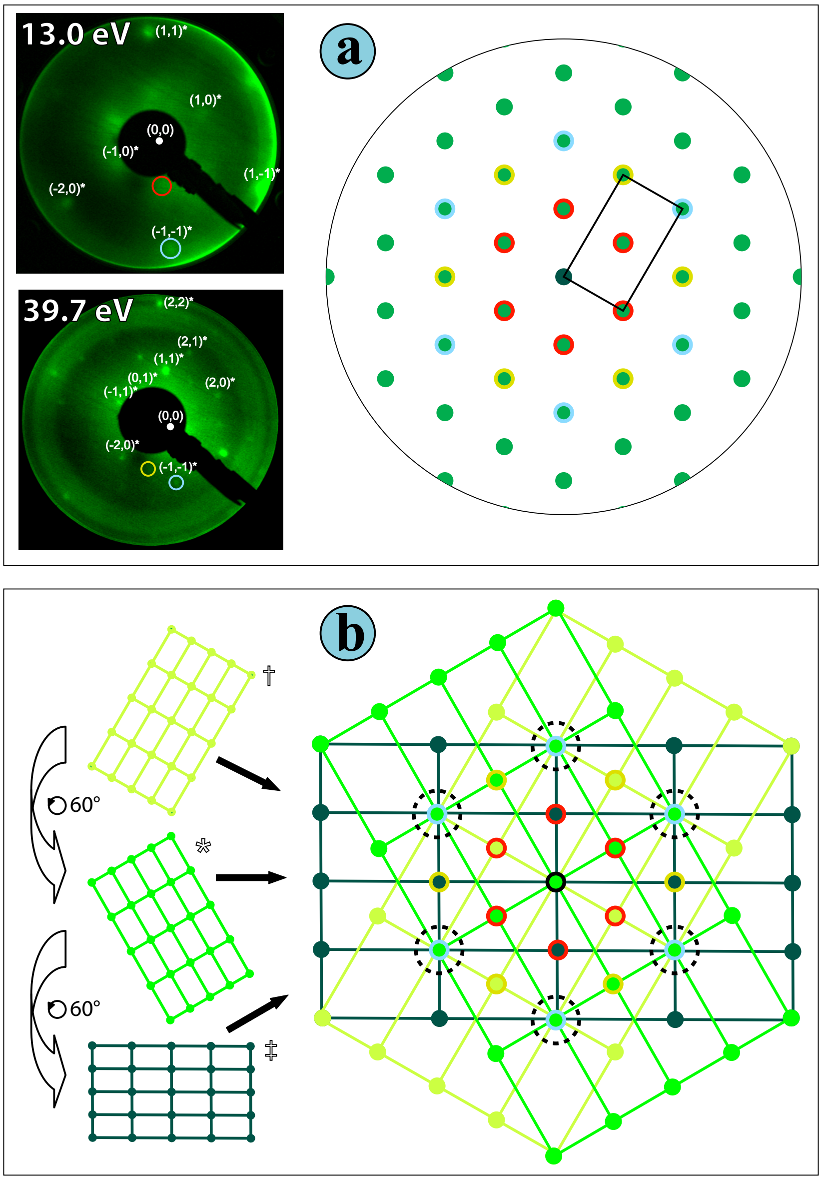

Figure 5.23: (a) LEED images of monolayer pentacene on Cu(111) taken at two different electron energies. On the right relevant spots are plotted into one schematic image. Spot colors refer to the spots marked by open circles on the left. The reciprocal unit cell is marked by the black box. Some of the spots are labeled according to the lattice marked by an asterisk in (b). (b) According construction of the LEED pattern by three rectangular lattices differing by 60° rotations is shown. Spots which are generated by a superposition of all three lattices are marked by the surrounding dashed black circles.

point defects within terraces (Figure 5.24a). Some of these molecules are marked by white arrows in Figure 5.24a. Apparently, step edges are covered nearly completely with molecules while most area of the terraces appears to be featureless. In the inset a magnification is shown, where single molecules can be clearly identified as rod-like features with seemingly random orientation. Since the amount of observed molecules does not match the nominal amount of molecules deposited onto the surface, it is suggested here as well, that the majority of molecules still stays in a gas like phase and diffuses across the surface. Because these molecules are highly mobile on the surface, they can only contribute to the overall background of the tunneling current and are invisible in STM. Point defects as well as steps provide preferred stabilization sites, where molecules tend to react with the copper surface and are stabilized at these points. Once a molecule passes a defect, it will stick to it with a certain probability. Therefore, increasing the mobility of the molecules increases the probability of a molecule to find a defect site and consequently to nucleate at this point. A simple method to increase the mobility of molecules is to raise their thermal energy. This is achieved by heating the sample. The challenge is to maximize the mobility of molecules whilst limiting the temperature to ensure the molecules will not be destroyed or desorbed from the surface. In this work a constant annealing temperature of only 150 °C was chosen and in return the time of annealing was varied. In a first step the sample was annealed for about 45 min. An exemplary image of the resulting surface structure is shown in Figure 5.24b. Obviously, the density of nucleation sites has been increased, which is apparent by a higher density of populated point defects and an expanded size of previously existing clusters. In the inset a magnification is presented, where also some local ordering becomes visible as some molecules appear as small parallel lying sticks. Overall, most of the surface area is still free of molecules and no long range order is observed. Therefore, the sample was annealed again at 150 °C for additional 90 min, summing up to 135 min in total. An STM image of the surface thereafter is shown in Figure 5.24c. Now, the majority of surface area is covered by molecules which interconnect the previously separated nucleation sites. As the inset depicts, most of the molecules still remain disordered. Also, no long range order could be observed. Still, the molecular layer is not completely closed, as many holes are visible, which presumably reveal the underlying substrate. Nevertheless, some molecules are already growing on top of the first layer. In Figure 5.24c these molecules appear as white spots and the white line in the lower right part of the image. Interestingly, within the bright line molecules were found to arrange in a row with side by side arrangement perpendicular to their long axis. Apparently, the unordered first layer can serve as template for further growth. However,

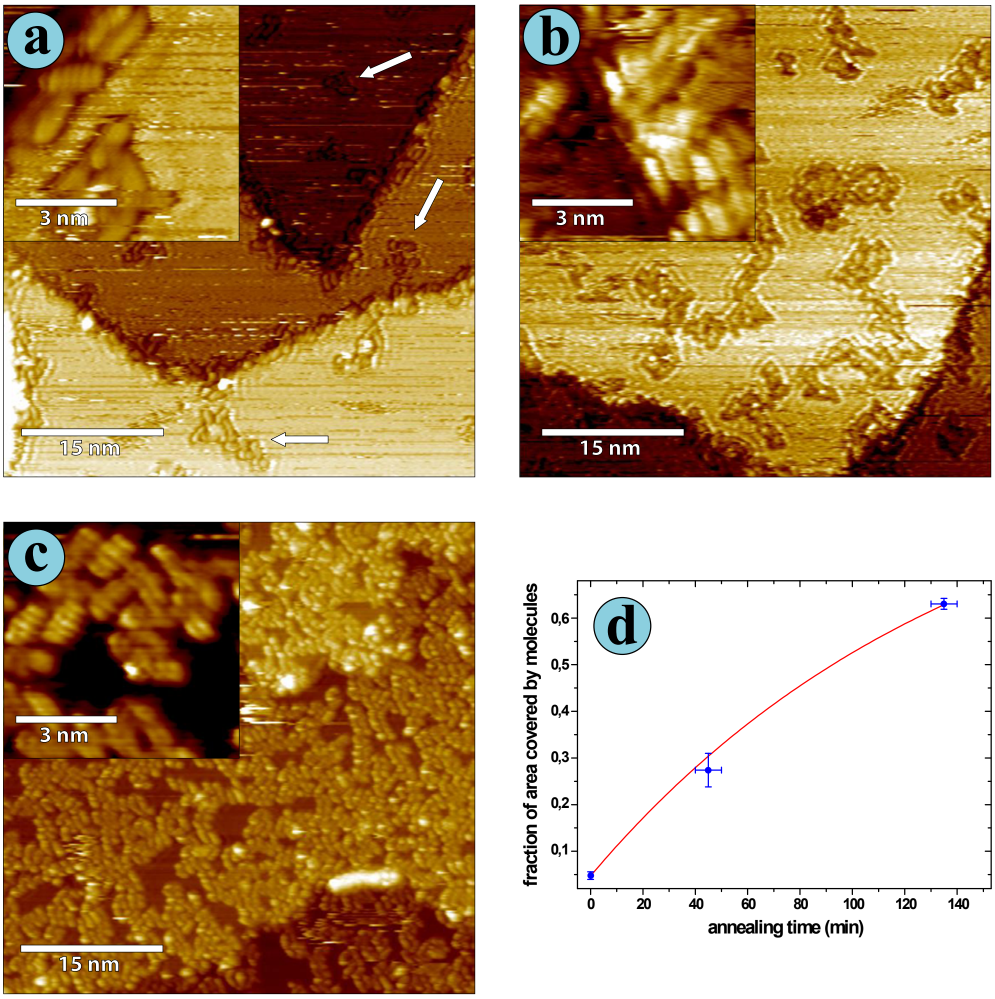

Figure 5.24: STM images of sub-monolayer perfluoropentacene on Cu(111). The insets show the according magnifications where single molecules can be identified. (a) Appearance after deposition of PFP. Some of the molecules sticking to the step edges and point defects at terraces are marked by arrows. ($U_t = -1.2\,\mathrm{V}$, $I_t = 0.5\,\mathrm{nA}$) (b) Surface after annealing at 150 °C for 45 min. ($U_t = -1.4\,\mathrm{V}$, $I_t = 0.3\,\mathrm{nA}$) (c) Molecular layer after annealing at 150 °C for 135 min in total. ($U_t = -1.2\,\mathrm{V}$, $I_t = 0.3\,\mathrm{nA}$) (d) Fraction of surface area, which is covered by stabilized molecules, in dependence of the annealing time. The red line is derived from adaption to first order reaction rate law (for details see text).

this was not further investigated due to the poor electronic characteristics already observed for the annealed first layer, presented further below.

Nevertheless, based on the STM observations of the annealing dependent structures, information about the energy gain upon stabilization of a molecule should be derived. Obviously, the fraction of surface area which is covered by stabilized molecules is increasing with the annealing time. Consequently, as first step the area fraction of stabilized molecules was determined for several images and the results were averaged according to the three different annealing stages, i.e. not annealed, annealed for 45 min and annealed for 135 min. Appropriate area fractions versus annealing time are plotted in Figure 5.24d. Stabilization of molecules at the surface can be considered as a reaction which follows the laws of chemical kinetics. In this case molecules on the surface which have not yet been stabilized should be regarded as the reactants. In general, the more molecules are diffusing across the surface, the higher the probability a stabilization site at the surface will be occupied. Therefore, the reaction rate is expected to depend on the concentration of the reactant and first order-order rate law has to be applied. If the concentration of the reactant is called R the reaction rate follows:

$$R = R_0 e^{-kt} \tag{5.2}$$

with starting concentration R_0, reaction rate coefficient k and time t. Because the concentration of the reactant can not be calculated with acceptable precision from the monitored deposition rate and deposition time, a different approach has to be taken. Basically, the observations in STM provide information about reacted molecules, rather than the reactants. In order to handle this information it will be assumed, in the case that all available molecules have been stabilized at the surface the coverage would be 1 (according to 100%). Consequently, the concentration of reacted molecules P can be calculated by $P = 1 - R$ and is equal to the fraction of area covered by stabilized molecules. Then the reaction rate modifies as follows:

$$P = 1 - (1 - P_0)e^{-kt} \tag{5.3}$$

with starting concentration of reacted molecules P_0. Based on this formula the data points in Figure 5.24d can be fitted (red line in Figure 5.24d). The interesting fit parameter is the reaction rate coefficient, which is determined to be $k = 1.2 \times 10^{-4}\,\mathrm{s}^{-1}$. Furthermore, the reaction rate coefficient k depends on the reaction temperature T and is theoretically given by:

$$k = A \exp\left(-\frac{E_A}{k_B T}\right) \tag{5.4}$$

which introduces the pre-exponential factor A, activation energy E_A and Boltzmann constant k_B. This formula is similar to what was found to be the desorption rate in thermal desorption spectroscopy (TDS) [119]. In comparison, the activation energy for the reaction can be identified with the activation energy for desorption, which is assumed to be equal to the binding energy of molecules on the surface [120]. Since the data presented in this work is taken at only one temperature, two unknown parameters remain, i.e. A and E_A. Unfortunately, no according data was published for PFP, yet. Nevertheless, because the aim of these considerations is to get a feeling of the involved energies, alternatively, available data from experiments with PEN should be used. Therefore, the pre-exponential factor of $A = 1.0 \times 10^{13}\,\mathrm{s}^{-1}$ given in the work of Söhnchen *et al.* [120], used for determination of TDS spectra of a completed monolayer, should be adequate for this calculation. Then the activation energy is calculated to be $E_A = 1.4\,\mathrm{eV}$. Variation of the pre-exponential factor in the range of $A = (10^{12} \ldots 10^{14})\,\mathrm{s}^{-1}$ leads to variations of the activation energy in the range of $E_A = (1.3 \ldots 1.5)\,\mathrm{eV}$. Although, quite a number of assumption have been made in this calculation, it provides a rough estimation of the order of magnitude of the involved energies. The height of the resulting energy proves that molecules undergo chemisorption upon stabilization on the surface. Note, that the data points in Figure 5.24d can also be fitted by a linear regression with just slightly higher sum of square error, implying a zero-order reaction rate law. However, the calculated activation energy under this assumption turns out to be exactly the same in the end.

In order to derive a completed layer, a fresh sample with a priori higher nominal amount of molecules was prepared. STM images of the resulting structure are presented in Figure 5.25. At this deposition the molecular layer formed a highly ordered structure. Within this layer molecules arrange side by side with a small offset along their long axis and are forming rows perpendicular to it, which can be clearly seen in Figure 5.25. Three different orientations of these rows were observed that are differing by 60° rotations, according to the substrate symmetry. They are visible on the different steps in Figure 5.25a. In Figure 5.25b a magnification of molecules on one of the steps is shown. To clarify the alignment of PFP, the molecular structure is overlaid on one molecule. Obviously, the five benzene rings of PFP appear as five stick-like features perpendicular to the long axis of the molecule corresponding to the HOMO of PFP (the inner structure of PFP will be discussed in detail further below). The corresponding LEED image is shown in Figure 5.25c. As already shown for PEN on Cu(111), this pattern can be constructed from three lattices differing by 60° rotations in agreement with the STM observation in Figure 5.25a. The unit cell (shown as

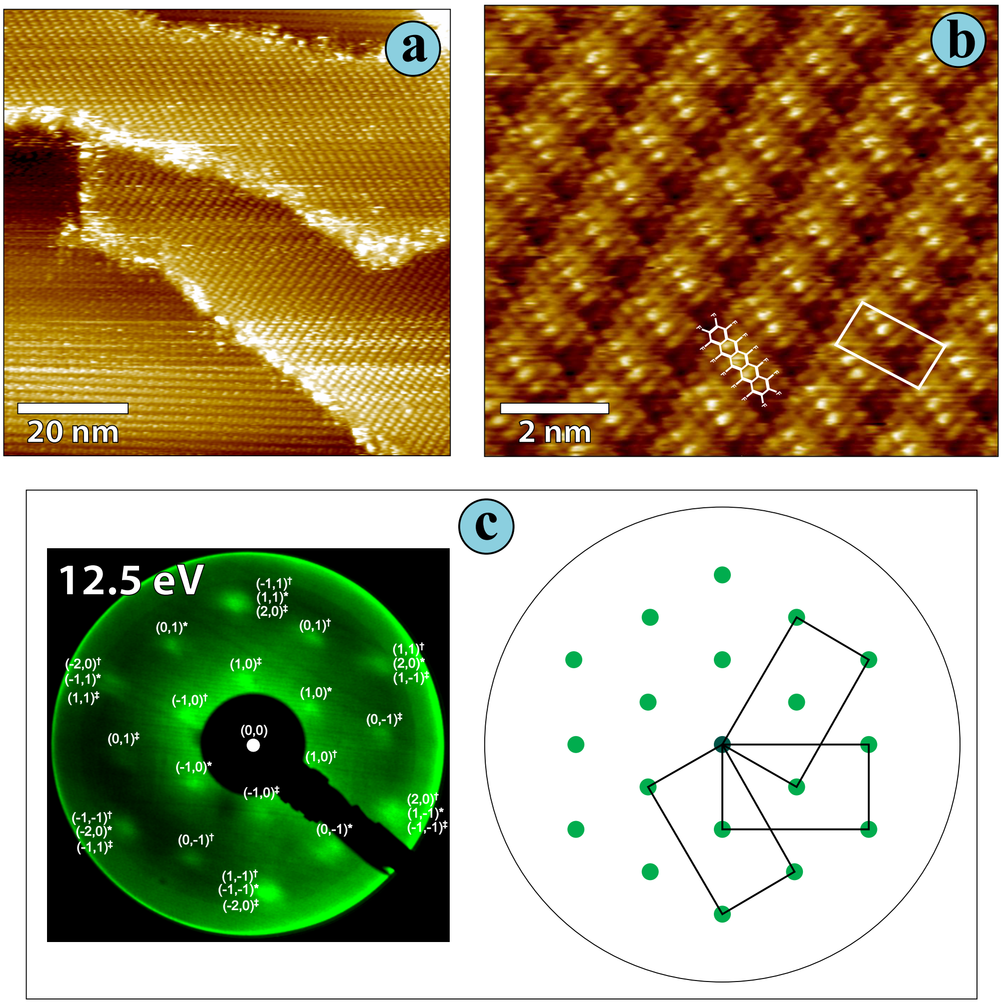

Figure 5.25: STM images of monolayer coverage PFP on Cu(111) revealing highly ordered molecular structures. (a) Wide range scan showing several substrate steps which are covered by molecules in three different orientations. ($U_t = -1.0\,\mathrm{V}$, $I_t = 0.3\,\mathrm{nA}$) Here, a plane correction procedure was chosen which maximized the contrast of molecules rather than showing the right height of steps. (b) Magnification of one domain. Molecules exhibit submolecular contrast. To clarify the position, one molecule is overlaid by its chemical structure. The white box marks the unit cell according to the LEED observation. ($U_t = -0.8\,\mathrm{V}$, $I_t = 0.5\,\mathrm{nA}$) (c) Appropriate LEED image. LEED spots are labeled according to the three different reciprocal lattices presented in Figure 5.23b. On the right a schematic of the spots is shown including the three reciprocal unit cells which differ by 60° rotations.

the white box in Figure 5.25b) was determined from the LEED image to be $a = (1.75 \pm 0.05)\,\mathrm{nm}$, $b = (1.0 \pm 0.1)\,\mathrm{nm}$ and $\alpha = (92 \pm 1)^{\circ}$. Compared to PEN the unit cell of PFP is slightly larger, which is expected by substitution of hydrogen atoms with fluorine. Apart from the larger unit cell, ordered structures of PEN and PFP are very similar to each other. However, domains with rapidly alternating orientations as found for PEN (Figure 5.22b), were not observed for PFP on Cu(111).

Actually, the temperature induced reaction of PFP on Cu(111) observed by STM (Figure 5.24) is also supported by the results of photoemission experiments. XPS spectra of the C1s and F1s core levels taken of samples with PFP monolayer deposition are presented in Figure 5.26. Here, the top curve shows the appropriate region recorded just after deposition of PFP and the bottom curve represents the same region after annealing at 150 °C. For the fresh sample three peaks appear in the C1s core level region (top curve of Figure 5.26a), which are well separated from each other. The two peaks at higher binding energy (287.3 eV and 285.8 eV) have a separation of 1.5 eV and can be attributed to chemically inequivalent carbon atoms within PFP, i.e. C atoms bound only to other C atoms and those which are connected to F on one side. Peak splitting because of strong chemical interaction with the substrate can be ruled out, as the peaks are virtually identical to the ones found for PFP on Au(111), which has been shown to exhibit only weak interaction [117]. Surprisingly, an additional peak at around 284.5 eV binding energy is observed, which is much smaller than the other two. This one can be assigned to residual carbon contamination originating from the PFP sublimation and sample handling on the one hand, but also to PFP molecules which have reacted with the substrate surface on the other hand. Interestingly, after annealing the sample at 150 °C the ratio of peak intensities completely changes as shown in the bottom curve of Figure 5.26a. Now, the additional peak at lower binding energy has much more intensity than the others. This is fully consistent with the STM observation that upon annealing more PFP molecules have reacted at defect sites of the Cu(111) surface. Additionally, a shoulder at even lower binding energy appears, indicating the existence of a fourth peak with a separation of 1.0 eV from the neighboring one. Taking a closer look at the peak positions reveals the binding energies have also changed compared to the fresh sample. The two peaks at higher binding energy are found at 287.25 eV and 285.9 eV, whereas the two peaks at lower binding energy are located at 284.4 eV and 283.4 eV, respectively. This change in binding energy is demonstrated in Figure 5.26a and b, which show the same experimental data, by Gaussian fits additionally painted into the spectra of the C1s region. Fittings (solid lines) shown there were optimized for (a) the fresh sample (three peaks) and (b) the annealed spectrum

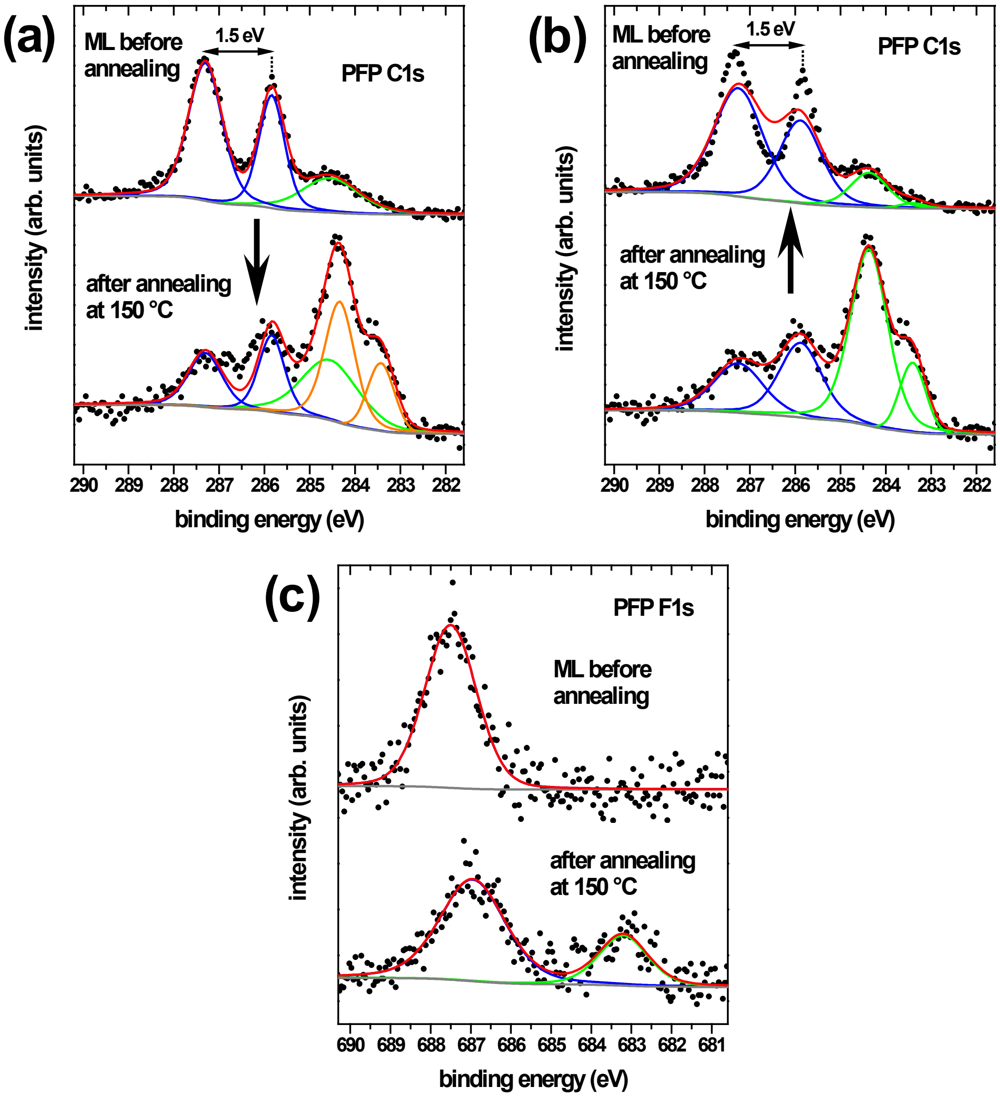

Figure 5.26: XPS spectra of monolayer PFP on Cu(111) (corresponding to nominal mass thickness of 4 Å) before (top curve) and after annealing (bottom curve) the sample at 150 °C. Black points represents measured data, while solid lines are derived from fitting the data with appropriate Gauss-functions. (a) and (b) show the C1s region, where the fitting was optimized for the spectrum of (a) the fresh sample and (b) the annealed one (the direction of this procedure is indicated by the arrows, for details see text). (c) F1s region.

(including four peaks accordingly). The same peaks were then taken to fit the respective other spectrum, i.e. the spectrum of the annealed sample in (a) and the spectrum of the fresh sample in (b). In the according second fit only the peak intensity was allowed to vary. In Figure 5.26a two additional peaks had to be added to the spectrum of the annealed sample to be even able to accomplish the fitting procedure. The resulting peaks do not suit the spectrum very well (bottom in Figure 5.26a) and the use of five peaks instead of four, which refers to the number of peaks in the experimental data, has no further physical motivation. Even more clearly, in Figure 5.26b the four peaks from the bottom spectrum were directly used to fit the top spectrum by only varying the peak intensity. Also there, the fitting can not be optimized to match with the measured data points. Apparently, in both cases the second fitting procedure does not provide reliable results as long as the peak positions are fixed to the values derived from the first fitting procedure. Furthermore, comparing the peaks in the spectrum of the annealed sample with the spectrum of the fresh sample reveals that the width and in particular the intensity ratio of the two peaks at higher binding energy have significantly changed. Consequently, peaks in the annealed spectrum originate from completely new carbon binding sites, suggesting there are at least four chemically different reaction products. Additional indication for this reaction is found in the spectra of the F1s core level presented in Figure 5.26c. Again, the top curve shows the spectrum taken at the fresh sample, whereas the bottom spectrum represents the annealed one. Best fits are painted as solid lines in the appropriate spectrum. For the fresh sample a single peak at 687.5 eV binding energy is found according to only one kind of chemical bond of fluorine within the molecule. This one can be attributed to F atoms covalent bound to C [121] as it is expected. After annealing, suddenly two peaks appear. The first peak is located at binding energy of 687.0 eV. Most probably this one refers again to F atoms bound to C, but in this case a chemical shift upon reaction with the copper surface occurs. Interestingly, the second peak appears well separated at 683.2 eV binding energy. This peak is assumed to originate from F atoms which have been broken off from the molecule upon annealing and directly reacted with the copper surface. Consequently, from XPS spectra considerable changes of the chemical structure at the PFP/Cu(111) interface after annealing were observed, which indicate strong chemical interaction of PFP with the substrate surface. More evidence for previous assumptions is found in UPS spectra discussed in the next section. Further annealing to higher temperatures, i.e. up to 250 °C, leads to total destruction of PFP evidenced by vanishing F1s core level while contributions to C1s remain.

Moreover, also in UPS spectra a significant annealing dependence is ob-

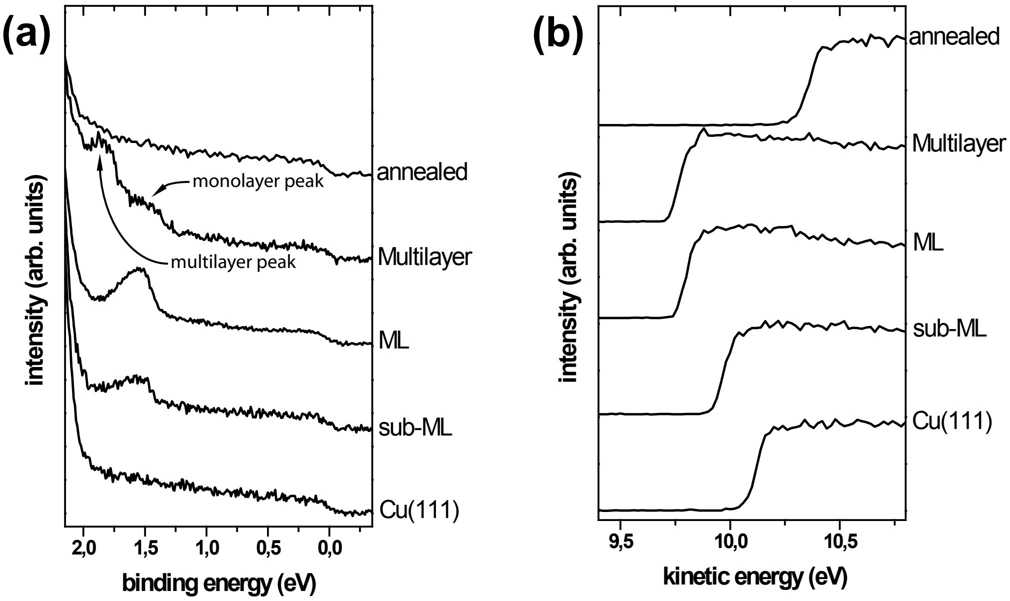

Figure 5.27: UPS spectra of PFP on Cu(111). From bottom to top, spectra of the clean Cu(111) substrate, sub-monolayer PFP (corresponding to nominal mass thickness of 1 Å), monolayer, multilayer (corresponding to 7 Å) and after annealing the sample at 150 °C are presented. (a) Valence band region. For better comparison all spectra have been normalized to their intensity at the Fermi-edge. (b) Appropriate SECO taken at -10 V sample bias.

served. The valence band of appropriate samples is presented in Figure 5.27a. Starting with the clean substrate (bottom) spectra of sub-monolayer, monolayer, multilayer and annealed sample (top) are shown. In the sub-monolayer up to the multilayer spectrum several peaks appear in the valence band, which refer to the HOMO of PFP and will be discussed in detail further below. At first the behavior upon annealing the sample at 150 °C should be analyzed. Surprisingly, the corresponding spectrum (top) appears to be completely featureless in the valence band, similar to what was observed for the clean Cu(111) crystal (bottom). As has been shown so far, the molecules react with the surface upon annealing the sample. Especially, core levels of C atoms showed evidence for strong reaction, indicated by a completely change of spectral features in XPS. In accordance with the UPS data it is now presumed, that all carbon atoms formerly involved in double bonds have taken a fourth binding partner, e.g. by binding to the copper surface. In this case the molecules are no longer aromatic as there is no free binding site to form a double bond. Since the double bonds provide the electrons, which render the molecule to have semiconducting characteristics, loss of conjugation is accompanied by vanishing valence band contributions. In case any intact conjugated molecule would still exist on the surface, it would lead to an observable state in the valence band. In Figure 5.27b the corresponding secondary electron cut-offs (SECO) are shown (following the same order). With increasing deposition of PFP the SECO shifts towards lower kinetic energy, indicating a decrease of work function. Interestingly, after annealing (top curve) the SECO shifts back, resulting in an even 0.2 eV higher work function than found for clean Cu(111). As already suggested from XPS spectra of the F1s core level, F atoms may have broken off from the molecule. In this case the strongly electronegative fluorine presumably reacts with the copper surface, leading to an increase of the surface dipole, which explains the increase of work function. In conjunction of STM, XPS and UPS data, it can be concluded that annealing the sample leads to strong reaction of PFP with the copper surface, which is accompanied by largely changes in the chemical and electronic structure of the molecules.

Taking a closer look at the valence band of PFP reveals another interesting feature (Figure 5.27a). Starting at sub-monolayer coverage the HOMO of PFP appears at an onset of about 1.40 eV and shows increasing intensity when the molecular amount increases to monolayer coverage. Surprisingly, further increasing the molecular amount on the surface to about 7 Å (labeled as multilayer in Figure 5.27) leads to decreasing intensity of the formerly identified HOMO, while at the same time a second peak with 0.34 eV higher binding energy appears. According to recent findings, the additional state may be attributed to PFP molecules in a different conformation [74, 122]. The fluorine in PFP carries a negative partial charge compared to the carbon backbone of the molecules. This leads to the formation of an in-plane dipole which points towards the molecular core [122]. As it was already found for dihexyl-sexithiophene on Ag(111), this effect results in an orientation dependent ionization energy [74]. As long as the molecules lie flat on the surface (as evidenced from STM measurements) the dipole has only small influence on escaping electrons generated by the photoemission experiment. In case the molecules are standing upwards, the binding energy appears to be significantly increased. Comparison of the observed shift for PFP on Cu(111) in these experiments (+0.34 eV) with results of PFP on SiO_x where the molecules are completely upright standing with their long molecular axis (+0.85 eV) [122], suggests that PFP in the experiments discussed here is either not completely upright standing or possibly standing upright with its short molecular axis. However, if a transition of lying to standing molecules occurs, the change in electrostatic potential affects not only the valance band. Consequently, taking a look onto the core level spectra of these samples is valuable. Appropriate spectra for mono- and multilayer are presented in

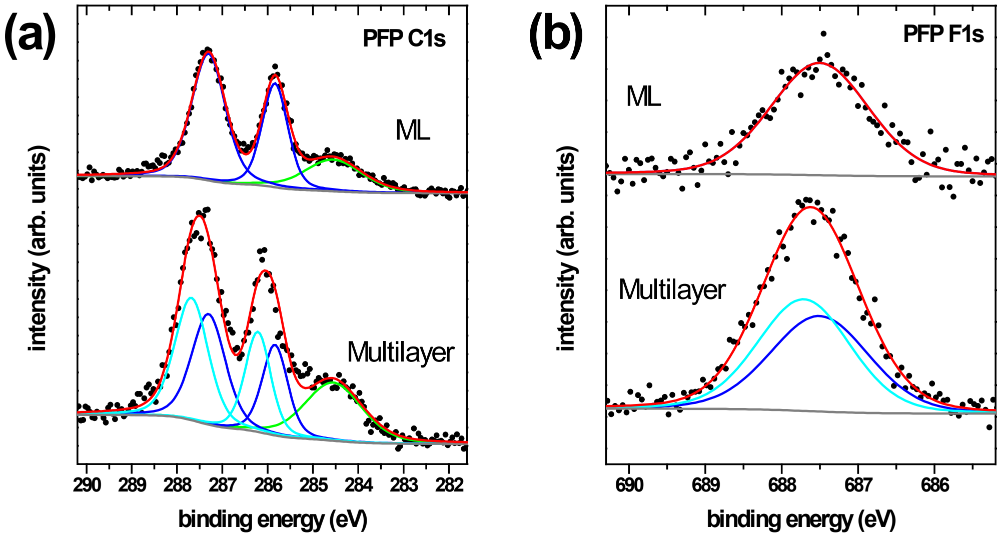

Figure 5.28: XPS spectra of monolayer (ML) and multilayer PFP on Cu(111). Appropriate fittings are included as solid lines. For details about the fitting procedure see text. (a) C1s core level. (b) F1s core level.

Figure 5.28. Indeed, small changes between spectra of these two depositions are observed. Starting with the C1s core level (Figure 5.28a), the monolayer can be fitted by three Gaussian functions, as discussed formerly. While the peak at lowest binding energy remains at the same position upon increasing film thickness, the other two peaks exhibit slight shifting towards higher binding energy. According to the previous assumptions the multilayer peaks (bottom) have to be a superposition of the monolayer states and the ones derived from standing molecules. Since the dipole only affects the energetic position of molecular levels, the states of standing molecules have to exhibit similar width and intensity ratio as it was found from fitting the monolayer spectrum. Thus, fitting of the multilayer spectrum was accomplished by two sets of Gaussian functions. The first set (dark blue), according to the spectral features of lying molecules, was taken directly from the three peaks of the monolayer fitting, fixing all parameters except for the peak intensity. In the second set (light blue), according to the spectral features of standing molecules, the two monolayer peaks at lower binding energy (dark blue) were copied and only variation of intensity and peak position was allowed. In both sets the peak intensity ratio of the appropriate two peaks (blue) was fixed to the ratio found in the monolayer spectrum. The result of this fitting procedure is included in the bottom spectrum as solid lines. Obviously, the result provides a reasonable approximation of experimental data points. In-

terestingly, the resulting shift between peaks of lying and assumed standing molecules is +0.38 eV in good agreement with the expectations from the valence band data (+0.34 eV). Therefore, the assumption of standing molecules in the second layer is fully supported by the XPS data. Also in the F1s core level a change from mono- to multilayer is observed (Figure 5.28b). Again, the peak position in multilayer is slightly shifted compared to the monolayer. Fitting of the multilayer spectrum is accomplished in the same way as already described for the C1s spectrum, but additionally the ratio of peak area of the two Gaussian functions in the multilayer was fixed to the ratio which was found in the C1s spectrum between peaks of standing and lying molecules. This way a shift of only +0.2 eV between the F1s core levels of lying and standing molecules is found. Although, this value differs from what was found for the C1s core levels and for the HOMO, it is not surprising. Since the fluorine are the outermost atoms, they are only marginally effected by the molecular dipole. In fact, the observed shift could be already reasonably explained by the less efficient photo-hole screening in the second layer. Therefore, also this observation fits perfectly into the proposed growth model. Taking a look again on the SECO of the appropriate molecular films reveals that the work function is lowered by about 0.35 eV upon adsorption of PFP on Cu(111), remaining constant from mono- to multilayer deposition. This shift is explained in first approximation by the 'push-back'-effect of metal surfrace-electrons. Additionally, the adsorption-induced distortion of the molecule on atomic scale as described in detail by Koch et al. has to be taken into account [118]. This distortion leads to a small dipole perpendicular to the molecular plane which affects also lying molecules (see [118] for details).

Finally, the inner structure of PFP as it appeared in STM should be discussed. A close-up is shown in Figure 5.29, which was calculated by correlation averaging of a high resolution image as shown in Figure 5.25b. Apparently, the molecule consists of several defined lobes along and also perpendicular to its long axis. This is highlighted by taking line profiles across the according regions of the molecule presented in the right part of Figure 5.29. The cyan line labeled 'A' along the long axes plotted in the upper diagram reveals five distinct peaks; whereas the green line labeled 'B' perpendicular to the long axis is shown at bottom. There three features can be identified. For comparison the calculated probability distribution according to the HOMO of PFP is plotted additionally into the averaged STM image. Apparently, the five peaks across the long axis can be explained by the five rings within the molecule. The decreasing height of the profile comparing the middle peak to the ones at the ends may originate either from a small bend of the molecule or probably a tip effect. Taking a look at the three

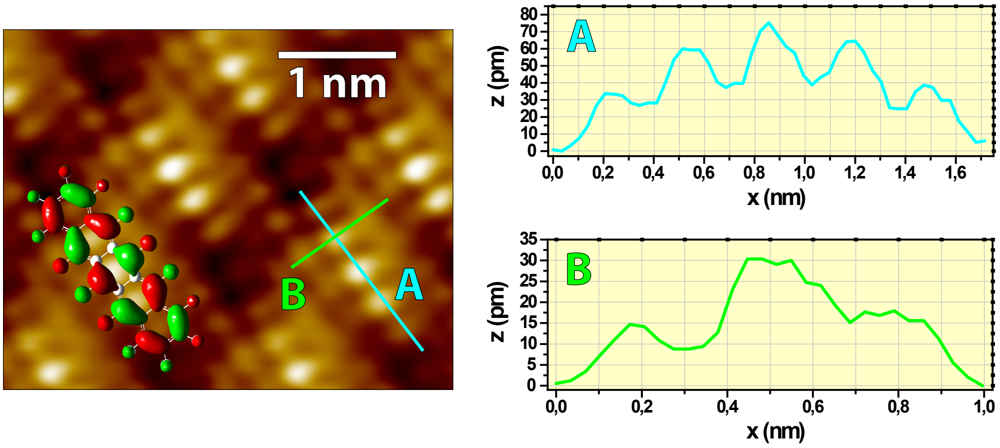

Figure 5.29: Detailed structure of PFP derived by correlation averaging of the ordered structure shown in Figure 5.25b (STM parameters were $U_t = -0.8\,\mathrm{V}$, $I_t = 0.5\,\mathrm{nA}$). On the left of the image the calculated probability density of the PFP HOMO is overlaid and on the right line profiles according to the lines shown in the image are presented. Profile A is referring to the line along the long axes whereas B follows the line perpendicular to it.

features perpendicular to the long axes, one would think they correspond to the contribution of the middle ring plus the two fluorine atoms next to it, at first glance. Indeed, the calculated HOMO shows contributions from the surrounding F atoms. However, the middle ring has no closed probability density perpendicular to the long axis as can be seen in the calculated HOMO of Figure 5.29. Therefore, one would expect to observe a hole within the middle feature in the line profile as well, since this middle hole in the calculated HOMO is even larger than the gap between the ring and the outer F atoms. Of course, these features could also originate from some tip artifact, but tentatively assigning them to originate from the F atoms is more coherent. One has to consider the much more complex environment in the real experiment in contrast to the simulation, which is not included in the calculations and due to the high computational effort virtually not feasible at present. Nevertheless, from high resolution images a flat lying conformation of the molecules can be concluded. Upright standing molecules in higher layers, as proposed from photoemission data, were not observed in STM. Since molecules in standing conformation occupy much less projected area, possibly all STM investigations took place in between patches of standing molecules. On the other hand, standing molecules are much more difficult to image in STM. Perhaps, the tip always penetrated into the layer of standing molecules.

5.3.4 Conclusions

Pentacene (PEN) and its fluorinated derivation perfluoropentacene (PFP) on Cu(111) were investigated by STM. For PEN only closed monolayers could be observed, which showed two different packing patterns. The first one is composed of molecules comprising all the same orientation, whereas the second appears as a zig-zag structure, consisting of molecules with irregular alternating orientation. Using PFP, single molecules and small clusters were observed already at sub-monolayer coverage, which were pinned to step edges and point defects within terraces. By annealing the sample it was possible to induce even more aggregation of molecules. The assumption that molecules reacted with the copper surface at these sites, is actually supported by XPS measurements showing reaction induced chemical shifts of the C1s and F1s core states. Additional UPS measurements reveal a completely loss of semiconducting properties upon annealing, indicating a complete destruction of the conjugated parts of the molecules. From the annealing dependence a rough estimation of the binding energy on the surface of about 1.4 eV was possible. The closed monolayer of PFP was shown to exhibit very similar pattern to what was found for PEN with a slightly larger unit cell. With increasing molecular thickness new features in UPS and XPS indicated a transition of the molecular orientation to an upright standing arrangement.

Consequently, fluorination of PEN enables for strong chemical reactivity of the molecules with the Cu(111) surface. Finally, chemisorption of PFP leads to a complete destruction of these molecules. Nevertheless, by applying an adequate amount of molecules to the surface, ordered self-assembled structures with flat lying molecules within the molecular layer are formed. Moreover, with increasing layer thickness the decreasing substrate influence leads to a change of the molecular orientation (similar to what was observed for HBC on Ag(111) in section 5.2).

5.4 Nano-templating

As it was shown so far, one of the challenges in the field of molecular electronics is to realize good electrical contact between the metal electrode and an individual molecule while at the same time avoid strong electrode-molecule interactions. Such interactions have great impact on the molecule's electronic structure, which often results in modified functionality and properties of the molecule, including the charge transport [123], luminescence properties [124, 125] and the switching ability [126–128]. Compared to the individual molecule in the gas phase or in the solid bulk the electronic properties of organic molecules are often significantly altered when in contact with a metal surface. This can have different origins, e.g. hybridization of the LUMO with metal bands, reported for instance for C_{60} on Au, Ag and Cu [129, 130], tetrafluoro-tetracyanoquinodimethane (F4TCNQ) on Au [131] and Cu(111) [132] or perylene-3,4,9,10-tetracarboxylic-3,4,9,10-dianhydride (PTCDA) on Ag(111) and Ag(110) [133]. Even for weak adsorbed molecules modifications of the electronic structure were reported, e.g. induced by changes of the molecular conformation [108, 134] and molecular level broadening [135, 136]. Retaining the intrinsic (bulk) electronic structure of a molecule requires to reduce the direct molecule metal interaction. To achieve this, several approaches have been reported, e.g. the insertion of oxide [137, 138], ionic salt [125, 139] or molecular [124, 140] buffer layers. Unfortunately, all mentioned methods prevent an intimate contact of the active molecule to the metal, which results in an additional barrier for charge transport between the electrode and active organic material, due to the wide energy gap of the buffer materials.

In this section the use of an organic material is presented, which serves as a template rather then a buffer layer, while retaining the electronic properties of an adsorbed molecule. The successful use of template materials was reported for example for C_{60} on a C_{60}-pentacene nanomesh [141] and C_{60} on different metal carboxylates [142]. Here, the prototypical molecule hexaazatriphenylene-hexanitrile (HATCN) is used, which is presented in Figure 5.30a. This molecule was assembled on the Ag(111) surface. Also in this work the well known molecule C_{60} was utilized as 'test-molecule' (Figure 5.30b). Although, several investigations on C_{60} on pristine Ag(111) were already reported, experiments on this system were reproduced within this work and will be briefly discussed in order to clearly pose the problem of contacting individual molecules on surfaces. For details about the Ag(111) substrate material please refer to section 5.2.1.

5.4.1 Structural properties

In a first experiment about one monolayer of C_{60} was deposited onto Ag(111). In agreement with earlier results [143, 144], this leads to a hexagonal $2\sqrt{3} \times 2\sqrt{3}R30°$ structure shown in Figure 5.31. The lattice parameter of this hexagonal structure is $(0.96 \pm 0.04)\,\mathrm{nm}$, which was also confirmed by LEED analysis. The inter-molecular distance corresponds to that found in bulk C_{60} [145] and indicates a close packing of C_{60} facilitating pronounced lateral inter-molecular interactions within the monolayer.

As the next step sub-monolayer HATCN (nominal mass thickness of about 2 Å) was deposited onto clean Ag(111). As observed by STM, HATCN

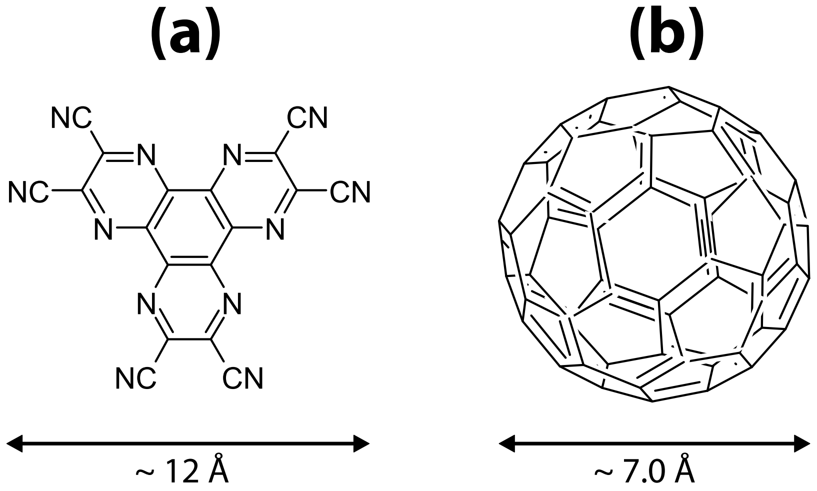

Figure 5.30: Chemical structures of (a) hexaazatriphenylene-hexanitrile (HATCN, $C_{18}N_{12}$) (b) C_{60} (also known as buckyball or Buckminsterfullerene).

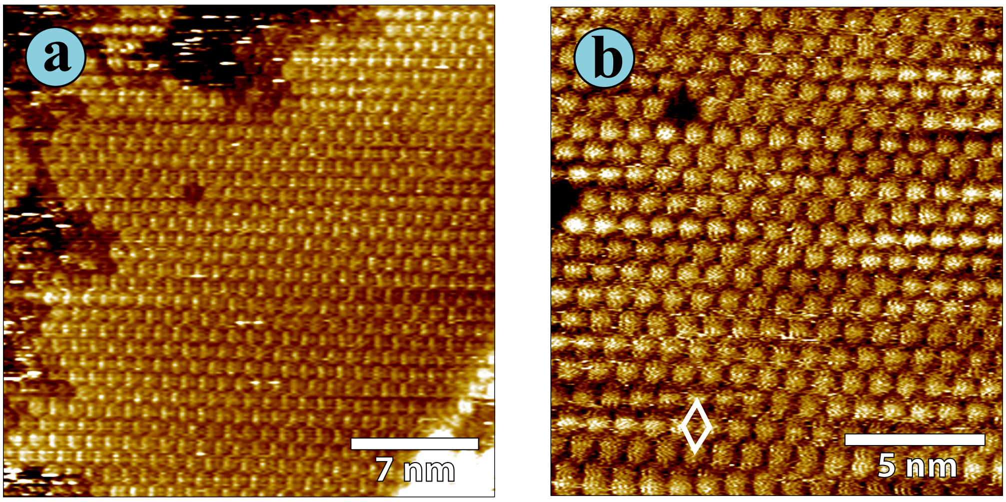

Figure 5.31: STM images of about monolayer coverage C_{60} on Ag(111). (a) Overview revealing high order on long range. ($U_t = -0.1\,\mathrm{V}$, $I_t = 0.8\,\mathrm{nA}$) (b) Magnification where single atoms can be clearly identified. The box at the bottom marks the unit cell of the $2\sqrt{3} \times 2\sqrt{3}R30°$ structure. ($U_t = -0.1\,\mathrm{V}$, $I_t = 0.8\,\mathrm{nA}$)

molecules form a highly ordered structure shown in Figure 5.32. Individual HATCN molecules can be clearly discerned in Figure 5.32c. They appear in a triangular shape, which matches with the outline of the chemical structure of HATCN shown in Figure 5.30a for a planar conformation of the molecule. Therefore, HATCN molecules are expected to lie flat on the surface. Interestingly, six HATCN molecules form one closed ring-like feature, leaving a hole in its center. This gives rise to a honeycomb structure providing an array of nano-cavities. The unit cell can be constructed as hexagonal structure with two molecules per cell and lattice parameter of (2.0 ± 0.1) nm. This structure was also confirmed by LEED investigations shown in Figure 5.33a revealing a clear hexagonal LEED pattern. The defect density within the HATCN layer, e.g. molecules missing within the ordered structure, was slightly larger than what was found for C_{60} on Ag(111) (Figure 5.31). Compared to HATCN, C_{60}/Ag(111) forms a much denser structure. This implies a higher intermolecular interaction which in turn makes it less vulnerable for defects.

Figure 5.32d shows a simulated STM image, obtained within the Tersoff-Hamann approach [30] for HATCN molecules arranged in a honeycomb pattern. The molecular alignment with respect to the underlying substrate used for this calculation is shown in Figure 5.33b. Conformation of molecules in this structure was optimized for individual molecules on Ag(111). Unfortunately, due to the considerable size of the HATCN molecule and the resulting very large unit cell, optimizing the geometry of the whole structure was not possible with state of the art computer clusters. The excellent agreement with the experiment allows an unambiguous correlation of the STM features with the internal structure of the adsorbate and also confirms the face-on orientation of adsorbed molecules. From the theoretical optimization of a single molecule (for details see section 4.4) HATCN is found to be geometrically distorted, i.e. bent, on the surface. The distance between surface and lowest HATCN atom is computed at 2.54 Å. Since van der Waals forces are not considered in common GGA-type functionals, this distance should be regarded as upper limit. In order to check the consistency of the results, the electronic structure of HATCN has been calculated also at closer distances. No qualitative differences were observed.

Higher depositions of HATCN on Ag(111) were also investigated by STM. Already at nominal mass thickness of about 4 Å the formation of several clusters was observed, indicating three dimensional growth of Stranski-Krastanov type (cf. section 2.4.3). Therefore, STM images taken at these samples were much less stable. This is most likely caused by weakly bound HATCN molecules within the second layer, which were easily picked up by the tip while scanning. However, images taken at the monolayer in between clusters as well as LEED investigations still confirmed the existence of exactly the

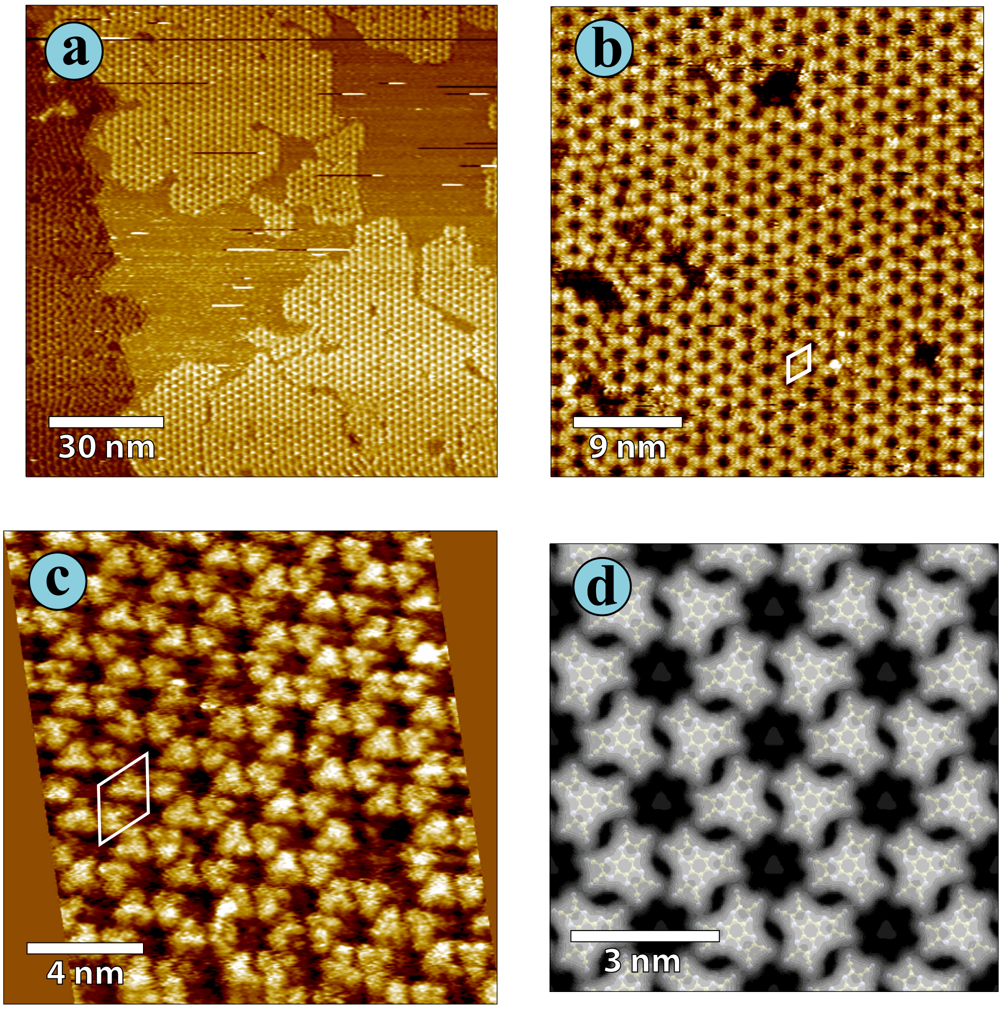

Figure 5.32: (a)-(c) STM images of sub-monolayer HATCN on Ag(111) at different magnifications. The white box marks the unit cell with two molecules per cell. (a),(b) $U_t = -1.2\,\mathrm{V}$, $I_t = 0.2\,\mathrm{nA}$ (c) $U_t = -1.0\,\mathrm{V}$, $I_t = 0.3\,\mathrm{nA}$ (d) Simulated STM image of a HATCN monolayer on Ag(111) (for details see text). The structures of the individual HATCN molecules are overlaid as a guide to the eye to be able to correlate the STM picture with the molecular arrangement.

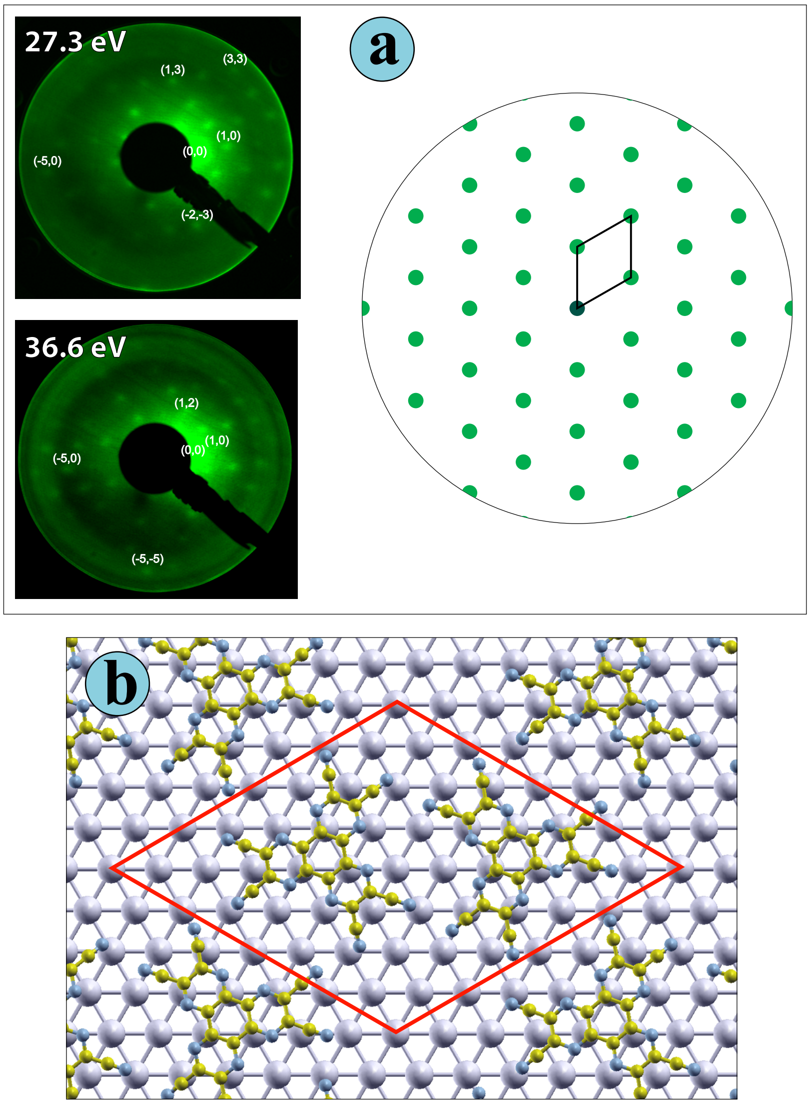

Figure 5.33: (a) LEED images of (sub-)monolayer deposition HATCN on Ag(111). Some LEED spots are labeled for better visualization. On the right side the schematic pattern derived from the LEED images including the hexagonal reciprocal unit cell is shown. (b) Molecular alignment with respect to the underlying Ag(111) lattice as employed for STM and density of states calculations. Only the top metal layer is shown. The geometry of the individual HATCN molecules was obtained by optimization of a single HATCN in a $7 \times 4\sqrt{3}$ unit cell. Arrangement and packing density were inferred from the STM experiments, see section 4.4. The red box marks the unit cell containing two molecules.

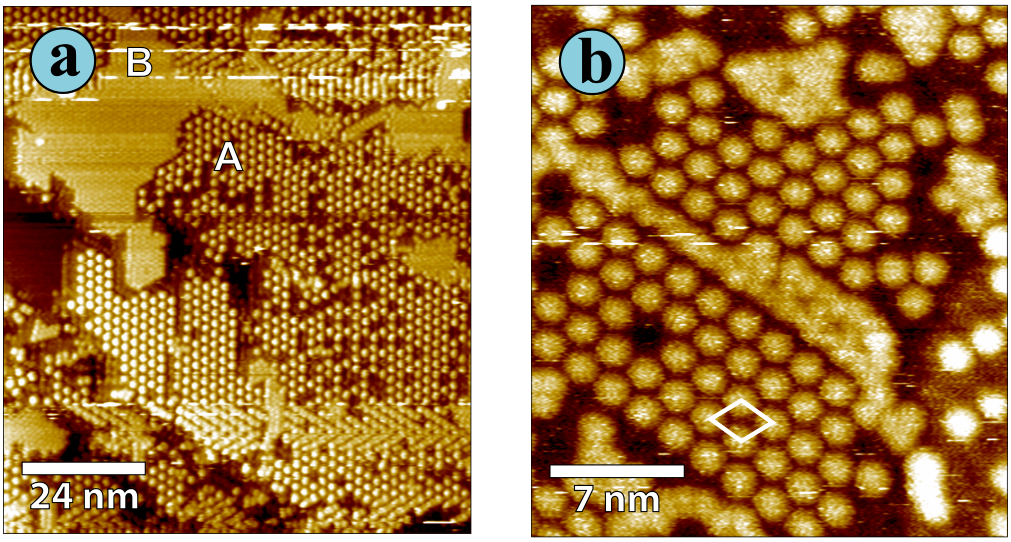

Figure 5.34: Sub-monolayer deposition of C_{60} onto the template of HATCN/Ag(111). (a) STM image on large scale revealing different domains, i.e. hexagonal packed C_{60} (labeled A) and areas with closed appearance (labeled B). ($U_t = 1.0\,\mathrm{V}$, $I_t = 0.3\,\mathrm{nA}$) (b) Magnification of the hexagonal structure of domain A. Individual C_{60} molecules can be clearly identified. ($U_t = 1.0\,\mathrm{V}$, $I_t = 0.3\,\mathrm{nA}$)

same ordered structure as discussed above.

The hexagonal array of nano-cavities build by HATCN molecules can now serve as template for the adsorption of individual isolated C_{60} molecules. For these experiments the formerly discussed sub-monolayer deposition of HATCN molecules was chosen in order to prevent the formation of three dimensional islands. Indeed, after deposition of sub-monolayer C_{60} onto HATCN/Ag(111) the STM evidences an inverted hexagonal pattern, presented in Figure 5.34. In the long range scan of Figure 5.34a two different domains are apparent, labeled A and B. Most area is covered by a clearly visible hexagonal pattern (domain A) for which a magnification is shown in Figure 5.34b. There, single molecules can be easily identified. Corresponding LEED images are shown in Figure 5.35. From the analysis of STM and LEED images exactly the same structural parameters as already found for HATCN/Ag(111) are derived, i.e. hexagonal unit cell with lattice parameter of $(2.0 \pm 0.1)\,\mathrm{nm}$, but this time including only one molecule per cell. The bright round protrusions in Figure 5.34 are thus assigned to C_{60} molecules that have locked into the nano-cavities of the HATCN layer. Unfortunately, a reliable calculation of the STM pictures for that structure was not possi-

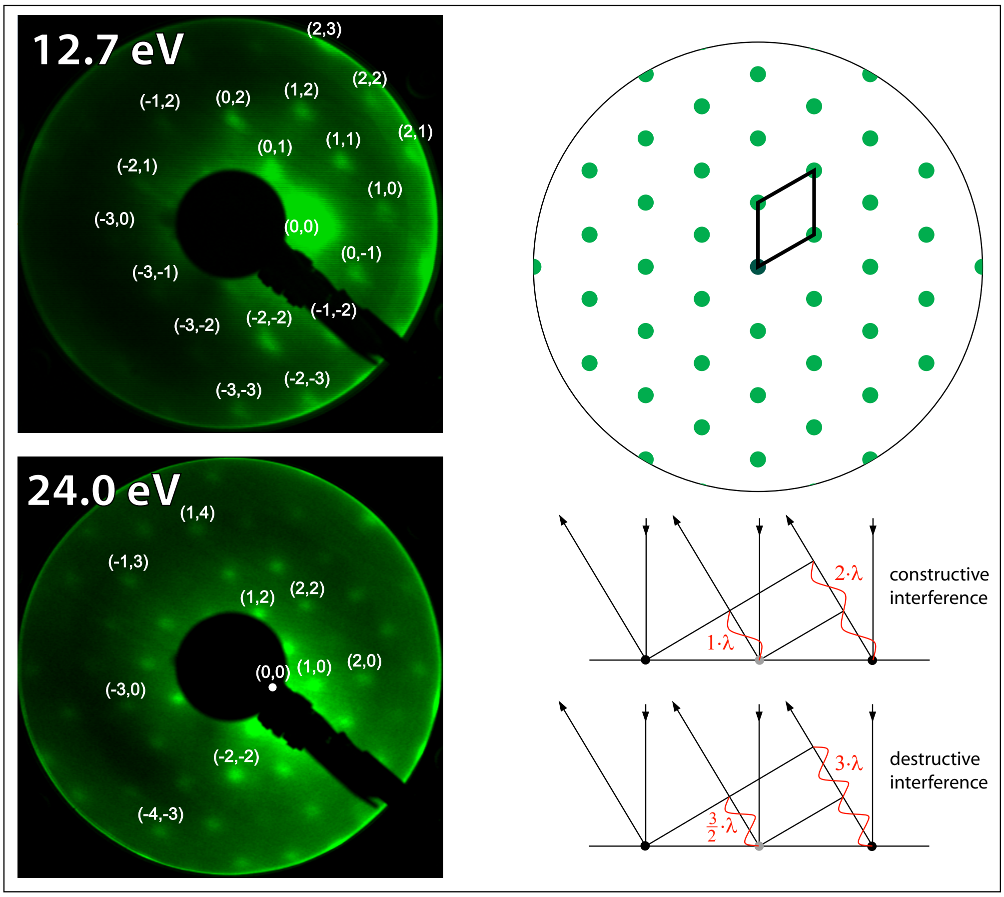

Figure 5.35: LEED images of C_{60} on HATCN/Ag(111). Some of the LEED spots are labeled for better visualization. A construction of relevant LEED spots is shown on the right including the hexagonal reciprocal unit cell marked as black box. At bottom a schematic drawing of the scattering process is shown for different orders of the electron wavelength (see text for details).

ble, considering that the interaction between C_{60} and HATCN is expected to display a dominant van der Waals character, which is not accounted for in GGA based density functional theory calculations.

The second domain observed as larger patches in Figure 5.34a (labeled B) and small clusters in Figure 5.34b has a much denser appearance. In contrast to the domains with C_{60} locked into HATCN nano-cavities (A), within this second type of domain (B) almost no inner structure can be identified. Indeed, imaging the inner structure of these dense areas was much more difficult. A STM image with better resolution inside this area (but unfortunately worse image quality of the surrounding domain) is shown in Figure 5.36a. Further magnification, shown in Figure 5.36b, reveals exactly the same packing found for C_{60} directly on Ag(111) (cf. Figure 5.31b). Apparently, these areas can be assigned to C_{60} lying directly on the substrate at positions where the underlying HATCN layer is not closed (cf. Figure 5.32a). Consequently, the two domains are expected to appear at different heights with respect to the substrate surface because domain B represents the first and domain A the second layer of molecules. Obviously, no significant change in contrast between the two domains can be observed in Figure 5.34. This can be explained by the additional state found at the Fermi edge of C_{60} on Ag(111), which contributes to the tunneling process. Further details are given below in section 5.4.2.

The co-existence of two domains with different lattice parameters gives rise to further discussion of the LEED images taken at these samples (Figure 5.35). Referring to equation (3.16) LEED spots of even order appear exactly at the same positions as spots of a lattice with half of the size and half of the order. For example, the hexagonal lattice of C_{60} on HATCN/Ag(111) with lattice parameter a generates spots of second order $n = 2$ at:

$$\sin\varphi \propto \frac{2}{a} = \frac{1}{a/2} = \frac{1}{b} \tag{5.5}$$

which are equal to the hexagonal lattice of C_{60} directly on Ag(111) with lattice parameter $b = a/2$ and order $n = 1$. Furthermore, taking a closer look on the scattering process leads to the following expected behavior (see bottom right of Figure 5.35). First, it will be assumed that an almost even mixing of molecules of packing A with lattice parameter a (black dots) and molecules of packing B with lattice parameter $b = a/2$ (gray spot in between) exists. Then every scattering process on structure A which involves even multiples of the electron wavelength (red curve in Figure 5.35), according to even orders n, will constructive interfere with electrons scattered in the same direction at structure B. In contrast, scattering on structure A with uneven multiples of the electron wavelength, according to uneven orders n, will lead to destructive

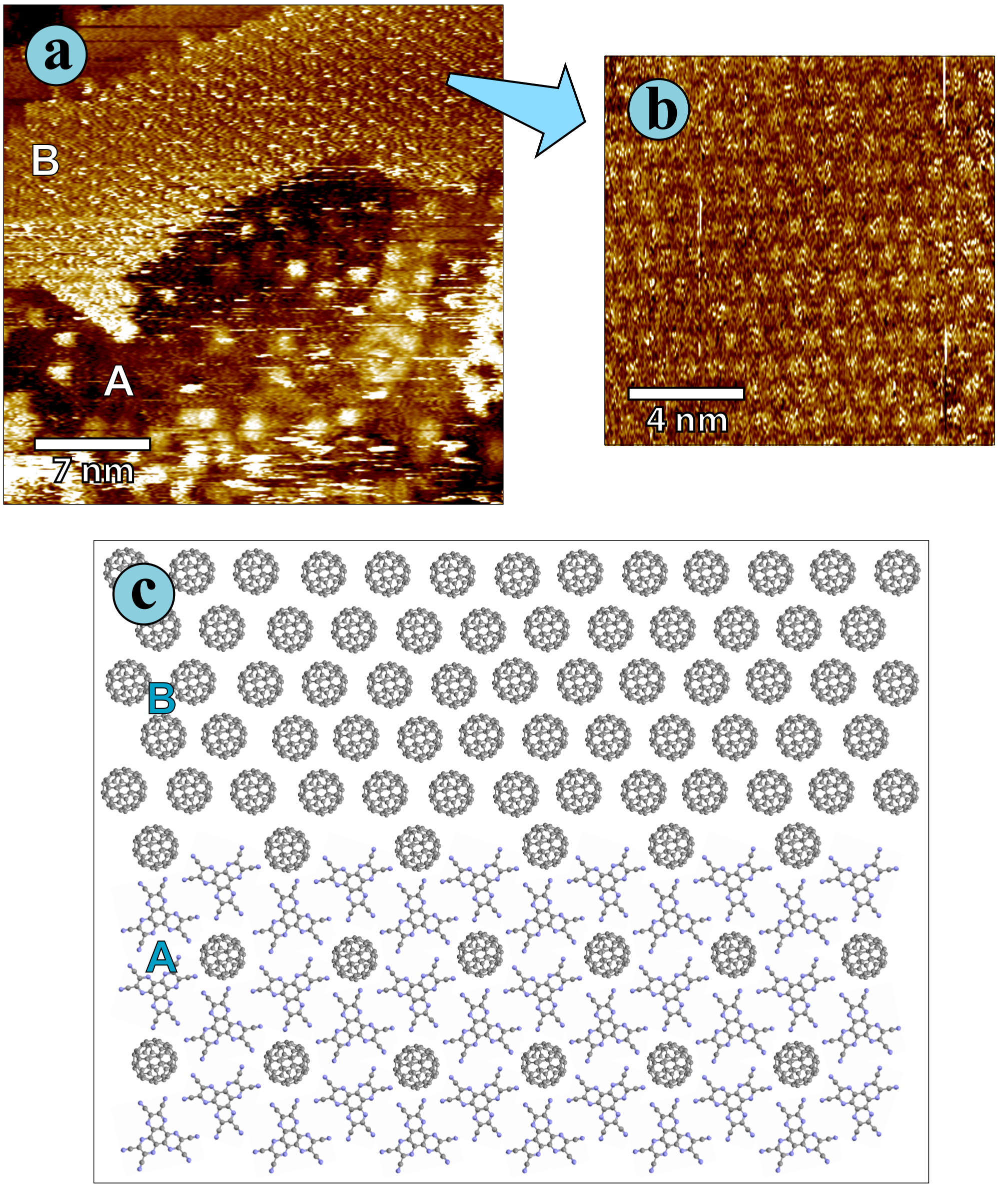

Figure 5.36: (a) STM image resolving the inner structure of the dense area found for C_{60} on HATCN/Ag(111) (domain B, compare to Figure 5.34a). Outside single C_{60} locked into the matrix defined by the HATCN nanocavities are visible (domain A). ($U_t = 0.5\,\mathrm{V}$, $I_t = 0.8\,\mathrm{nA}$) (b) Magnification of the dense area (domain B) revealing exactly the same packing as found for C_{60} directly on Ag(111). ($U_t = 0.1\,\mathrm{V}$, $I_t = 0.8\,\mathrm{nA}$) (c) Schematic model of the molecular layer (underlying substrate is not shown).

interference with electrons scattered on structure B. This is caused by the fractional wavelength occurring at scattering centers B, which results in a 180° phase shift. In case both scattering centers (A and B) are of the same atom species, the resulting pattern would be exactly the same as found for structure B alone. LEED images taken in these experiments (Figure 5.35) reveal diffraction spots which can be assigned to C_{60} on HATCN/Ag(111) (referring to structure A) and no significant intensity variations between the spots appear. Due to the fact that domains with C_{60} directly on Ag(111) are covering much less fractional area and the two domains are well separated from each other, rather than evenly mixed, the derived LEED images are simply a superposition of both diffraction patterns, in which the C_{60}/Ag(111) domains show only minor contributions.

The structural arrangement found by STM is modeled in Figure 5.36c. It comes apparent that individual C_{60} molecules are adsorbed in positions laterally well separated from each other as the lattice constant is 2 nm while the diameter of a C_{60} molecule is only 0.7 nm [146]. It is noted that in STM isolated C_{60} molecules (Figure 5.34) have a larger apparent diameter than in the close packed monolayer directly on Ag(111) (Figure 5.31b and Figure 5.36b) because the STM tip can proceed deeper into the empty trenches between isolated C_{60} and off-surface normal tunneling can contribute due to the finite tip-size. Similar observations, i.e. broadened appearance of C_{60} molecules were also reported by Stepanow *et al.* [147] for C_{60} on metallo-supramolecular nano-cavities on Cu(100) and Zhang *et al.* [141] for C_{60} on a C_{60}-pentacene nanomesh.

A number of point defects of the C_{60} layer are observed in Figure 5.34, where individual molecules are missing. An important observation is that the adsorption energy of C_{60} on the HACTN layer is large enough to enable stable STM imaging of the isolated C_{60} molecules at *room temperature*. Adsorption site jumps of C_{60} between subsequent scans were observed in less than 1% of all images. Such a jump is shown in Figure 5.37. There, two subsequent STM images reveal five positions in the molecular layer, which have changed between the two images (marked by dashed circles). At four of these positions C_{60} molecules have suddenly disappeared while at one position C_{60} is added (most probably moved from one of the other positions). In addition, one single C_{60} molecule without any neighboring molecules in the next-nearest-neighbor distance of 2.0 nm is visible (marked by the arrow in Figure 5.37), which is still in registry with the position of the nano-cavity matrix provided by HATCN/Ag(111). This one has not even changed its position between the two scans of Figure 5.37, demonstrating the rather strong stabilization of C_{60} in the nano-cavities. Consequently, the surrounding area of this single molecule has to be identified as the HATCN template layer. Indeed, by

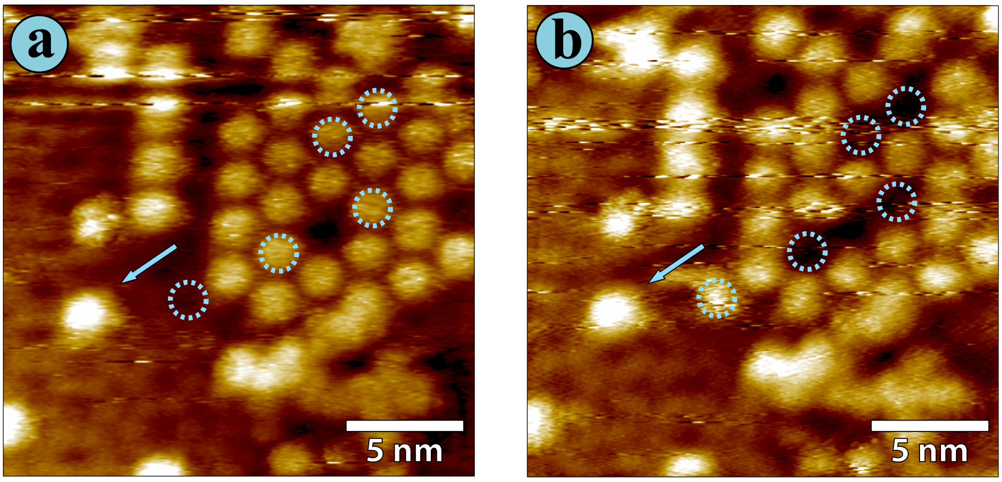

Figure 5.37: Subsequent STM images of C_{60} on HATCN/Ag(111) showing changes of the molecular layer between the two images. Positions at which molecules have either vanished or added are marked by dashed circles. Additionally, one single molecule apart from the closed C_{60} layer but still locking into the matrix defined by the HATCN nano-cavities is marked by the arrow. Interestingly, surrounding this single C_{60} molecule the honeycomb structure of the underlying HATCN layer is visible, nicely confirming that C_{60} locks into the middle hole of the HATCN template. ($U_t = 1.0\,\mathrm{V}$, $I_t = 0.5\,\mathrm{nA}$)

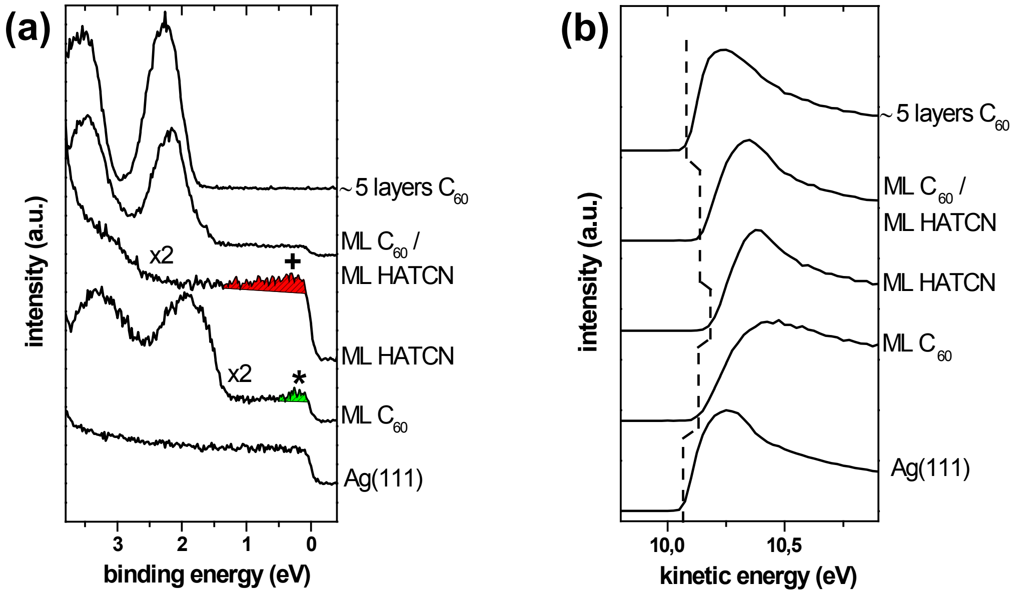

Figure 5.38: (a) UPS spectra of the valence band region for the different samples as indicated (ML = monolayer). The LUMO-derived state at the Fermi level (0 eV binding energy) for C_{60}/Ag(111) is marked by '*'. The LUMO-derived state for HATCN/Ag(111) is marked with '+'. (b) UPS spectra of the according secondary electron cut-off (SECO) taken at -10 V sample bias. The onset shift is marked by the dashed line.

taking a closer look at the area next to the single molecule several objects forming a honeycomb structure become apparent, which fits perfectly with the observed HATCN layer structure (Figure 5.32). The position of the C_{60} relative to the honeycombs nicely confirms the assumption that C_{60} molecules lock into the middle holes of the underlying HATCN template layer.

5.4.2 Electronic properties

Having established that HATCN on Ag(111) is a suitable structural template for the adsorption of individual isolated C_{60} molecules in an ordered manner, the focus should now turn towards the electronic properties investigated by UPS. The appropriate spectra of the different samples are shown in Figure 5.38 for the valence band region and the secondary electron cut-off (SECO) accordingly. Again, firstly the behavior of C_{60} directly on Ag(111) will be discussed.

Compared with the spectrum of pristine Ag(111) (bottom curve in Figure 5.38a) the monolayer (ML) spectrum of C_{60} on Ag(111) shows distinct formation of valence band states (second curve from bottom). As has been already shown by Veenstra *et al.* [148], electron transfer from the metal into the lowest unoccupied molecular orbital (LUMO) leads to significant modification of the molecular electronic structure compared to the bulk, which will be discussed now. For C_{60} multilayers on Ag(111) (topmost curve in Figure 5.38a), the known bulk electronic structure of C_{60} with the fivefold degenerated highest occupied molecular levels is observed [149], forming the peak centered at 2.25 eV binding energy (BE) and the next deeper valence levels centered at 3.5 eV BE. Notably, the electronic structure of the C_{60} monolayer exhibits considerable changes compared to the bulk (second curve from bottom in Figure 5.38a): (i) the two peaks derived from the frontier occupied molecular levels are significantly broadened and shifted ca. 0.4 eV towards lower BE; (ii) additional photoemission intensity (marked by an asterisk in Figure 5.38a) is observed right at the Fermi level (E_F). The new state at the Fermi edge is attributed to electron transfer from the metal to C_{60} leading to a hybridization between molecular orbitals and substrate bands. The band derived from the C_{60} LUMO is thus partially filled, extending the metallic character onto the C_{60} molecules [150, 151] in contrast to bulk C_{60} which is characterized by a 2.3 eV wide energy gap between occupied and unoccupied states [152]. Based on the same effect the broadening of the two other peaks can be explained, while the shift towards lower BE originates from the more efficient photo-hole screening in contact with the highly polarizable metal surface [148]. Important to notice is that all these effects take place only within the first two monolayers of C_{60} as the influence of the substrate can be neglected with increasing distance from the surface [148].

The UPS spectrum of monolayer HATCN/Ag(111) (middle curve in Figure 5.38a) also clearly displays additional photoemission intensity close to E_F (red shaded area marked by '+'), reminiscent of a symmetric peak cut by the Fermi level. This observation is very similar to C_{60}/Ag(111) (second curve from bottom in Figure 5.38a) and PTCDA/Ag(111) [133, 153]. In analogy to the two mentioned examples, it should be proposed that the band resulting from a hybridization of the LUMO-derived HATCN level and the metal states close to E_F is partially filled. This would correspond to extending the metallic character of the Ag substrate onto the adsorbed molecules, a notion that is fully confirmed by the calculations, whose main results are displayed in Figure 5.39b. There the molecular contribution to the total density of states of the Ag/HATCN slab is shown. For this calculation, the experimentally derived unit cell has been employed. Therefore, inter-molecular interactions

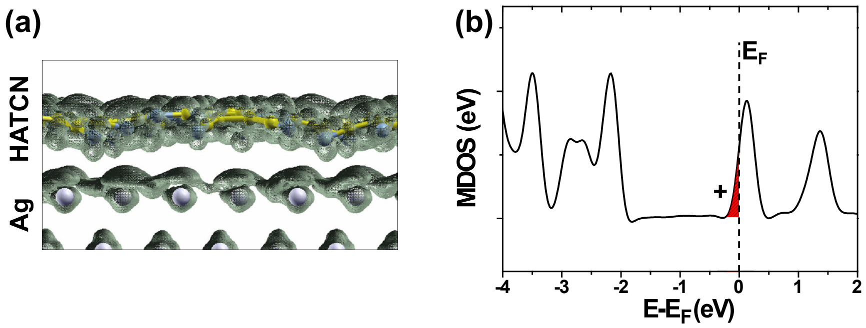

Figure 5.39: (a) Local density of states (LDOS) of HATCN on Ag(111) in the arrangement shown in Figure 5.33b integrated in an energy window of ±0.1 eV above and below the Fermi level E_F. The LDOS extends over both the molecule as well as the Ag substrate, indicating that the metallic character extends onto the HATCN molecules. (b) Calculation of the molecular contribution to the density of states of HATCN/Ag(111) in the arrangement shown in Figure 5.33b. The band associated with the HATCN-LUMO is pinned right at E_F. In analogy to Figure 5.38a, the LUMO-derived state is marked with '+' and red shaded.

are already accounted for. Apparently, E_F cuts right through the LUMO derived band rendering it partly occupied (red shaded area marked by '+' in analogy to the UPS spectrum in Figure 5.38a). This is in full agreement with the experimental observation. Note, to align the simulated spectrum with the experimental data an additional stretching of the energy scale by a factor of 1.3 is necessary, following the usual procedure [132, 154]. In Figure 5.39a an isodensity representation of the local density of states integrated in a window of ±0.1 eV above and below E_F is shown (i.e., the spatial distribution of the electron states around E_F is retrieved). Also, it is clearly visible that the conduction electronic states extend well onto the HATCN layer.

The UPS spectrum of C_{60} on HATCN/Ag(111) (second curve from top in Figure 5.38a) reveals the successful electronic decoupling of the individual C_{60} molecules from the Ag metal. The spectrum closely resembles that of a C_{60} multilayer (top spectrum in Figure 5.38a) regarding both line shape and energy position. Minor differences for C_{60} on HATCN/Ag(111) compared to bulk C_{60} (on Ag) include a shift to lower BE by 0.05 eV and a small shoulder on the low-BE side of the peak derived from the C_{60} frontier orbitals. The reason for the energy shift is the 0.05 eV higher work function of HATCN/Ag(111) compared to the C_{60} monolayer on Ag(111), as derived from the position of the respective secondary electron cut-off spectra in photoemission (discussed further below), and possibly a more efficient photo-hole screening for C_{60} on top of metallic HATCN/Ag(111) as compared to C_{60} bulk [155]. The low-BE shoulder most probably is due to some C_{60} in direct contact with Ag in sample areas that were not covered by HATCN. Such domains found by STM were already discussed above. The fact that the step at E_F can still be observed in the spectrum for C_{60} on the HATCN primed metal surface is due to the fact that the HATCN layer is metallic (and thus exhibits such a step) and not fully covered by C_{60} (only the cavities of the HATCN honeycomb structure are covered by C_{60}), as well as contributions from C_{60} directly on Ag(111) which also has metallic character, see Figure 5.36c.

The secondary electron cut-off (SECO) for all samples is shown in Figure 5.38b. There the bottom curve represents the SECO of the clean Ag(111) substrate, referring to a work function of 4.6 eV. Upon deposition of monolayer C_{60} (second spectrum from bottom) a shift of 0.06 eV towards higher kinetic energy and therefore higher work function occurs. Apparently, C_{60} acts as an acceptor as it even over-compensates the push-back effect which is expected by the adsorption of molecules on the surface. In the multilayer of C_{60} (top curve) the SECO is shifted back to the initial value due to the decreased influence of interface effects. Deposition of monolayer HATCN instead of C_{60} leads to the SECO shown in the middle of Figure 5.38b. Compared to pristine Ag(111) the SECO has shifted by 0.11 eV towards higher kinetic energy, indicating that HATCN acts as an even stronger acceptor on Ag(111) than C_{60} on Ag(111). Putting a monolayer of C_{60} on top of the HATCN template layer leads to a back-shifting the SECO towards lower kinetic energy by 0.04 eV compared to HATCN/Ag(111) (second curve from top). This value remained stable even for higher depositions. Consequently, by introducing HATCN as template layer the work function of the C_{60} layer is increased by 0.07 eV compared to C_{60} on pristine Ag(111).

5.4.3 Conclusions

It was successfully demonstrated how the electronic as well as structural properties of the C_{60}/Ag interface can be finely adjusted by an interfacial HATCN layer, yielding firmly surface-adsorbed isolated C_{60} molecules (with electronic properties not modified by adsorption) at room temperatures. UPS experiments as well as quantum-mechanical modeling reveal that HATCN on Ag(111) exhibits metallic character, in particular a partially filled band at the Fermi level. This allows to realize a metallic contact to C_{60} molecules, while at the same time the chemisorption on the Ag(111) surface including electron transfer from the metal to C_{60} is prevented. Additionally, the honeycomb arrangement of HATCN on Ag(111) provides an ideal template for the adsorption of individual C_{60} molecules in a defined structure, with significantly decreased interaction between neighboring molecules.

6 Conclusions & Outlook

The goal of this work was to improve the understanding of the interplay of the structural and electronic properties of conjugated organic molecules (COM) at interfaces. To achieve this, several complementary techniques were used. The ordering behavior of molecules in thin films was investigated by STM and LEED, whereas for thicker films AFM was used. Information about the orientation of molecules in dependence of the film thickness was obtained from NEXAFS spectroscopy experiments and evaluation of UPS spectra. Conclusions about the inter-molecular and molecule-metal interactions were drawn from the analysis of XPS and UPS spectra as well as from the ordering behavior. Additionally, from UPS spectra information about the semiconducting properties of the materials were derived. Experimental findings were in part supported by theoretical calculations, which were conducted by collaborators.

At first, the influence of alkylation on the ordering of prototypical molecules was demonstrated. Thin films of sexithiophene (6T) on Au(111) were found to grow without taking care of underlying substrate features like the herringbone surface reconstruction. Consequently, in this case the inter-molecular interaction strength is greater than the molecule-metal interaction strength. Substrate step edges were identified as the starting point for the growth of large ordered domains. By the addition of alkyl chains at the ends of the molecule, resulting in α,ω-dihexyl-sexithiophene (DH6T), this growth behavior was significantly changed. Nucleation sites for DH6T were no longer step edges, but kinks of the metal substrate's herringbone surface reconstruction within the terraces. One novel finding was the complete separation of the conjugated cores within the ordered layer. This is in considerable contrast to previous observations on similar systems and leads to a significantly reduced inter-molecular interaction. In consequence, the molecule-metal interaction clearly influences the growth of ordered domains, as observed by the fact that the lateral molecular orientation depended on the underlying herringbone substrate reconstruction. Consequently, by the addition of alkyl chains the ratio between inter-molecular and molecule-metal interaction strength can be tuned. This principle might be further optimized by varying the length of the alkyl chains. For example, in combination with thermal desorption spectroscopy (TDS) a systematic determination of the interface binding energy in dependence of the alkyl chain length would be possible. Furthermore, it was found that single 6T molecules adsorbed at step edges show one dimensional growth, forming closed chains along the steps, before two dimensional growth sets in. In order to adapt the shape of the step edges molecules even changed their conformation. Such behavior has not been reported before for molecular wires. This highlights the relatively high energy gain upon adsorption at these steps (i.e. $> 40\,\text{meV}$, according to the calculations) and is of interesting for future design of molecular wires.

Secondly, the exemplary system hexa-*peri*-hexabenzocoronene (HBC) on Ag(111) was used to demonstrate the fast attenuation of the substrate influence on the molecular ordering. While molecules within the first layer lie flat on the metal surface, in higher layers the known bulk structure of HBC was found. This structural change is accompanied by a change of the molecular orientation with respect to the surface plane. Consequently, within the first layer (possibly also the second) the molecule-metal interaction dominates and in higher layers the growth is only determined by the inter-molecular interactions. Interestingly, in case of HBC on Ag(111) the multilayer bulk structure was found to exhibit indication for one-dimensional electron band formation. Due to the orientation of the molecular π-system, increased electron mobility is expected to occur parallel to the surface plane. Since in devices charge carriers have to be injected from the metal into the organic adlayer (and vice versa), i.e. perpendicular to the surface plane, it seems interesting to explore if this molecular system can be exploited as an efficient active organic layer. When fabricating an organic device the electrodes are usually deposited onto the organic material. This often results in diffusion of the small metal atoms into the organic layer, and thus might establish adequate contact to the molecular structure found in this work. Consequently, building a prototype transistor with this material combination and determining its electrical properties would be interesting.

The third system of interest in this work showed (to some extent) combined effects of the former two systems. Here the growth of well known pentacene (PEN) on Cu(111) was compared to perfluoropentacene (PFP), which is a pentacene in which all hydrogens have been substituted by fluorine. In contrast to PEN, sub-monolayer deposition of PFP resulted in a strong chemical reaction with the substrate surface. Molecules appeared in an unordered phase thereafter. The number of reacted molecules thereby was evaluated statistically, which depicted an increasing number of reaction sites with increasing time. Consequently, it was possible to increase the reaction rate by feeding thermal energy to the system. As evidenced from XPS and UPS measurements, this leads to completely modified chemical environment of the molecule, indicating strong chemisorption, and finally even the loss of semiconducting properties due to a vanishing conjugation of PFP. None of these effects were observed for PEN on the same substrate. Therefore, fluorination not only leads to dominating molecule-metal interaction (like found for DH6T), but literally activates the molecule for strong reactions with the substrate. Nevertheless, after continuous deposition of monolayer thickness PFP, a highly ordered structure was observed. Molecules therein grew flat lying in a side-by-side alignment of their long molecular axis. Surprisingly, this structure is remarkable analogous to the ordered monolayer structure of PEN. Obviously, the formation of an ordered phase is still preferred and depends on the total amount of molecules on the surface. Within the multilayer regime UPS spectra showed clear evidence for an orientational change. Most likely PFP molecules stand up beyond the first layer. This transition has to be investigated in further detail. The molecular dipole generated by the fluorine atoms is strongly orientation dependent and increases the complexity of the interaction regime of this system. A careful determination of the growth behavior, especially at the mono- to multilayer transition, would provide valuable information about the physics of molecular growth with various interaction strengths.

In the fourth system, a completely new approach was made. It was shown that C_{60} on Ag(111) exhibits modified electronic properties compared to the bulk C_{60} crystal, which is often unwanted. To avoid this problem a template layer made of hexaazatriphenylene-hexanitrile (HATCN) was introduced. Although, the metal surface was pre-covered by this intrinsically semiconducting molecule, metallic properties, i.e. electronic states at the Fermi-level, were conserved. Therefore, HATCN serves as metallic like substrate for further growth. Moreover, the honeycomb structure of the HATCN layer provides a matrix of nano-cavities which are traps for subsequent deposited C_{60} molecules. In this way single C_{60} molecules were adsorbed laterally well separated from each other, while remaining very stable at these positions even at *room temperature*. Furthermore, UPS spectra evidenced that C_{60} had been completely electronically decoupled from Ag(111), offering bulk like valence band features. Consequently, by introducing a molecular template layer the electronic and structural properties of the subsequent adlayer could be tuned. As a next step the HATCN/Ag(111) template should be further exploited, by adsorption of other organic molecules on top of it. Especially the behavior upon adsorption of significantly smaller or larger molecules would be of interest. This way the determination of the critical nucleus size and adsorption energy within one nano-cavity is possible. Additionally, the lateral separation of molecules on top of the template layer can be exploited for investigations on quasi single molecules at room temperature, for example by scanning tunneling spectroscopy (STS).

Several different approaches have been demonstrated in this thesis which potentially influence the interaction and ordering behavior at the organic-metal interface. Findings from the presented molecular systems are valuable for the future design and understanding of conjugated molecules at interfaces in organic devices.

Bibliography

[1] J.R. Sheats, H. Antoniadis, M. Hueschen, W. Leonard, J. Miller, R. Moon, D. Roitman, and A. Stocking. Organic Electroluminescent Devices. *Science*, 273:884, 1996.

[2] M. Strukelj, R.H. Jordan, and A. Dodabalapur. Organic Multilayer White Light Emitting Diodes. *J. Am. Chem. Soc.*, 118:1213, 1996.

[3] M.A. Baldo, D.F. O'Brien, Y. You, A. Shoustikov, S. Sibley, M.E. Thompson, and S.R. Forrest. Highly efficient phosphorescent emission from organic electroluminescent devices. *Nature*, 395:151, 1998.

[4] R.H. Friend, R.W. Gymer, A.B. Holmes, J.H. Burroughes, R.N. Marks, C. Taliani, D.D.C. Bradley, D.A. Dos Santos, J.L. Brédas, M. Lögdlund, and W.R. Salaneck. Electroluminescence in conjugated polymers. *Nature*, 397:121, 1999.

[5] L.M. Leung, W.Y. Lo, S.K. So, K.M. Lee, and W.K. Choi. A High-Efficiency Blue Emitter for Small Molecule-Based Organic Light-Emitting Diode. *J. Am. Chem. Soc.*, 122:5640, 2000.

[6] G. Horowitz. Organic Field-Effect Transistors. *Adv. Mater.*, 10:365, 1998.

[7] X.C. Li, H. Sirringhaus, F. Garnier, A.B. Holmes, S.C. Moratti, N. Feeder, W. Clegg, S.J. Teat, and R.H. Friend. A Highly -Stacked Organic Semiconductor for Thin Film Transistors Based on Fused Thiophenes. *J. Am. Chem. Soc.*, 120:2206, 1998.

[8] C.D. Dimitrakopoulos and P.R.L. Malenfant. Organic Thin Film Transistors for Large Area Electronics. *Adv. Mater.*, 14:99, 2002.

[9] Y. Sakamoto, T. Suzuki, M. Kobayashi, Y. Gao, Y. Fukai, Y. Inoue, F. Sato, and S. Tokito. Perfluoropentacene: High-Performance p-n

Junctions and Complementary Circuits with Pentacene. *J. Am. Chem. Soc.*, 126:8138, 2004.

[10] A. Hagfeldt and M. Grätzel. Molecular Photovoltaics. *Acc. Chem. Res.*, 33:269, 2000.

[11] P. Peumans, S. Uchida, and S.R. Forrest. Efficient bulk heterojunction photovoltaic cells using small-molecular-weight organic thin films. *Nature*, 425:158, 2003.

[12] H. Hoppe and N.S. Sariciftci. Organic solar cells: An overview. *J. Mater. Res.*, 19:1924, 2004.

[13] A. Kahn, N. Koch, and W. Gao. Electronic Structure and Electrical Properties of Interfaces between Metals and Pi-Conjugated Molecular Films. *J. Polym. Sci., Part B: Polym. Phys.*, 41:2529–2548, 2003.

[14] C.W. Tang and S.A. VanSlyke. Organic electroluminescent diodes. *Appl. Phys. Lett.*, 51:913, 1987.

[15] J.J.M. Halls, C.A. Walsh, N.C. Greenham, E.A. Marseglia, R.H. Friend, S.C. Moratti, and A.B. Holmes. Efficient photodiodes from interpenetrating polymer networks. *Nature*, 376:498, 1995.

[16] F. Garnier, G. Horowitz, X. Peng, and D. Fichou. An all-organic "soft" thin film transistor with very high carrier mobility. *Adv. Mater.*, 2:592, 1990.

[17] J.E. McGinness. Mobility Gaps: A Mechanism for Band Gaps in Melanins. *Science*, 177:896, 1972.

[18] N. Koch. Organic Electronic Devices and Their Functional Interfaces. *ChemPhysChem*, 8:1438, 2007.

[19] P. Peumans, A. Yakimov, and S.R. Forrest. Small molecular weight organic thin-film photodetectors and solar cells. *J. Appl. Phys.*, 93: 3693, 2003.

[20] H. Vázquez, F. Flores, R. Oszwaldowski, J. Ortega, R. Pérez, and A. Kahn. Barrier formation at metal-organic interfaces: dipole formation and the charge neutrality level. *Appl. Surf. Sci.*, 234:107, 2004.

[21] Peter Williams Atkins. *Physical Chemistry.* Oxford University Press, sixth edition edition, 1998.

[22] Richard H. Tredgold. *Order in thin organic films.* Cambridge University Press, 1994.

[23] R. Hentschke, B.L. Schürmann, and J.P. Rabe. Molecular dynamics simulations of ordered alkane chains physisorbed on graphite. *J. Chem. Phys.*, 96:6213, 1992.

[24] Paolo Samori. *Self-assembly of conjugated (macro)molecules - nanostructures for molecular electronics.* PhD thesis, Humboldt-Universität zu Berlin, 2000.

[25] G. Witte and C. Wöll. Growth of aromatic molecules on solid substrates for applications in organic electronics. *J. Mater. Res.*, 19:1889, 2004.

[26] Gerd Binnig and Heinrich Rohrer. *Nobel Lectures in Physics 1981-1990*, chapter Scanning Tunneling Microscopy - From Birth to Adolescence, page 389. World Scientific Publishing Co., 1986.

[27] G. Binnig and H. Rohrer. Scanning tunneling microscopy. *IBM J. Res. Dev.*, 30:355, 1986.

[28] Roland Wiesendanger. *Scanning Probe Microscopy and Spectroscopy - Methods and Applications.* Cambridge University Press, 1998.

[29] J.G. Simmons. Generalized Formula for the Electric Tunnel Effect between Similar Electrodes Separated by a Thin Insulating Film. *J. Appl. Phys.*, 34:1793, 1963.

[30] J. Tersoff and D.R. Hamann. Theory and Application for the Scanning Tunneling Microscope. *Phys. Rev. Lett.*, 50:1998, 1983.

[31] J. Tersoff and D.R. Hamann. Theory of the scanning tunneling microscope. *Phys. Rev. B*, 31:805, 1985.

[32] J. Bardeen. Tunnelling from a Many-Particle Point of View. *Phys. Rev. Lett.*, 6:57, 1961.

[33] C.J. Chen. Tunneling matrix elements in three-dimensional space: The derivative rule and the sum rule. *Phys. Rev. B*, 42:8841, 1990.

[34] M. Büttiker, Y. Imry, R. Landauer, and S. Pinhas. Generalized many-channel conductance formula with application to small rings. *Phys. Rev. B*, 31:6207, 1985.

[35] Y. Meir and N.S. Wingreen. Landauer formula for the current through an interacting electron region. *Phys. Rev. Lett.*, 68:2512, 1992.

[36] J.K. Spong, H.A. Mizes, L.J. LaComb Jr, M.M. Dovek, J.E. Frommer, and J.S. Foster. Contrast mechanism for resolving organic molecules with tunnelling microscopy. *Nature*, 338:137, 1989.

[37] W. Mizutani, M. Shigeno, K. Kajimura, and M. Ono. Tunneling through a deformed potential. *Ultramicroscopy*, 42-44:236, 1992.

[38] G. Binnig, C.F. Quate, and C. Gerber. Atomic Force Microscope. *Phys. Rev. Lett.*, 56:930, 1986.

[39] Jacob N. Israelachvili. *Intermolecular And Surface Forces.* Academic Press Inc., 1998.

[40] Louis de Broglie. *Nobel Lectures in Physics 1922-1941*, chapter The Wave Nature of the Electron, page 244. Elsevier Publishing Company, 1929.

[41] C. Davisson and L.H. Germer. The Scattering of Electrons by a Single Crystal of Nickel. *Nature*, 119:558, 1927.

[42] C. Davisson and L.H. Germer. Diffraction of Electrons by a Crystal of Nickel. *Phys. Rev.*, 30:705, 1927.

[43] H. Hertz. Ueber einen Einfluss des ultravioletten Lichtes auf die electrische Entladung. *Ann. Phys.*, 31:421, 1887.

[44] A. Einstein. Über einen die Erzeugung und Verwandlung des Lichtes betreffenden heuristischen Gesichtspunkt. *Ann. Phys.*, 17:132, 1905.

[45] Joachim Stöhr. *NEXAFS Spectroscopy.* Springer Series in Surface Sciences , Vol. 25. Springer, 2nd edition, 2003.

[46] A.L. Johnson, E.L. Muetterties, J. Stöhr, and F. Sette. Chemisorption geometry of pyridine on platinum(111) by NEXAFS. *J. Phys. Chem.*, 89:4071, 1985.

[47] M. Bader, J. Haase, K.H. Frank, A. Puschmann, and A. Otto. Orientational Phase Transition in the System Pyridine/Ag(111): A Near-Edge X-Ray-Absorption Fine-Structure Study. *Phys. Rev. Lett.*, 56: 1921, 1986.

[48] I. Horcas, R. Fernández, J.M. Gómez Rodríguez, and J. Colchero. WSXM: A software for scanning probe microscopy and a tool for nanotechnology. *Rev. Sci. Instrum.*, 78:013705, 2007.

[49] A. Schöll, Y. Zou, T. Schmidt, R. Fink, and E. Umbach. Energy calibration and intensity normalization in high-resolution NEXAFS spectroscopy. *J. Electron. Spectrosc.*, 129:1–8, 2003.

[50] A.D. Becke. Density-functional thermochemistry. III. The role of exact exchange. *J. Chem. Phys.*, 98:5648, 1993.

[51] M.J. Frisch and et al. *GAUSSIAN 03 revision D.1.* Wallingford, CT, 2005.

[52] G. Kresse and J. Hafner. Ab initio molecular dynamics for open-shell transition metals. *Phys. Rev. B*, 48:13115, 1993.

[53] G. Kresse and J. Hafner. Ab initio molecular dynamics for liquid metals. *Phys. Rev. B*, 47:558, 1993.

[54] G. Kresse and J. Hafner. Ab initio molecular-dynamics simulation of the liquid-metal-amorphous-semiconductor transition in germanium. *Phys. Rev. B*, 49:14251, 1994.

[55] G. Kresse and J. Furthmüller. Efficient iterative schemes for ab initio total-energy calculations using a plane-wave basis set. *Phys. Rev. B*, 54:11169, 1996.

[56] P.E. Blöchl. Projector augmented-wave method. *Phys. Rev. B*, 50: 17953, 1994.

[57] G. Kresse and D. Joubert. From ultrasoft pseudopotentials to the projector augmented-wave method. *Phys. Rev. B*, 59:1758, 1999.

[58] H.J. Monkhorst and J.D. Pack. Special points for Brillouin-zone integrations. *Phys. Rev. B*, 13:5188, 1976.

[59] G. Heimel, L. Romaner, J.L. Brédas, and E. Zojer. Interface Energetics and Level Alignment at Covalent Metal-Molecule Junctions: PI-Conjugated Thiols on Gold. *Phys. Rev. Lett.*, 96:196806, 2006.

[60] J. Tersoff. Method for the calculation of scanning tunneling microscope images and spectra. *Phys. Rev. B*, 40:11990, 1989.

[61] G. Heimel, L. Romaner, J.L. Brédas, and E. Zojer. Organic/metal interfaces in self-assembled monolayers of conjugated thiols: A first-principles benchmark study. *Surf. Sci.*, 600:4548, 2006.

[62] L. Torsi, A. Dodabalapur, L.J. Rothberg, A.W.P. Fung, and H.E. Katz. Intrinsic Transport Properties and Performance Limits of Organic Field-Effect Transistors. *Science*, 272:1462, 1996.

[63] G. Horowitz, P. Delannoy, H. Bouchriha, F. Deloffre, J.L. Fave, F. Garnier, R. Hajlaoui, M. Heyman, F. Kouki, P. Valat, V. Wintgens, and A. Yassar. Two-layer light-emitting diodes based on sexithiophene and derivatives. *Adv. Mater.*, 6:752, 1994.

[64] H. Inoue, G. Yoshikawa, and K. Saiki. Molecular Chain Structure of α-Sexithienyl on Ag(110) Observed by Scanning Tunneling Microscopy. *Jpn. J. Appl. Phys.*, 45:1794, 2006.

[65] G. Yoshikawa, M. Kiguchi, S. Ikeda, and K. Saiki. Molecular orientations and adsorption structures of α-sexithienyl thin films grown on Ag(110) and Ag(111) surfaces. *Surf. Sci.*, 559:77, 2004.

[66] M. Kiguchi, S. Entani, K. Saiki, and G. Yoshikawa. One-dimensional ordered structure of α-sexithienyl on Cu(110). *Appl. Phys. Lett.*, 84: 3444, 2004.

[67] S. Prato, L. Floreano, D. Cvetko, V. Renzi, A. Morgante, S. Modesti, F. Biscarini, R. Zamboni, and C. Taliani. Anisotropic Ordered Planar Growth of α-Sexithienyl Thin Films. *J. Phys. Chem. B*, 103:7788, 1999.

[68] A.J. Mäkinen, J.P. Long, N.J. Watkins, and Z.H. Kafafi. Sexithiophene Adlayer Growth on Vicinal Gold Surfaces. *J. Phys. Chem. B*, 109:5790, 2005.

[69] M. Kiel, K. Duncker, C. Hagendorf, and W. Widdra. Molecular structure and chiral separation in α-sexithiophene ultrathin films on Au(111): Low-energy electron diffraction and scanning tunneling microscopy. *Phys. Rev. B*, 75:195439, 2007.

[70] F. Garnier, A. Yassar, R. Hajlaoui, G. Horowitz, F. Deloffre, B. Servet, S. Ries, and P. Alnot. Molecular engineering of organic semiconductors: design of self-assembly properties in conjugated thiophene oligomers. *J. Am. Chem. Soc.*, 115:8716–8721, 1993.

[71] A. Stabel and J.P. Rabe. Scanning tunnelling microscopy of alkylated oligothiophenes at interfaces with graphite. *Synth. Met.*, 67:47–53, 1994.

[72] L. Rossi, G. Lanzani, and F. Garnier. Charged photoexcitations in thiophene-based molecular semiconductors. *Phys. Rev. B*, 58:6684, 1998.

[73] P. Lang, C. Nogues, S. Verneyre, F. Demanze, P. Srivastava, F. Garnier, J.C. Wittmann, B. Lotz, and C. Straupé. Orientation and structure of thin films of α, ω-dihexyl sexithiophene deposited onto PTFE oriented by friction. *J. Chim. Phys. Phys.- Chim. Biol.*, 95:1286, 1998.

[74] S. Duhm, G. Heimel, I. Salzmann, H. Glowatzki, R.L. Johnson, J.P. Rabe A. Vollmer, and N. Koch. Orientation-dependent ionization energies and interface dipoles in ordered molecular assemblies. *Nat. Mater.*, 7:326, 2008.

[75] C. Wöll, S. Chiang, R.J. Wilson, and P.H. Lippel. Determination of atom positions at stacking-fault dislocations on Au(111) by scanning tunneling microscopy. *Phys. Rev. B*, 39:7988, 1989.

[76] J.V. Barth, H. Brune, G. Ertl, and R.J. Behm. Scanning tunneling microscopy observations on the reconstructed Au(111) surface: Atomic structure, long-range superstructure, rotational domains, and surface defects. *Phys. Rev. B*, 42:9307–9318, 1990.

[77] S.J. Stranick, M.M. Kamna, and P.S. Weiss. Interactions and dynamics of benzene on Cu(111) at low temperature. *Surf. Sci.*, 338:41–59, 1995.

[78] M. Eremtchenko, R. Temirov, D. Bauer, J.A. Schaefer, and F.S. Tautz. Formation of molecular order on a disordered interface layer: Pentacene/Ag(111). *Phys. Rev. B*, 72:115430, 2005.

[79] F. Jäckel, U.G.E. Perera, V. Iancu, K.F. Braun, N. Koch, J.P. Rabe, and S.W. Hla. Investigating Molecular Charge Transfer Complexes with a Low Temperature Scanning Tunneling Microscope. *Phys. Rev. Lett.*, 100:126102, 2008.

[80] I. Chizhov, G. Scoles, and A. Kahn. The Influence of Steps on the Orientation of Copper Phthalocyanine Monolayers on Au(111). *Langmuir*, 16:4358, 2000.

[81] K. Glöckler, C. Seidel, A. Soukopp, M. Sokolowski, E. Umbach, M. Böhringer, R. Berndt, and W.D. Schneider. Highly ordered structures and submolecular scanning tunnelling microscopy contrast of PTCDA and DM-PBDCI monolayers on Ag(111) and Ag(110). *Surf. Sci.*, 405:1, 1998.

[82] W. Xiao, P. Ruffieux, K. Aït-Mansour, O. Gröning, K. Palotas, W.A. Hofer, P. Gröning, and R. Fasel. Formation of a Regular Fullerene Nanochain Lattice. *J. Phys. Chem. B*, 110:21394–21398, 2006.

[83] C.E. Check and T.M. Gilbert. Progressive Systematic Underestimation of Reaction Energies by the B3LYP Model as the Number of C-C Bonds Increases: Why Organic Chemists Should Use Multiple DFT Models for Calculations Involving Polycarbon Hydrocarbons. *J. Org. Chem.*, 70:9828, 2005.

[84] G. Liu, J.A. Rodriguez, J. Dvorak, J. Hrbek, and T. Jirsak. Chemistry of sulfur-containing molecules on Au(1 1 1): thiophene, sulfur dioxide, and methanethiol adsorption. *Surf. Sci.*, 505:295, 2002.

[85] R. Otero, Y. Naitoh, F. Rosei, P. Jiang, P. Thostrup, A. Gourdon, E. Lægsgaard, I. Stensgaard, C. Joachim, and F. Besenbacher. One-Dimensional Assembly and Selective Orientation of Lander Molecules on an O-Cu Template. *Angew. Chem. Int. Ed.*, 43:2091, 2004.

[86] J.H. Cho, D.H. Oh, and L. Kleinman. One-dimensional molecular wire on hydrogenated Si(001). *Phys. Rev. B*, 65:081310, 2002.

[87] G.P. Lopinski, D.D.M. Wayner, and R.A. Wolkow. Self-directed growth of molecular nanostructures on silicon. *Nature*, 406:48, 2000.

[88] A. Tracz, A. Stabel, and J.P. Rabe. Influence of Controlled Nanoscale Roughness on Physisorbed Two-Dimensional Crystals at Graphite-Liquid Interfaces. *Langmuir*, 18:9319–9326, 2002.

[89] R. Goddard, M.W. Haenel, W.C. Herndon, C. Krueger, and M. Zander. Crystallization of Large Planar Polycyclic Aromatic Hydrocarbons: The Molecular and Crystal Structures of Hexabenzocoronene and Benzodicoronene. *J. Am. Chem. Soc.*, 117:30–41, 1995.

[90] M. Keil, P. Samori, D.A. Santos, T. Kugler, S. Stafström, J.D. Brand, K. Müllen, J.L. Brédas, J.P. Rabe, and W.R. Salaneck. Influence of the Morphology on the Electronic Structure of Hexa-peri-hexabenzocoronene Thin Films. *J. Phys. Chem. B*, 104:3967–3975, 2000.

[91] L. Gross, F. Moresco, P. Ruffieux, A. Gourdon, C. Joachim, and K.H. Rieder. Tailoring molecular self-organization by chemical synthesis: Hexaphenylbenzene, hexa-peri-hexabenzocoronene, and derivatives on Cu (111). *Phys. Rev. B*, 71:165428, 2005.

[92] P. Ruffieux, O. Gröning, M. Bielmann, C. Simpson, K. Müllen, L. Schlapbach, and P. Gröning. Supramolecular columns of hexabenzocoronenes on copper and gold (111) surfaces. *Phys. Rev. B*, 66:073409, 2002.

[93] C. Kübel, K. Eckhardt, V. Enkelmann, G. Wegner, and K. Müllen. Synthesis and crystal packing of large polycyclic aromatic hydrocarbons: hexabenzo[*bc,ef,hi,kl,no,qr*]coronene and dibenzo[*fg,ij*]phenanthro[9,10,1,2,3-*pqrst*]pentaphene. *J. Mater. Chem.*, 10:879–886, 2000.

[94] R. Friedlein, X. Crispin, C.D. Simpson, M.D. Watson, F. Jäckel, W. Osikowicz, S. Marciniak, M.P. Jong, P. Samori, S.K.M. Jönsson, M. Fahlman, K. Müllen, J.P. Rabe, and W. R. Salaneck. Electronic structure of highly ordered films of self-assembled graphitic nanocolumns. *Phys. Rev. B*, 68:195414, 2003.

[95] V. Lemaur, D.A. Silva-Filho, V. Coropceanu, M. Lehmann, Y. Geerts, J. Piris, M.G. Debije, A.M. Craats, K. Senthilkumar, L.D. Siebbeles, J.M. Warman, J.L. Bredas, and J. Cornil. Charge Transport Properties in Discotic Liquid Crystals: A Quantum-Chemical Insight into Structure-Property Relationships. *J. Am. Chem. Soc.*, 126:3271–3279, 2004.

[96] A.M. Craats, J.M. Warman, A. Fechtenkötter, J.D. Brand, M.A. Harbison, and K. Müllen. Record Charge Carrier Mobility in a Room-Temperature Discotic Liquid-Crystalline Derivative of Hexabenzocoronene. *Adv. Mater.*, 11:1469, 1999.

[97] Thomas Fauster and Wulf Steinmann. *Electromagnetic Waves: Recent Developments in Research*, volume Volume 2: Photonic Probes of Surfaces, chapter 8, pages 347–411. Elsevier (Amsterdam), 1995.

[98] Y. Luo, H. Ågren, M. Keil, R. Friedlein, and W.R. Salaneck. A theoretical investigation of the near-edge X-ray absorption spectrum of hexa-peri-hexabenzocoronene. *Chem. Phys. Lett.*, 337:176–180, 2001.

[99] S. Duhm, H. Glowatzki, J.P. Rabe, N. Koch, and R.L. Johnson. Influence of alkyl chain substitution on sexithienyl-metal interface morphology and energetics. *Appl. Phys. Lett.*, 88:203109, 2006.

[100] O. McDonald, A.A. Cafolla, D. Carty, G. Sheerin, and G. Hughes. Photoemission, NEXAFS and STM studies of pentacene thin films on Au(100). *Surf. Sci.*, 600:3217–3225, 2006.

[101] H. Proehl, M. Toerker, F. Sellam, T. Fritz, K. Leo, C. Simpson, and K. Müllen. Comparison of ultraviolet photoelectron spectroscopy and scanning tunneling spectroscopy measurements on highly ordered ultrathin films of hexa-peri-hexabenzocoronene on Au(111). *Phys. Rev. B*, 63:205409, 2001.

[102] G. Beernink, T. Strunskus, G. Witte, and C. Wöll. Importance of dewetting in organic molecular-beam deposition: Pentacene on gold. *Appl. Phys. Lett.*, 85:398, 2004.

[103] N. Koch, I. Salzmann, R.L. Johnson, J. Pflaum, R. Friedlein, and J.P. Rabe. Molecular orientation dependent energy levels at interfaces with pentacene and pentacenequinone. *Org. Electron.*, 7:537, 2006.

[104] P. Samori, N. Severin, C.D. Simpson, K. Müllen, and J.P. Rabe. Epitaxial composite layers of electron donors and acceptors from very Large polycyclic aromatic hydrocarbons. *J. Am. Chem. Soc.*, 124:9454–9457, 2002.

[105] F. Sellam, T. Schmitz-Hübsch, M. Toerkera, S. Mannsfeld, H. Proehl, T. Fritz, K. Leo, C. Simpson, and K. Müllen. LEED and STM investigations of organic-organic heterostructures grown by molecular beam epitaxy. *Surf. Sci.*, 478:113–121, 2001.

[106] G. Witte, K. Hänel, S. Söhnchen, and C. Wöll. Growth and morphology of thin films of aromatic molecules on metals: the case of perylene. *Appl. Phys. A*, 82:447, 2006.

[107] B. Krause, A.C. Dürr, K. Ritley, F. Schreiber, H. Dosch, and D. Smilgies. Structure and growth morphology of an archetypal system for organic epitaxy: PTCDA on Ag(111). *Phys. Rev. B*, 66:235404, 2002.

[108] N. Koch, G. Heimel, J. Wu, E. Zojer, R.L. Johnson, J.L. Brédas, K. Müllen, and J.P. Rabe. Influence of molecular conformation on organic/metal interface energetics. *Chem. Phys. Lett.*, 413:390, 2005.

[109] N. Koch, A. Vollmer, I. Salzmann, B. Nickel, H. Weiss, and J.P. Rabe. Evidence for Temperature-Dependent Electron Band Dispersion in Pentacene. *Phys. Rev. Lett.*, 96:156803, 2006.

[110] S. Lee, B. Koo, J. Shin, E. Lee, H. Park, and H. Kim. Effects of hydroxyl groups in polymeric dielectrics on organic transistor performance. *Appl. Phys. Lett.*, 88:162109, 2006.

[111] T.B. Singh, P. Senkarabacak, N.S. Sariciftci, A. Tanda, C. Lackner, R. Hagelauer, and G. Horowitz. Organic inverter circuits employing ambipolar pentacene field-effect transistors. *Appl. Phys. Lett.*, 89: 033512, 2006.

[112] Y. Inoue, Y. Sakamoto, T. Suzuki, M. Kobayashi, Y. Gao, and S. Tokito. Organic Thin-Film Transistors with High Electron Mobility Based on Perfluoropentacene. *Jpn. J. Appl. Phys.*, 44:3663, 2005.

[113] J.H. Kang and X.Y. Zhu. Pi-stacked pentacene thin films grown on Au(111). *Appl. Phys. Lett.*, 82:3248, 2003.

[114] E. Annese, C.E. Viol, B. Zhou, J. Fujii, I. Vobornik, C. Baldacchini, M.G. Betti, and G. Rossi. Self organization of pentacene grown on Cu(119). *Surf. Sci.*, 601:4242, 2007.

[115] Q. Chen, A.J. McDowall, and N.V. Richardson. Ordered Structures of Tetracene and Pentacene on Cu(110) Surfaces. *Langmuir*, 19:10164, 2003.

[116] J. Lagoute, K. Kanisawa, and S. Fölsch. Manipulation and adsorption-site mapping of single pentacene molecules on Cu(111). *Phys. Rev. B*, 70:245415, 2004.

[117] N. Koch, A. Vollmer, S. Duhm, Y. Sakamoto, and T. Suzuki. The Effect of Fluorination on Pentacene/Gold Interface Energetics and Charge Reorganization Energy. *Adv. Mater.*, 19:112, 2007.

[118] N. Koch, A. Gerlach, S. Duhm, H. Glowatzki, G. Heimel, A. Vollmer, Y. Sakamoto, T. Suzuki, J. Zegenhagen, J.P. Rabe, and F. Schreiber. Adsorption-Induced Intramolecular Dipole: Correlating Molecular Conformation and Interface Electronic Structure. *J. Am. Chem. Soc.*, 130:7300, 2008.

[119] P.A. Redhead. Thermal desorption of gases. *Vacuum*, 12:203, 1962.

[120] S. Söhnchen, S. Lukas, and G. Witte. Epitaxial growth of pentacene films on Cu(110). *J. Chem. Phys.*, 121:525, 2004.

[121] A. Bismarck, R. Tahhan, J. Springer, A. Schulz, T.M. Klapötke, H. Zeil, and W. Michaeli. Influence of fluorination on the properties of carbon fibres. *J. Fluorine Chem.*, 84:127, 1997.

[122] I. Salzmann, S. Duhm, G. Heimel, M. Oehzelt, R. Kniprath, R.L. Johnson, J.P. Rabe, and N. Koch. Tuning the ionization energy of organic-semiconductor films: The role of polar intramolecular polar bonds. *J. Am. Chem. Soc.*, 130:12870, 2008. submitted.

[123] R. Temirov, S. Soubatch, A. Luican, and F.S. Tautz. Free-electron-like dispersion in an organic monolayer film on a metal substrate. *Nature*, 444:350, 2006.

[124] Z.C. Dong, X.L. Guo, A.S. Trifonov, P.S. Dorozhkin, K. Miki, K. Kimura, S. Yokoyama, and S. Mashiko. Vibrationally Resolved Fluorescence from Organic Molecules near Metal Surfaces in a Scanning Tunneling Microscope. *Phys. Rev. Lett.*, 92:086801, 2004.

[125] E. Ćavar, M.C. Blüm, M. Pivetta, F. Patthey, M. Chergui, and W.D. Schneider. Fluorescence and Phosphorescence from Individual C_{60} Molecules Excited by Local Electron Tunneling. *Phys. Rev. Lett.*, 95: 196102, 2005.

[126] V. Iancu, A. Deshpande, and S.W. Hla. Manipulating Kondo Temperature via Single Molecule Switching. *Nano Lett.*, 6:820, 2006.

[127] N. Henningsen, K.J. Franke, G. Schulze, I. Fernández-Torrente, B. Priewisch, K. Rück-Braun, and J.I. Pascual. Active Intramolecular Conformational Dynamics Controlling the Assembly of Azobenzene Derivatives at Surfaces. *ChemPhysChem*, 9:71, 2008.

[128] S. Hagen, P. Kate, M.V. Peters, S. Hecht, M. Wolf, and P. Tegeder. Kinetic analysis of the photochemically and thermally induced isomerization of an azobenzene derivative on Au(111) probed by two-photon photoemission. *Appl. Phys. A*, 93:253, 2008. in press.

[129] B.W. Hoogenboom, R. Hesper, L.H. Tjeng, and G.A. Sawatzky. Charge transfer and doping-dependent hybridization ofC_{60} on noble metals. *Phys. Rev. B*, 57:11939, 1998.

[130] P.J. Benning, F. Stepniak, and J.H. Weaver. Electron-diffraction and photoelectron-spectroscopy studies of fullerene and alkali-metal fulleride films. *Phys. Rev. B*, 48:9086, 1993.

[131] N. Koch, S. Duhm, J.P. Rabe, A. Vollmer, and R.L. Johnson. Optimized Hole Injection with Strong Electron Acceptors at Organic-Metal Interfaces. *Phys. Rev. Lett.*, 95:237601, 2005.

[132] L. Romaner, G. Heimel, J.L. Brédas, A. Gerlach, F. Schreiber, R.L. Johnson, J. Zegenhagen, S. Duhm, N. Koch, and E. Zojer. Impact of Bidirectional Charge Transfer and Molecular Distortions on the Electronic Structure of a Metal-Organic Interface. *Phys. Rev. Lett.*, 99: 256801, 2007.

[133] Y. Zou, L. Kilian, A. Schöll, T. Schmidt, R. Fink, and E. Umbach. Chemical bonding of PTCDA on Ag surfaces and the formation of interface states. *Surf. Sci.*, 600:1240, 2006.

[134] K.F. Braun and S.W. Hla. Probing the Conformation of Physisorbed Molecules at the Atomic Scale Using STM Manipulation. *Nano Lett.*, 5:73, 2005.

[135] H. Vázquez, R. Oszwaldowski, P. Pou, J. Ortega, R. Pérez, F. Flores, and A. Kahn. Dipole formation at metal/PTCDA interfaces: Role of the Charge Neutrality Level. *Europhys. Lett.*, 65:802, 2004.

[136] K.J. Franke, G. Schulze, N. Henningsen, I. Fernández-Torrente, J.I. Pascual, S. Zarwell, K. Rück-Braun, M. Cobian, and N. Lorente. Reducing the Molecule-Substrate Coupling in C_{60}-Based Nanostructures by Molecular Interactions. *Phys. Rev. Lett.*, 100:036807, 2008.

[137] Y. Park, V.E. Choong, B.R. Hsieh, C.W. Tang, and Y. Gao. Gap-State Induced Photoluminescence Quenching of Phenylene Vinylene Oligomer and Its Recovery by Oxidation. *Phys. Rev. Lett.*, 78:3955, 1997.

[138] G.V. Nazin, X.H. Qiu, and W. Ho. Visualization and Spectroscopy of a Metal-Molecule-Metal Bridge. *Science*, 302:77, 2003.

[139] J. Repp, G. Meyer, S.M. Stojković, A. Gourdon, and C. Joachim. Molecules on Insulating Films: Scanning-Tunneling Microscopy Imaging of Individual Molecular Orbitals. *Phys. Rev. Lett.*, 94:026803, 2005.

[140] L. Ruppel, A. Birkner, G. Witte, C. Busse, T. Lindner, G. Paasch, and C. Wöll. A defect-free thin film pentacene diode: Interplay between transport and scanning tunneling microscope tip tunneling injection. *J. Appl. Phys.*, 102:033708, 2007.

[141] H.L. Zhang, W. Chen, H. Huang, L. Chen, and A.T.S. Wee. Preferential Trapping of C_{60} in Nanomesh Voids. *J. Am. Chem. Soc.*, 130:2720, 2008.

[142] S. Stepanow, M. Lingenfelder, A. Dmitriev, H. Spillmann, E. Delvigne, N. Lin, X. Deng, C. Cai, J.V. Barth, and K. Kern. Steering molecular organization and host-guest interactions using two-dimensional nanoporous coordination systems. *Nat. Mater.*, 3:229, 2004.

[143] E.I. Altman and R.J. Colton. Determination of the orientation of C_{60} adsorbed on Au(111) and Ag(111). *Phys. Rev. B*, 48:18244, 1993.

[144] E.I. Altman and R.J. Colton. The interaction of C_{60} with noble metal surfaces. *Surf. Sci.*, 295:13, 1993.

[145] J.L. de Boer, S. van Smaalen, V. Petricek, M. Dusek, M.A. Verheijen, and G. Meijer. Hexagonal close-packed C_{60}. *Chem. Phys. Lett.*, 219: 469, 1994.

[146] S. Liu, Y.J. Lu, M.M. Kappes, and J.A. Ibers. The Structure of the C_{60} Molecule: X-Ray Crystal Structure Determination of a Twin at 110 K. *Science*, 254:408, 1991.

[147] S. Stepanow, N. Lin, J.V. Barth, and K. Kern. Non-covalent binding of fullerenes and biomolecules at surface-supported metallosupramolecular receptors. *Chem. Commun.*, page 2153, 2006.

[148] S.C. Veenstra, A. Heeres, G. Hadziioannou, G.A. Sawatzky, and H.T. Jonkman. On interface dipole layers between C_{60} and Ag or Au. *Appl. Phys. A*, 75:661, 2002.

[149] R.C. Haddon, L.E. Brus, and K. Raghavachari. Electronic structure and bonding in icosahedral C_{60}. *Chem. Phys. Lett.*, 125:459, 1986.

[150] G.K. Wertheim and D.N.E. Buchanan. Interfacial reaction of C_{60} with silver. *Phys. Rev. B*, 50:11070, 1994.

[151] M.R.C. Hunt, S. Modesti, P. Rudolf, and R.E. Palmer. Charge transfer and structure in C_{60} adsorption on metal surfaces. *Phys. Rev. B*, 51: 10039, 1995.

[152] R.W. Lof, M.A. van Veenendaal, B. Koopmans, H.T. Jonkman, and G.A. Sawatzky. Band gap, excitons, and Coulomb interaction in solid C_{60}. *Phys. Rev. Lett.*, 68:3924, 1992.

[153] S. Duhm, A. Gerlach, I. Salzmann, B. Bröker, R.L. Johnson, F. Schreiber, and N. Koch. PTCDA on Au(111), Ag(111) and Cu(111): Correlation of interface charge transfer to bonding distance. *Org. Electron.*, 9:111, 2008.

[154] J. Hwang, E.G. Kim, J. Liu, J.L. Brédas, A. Duggal, and A. Kahn. Photoelectron Spectroscopic Study of the Electronic Band Structure of Polyfluorene and Fluorene-Arylamine Copolymers at Interfaces. *J. Phys. Chem. C*, 111:1378, 2007.

[155] N. Koch. Energy levels at interfaces between metals and conjugated organic molecules. *J. Phys.: Condens. Matter*, 20:184008, 2008.

Abbreviations

Abbreviation	Description
6T	α-SexiThiophene
AES	Auger Electron Spectroscopy
AFM	Atomic Force Microscopy/Microscope
BE	Binding Energy
COM	Conjugated Organic Molecule
DFT	Density Functional Theory
DH6T	α,ω-DiHexyl-SexiThiophene
DOS	Density Of States
EA	Electron Affinity
EIB	Electron Injection Barrier
fcc	Face-Centered Cubic
FFT	Fast Fourier Transformation
HATCN	HexaAzaTriphenylene-hexanitrile (= six ‘CN’)
HBC	hexa-*peri*-HexaBenzoCoronene
hcp	Hexagonal Close-Packed
HIB	Hole Injection Barrier
HOMO	Highest Occupied Molecular Orbital
HOPG	Highly Oriented Pyrolytic Graphite
ID	Interface Dipole
IE	Ionization Energy
ITO	Indium Tin Oxide
LDOS	Local Density Of States
LEED	Low Energy Electron Diffraction
LUMO	Lowest Unoccupied Molecular Orbital
ML	MonoLayer
NEXAFS	Near Edge X-ray Absorption Fine Structure
OFET	Organic Field-Effect Transistor
OLED	Organic Light Emitting Diode

OPVC	Organic PhotoVoltaic Cell
OTFT	Organic Thin Film Transistor
PEN	PENtacene
PES	PhotoElectron Spectroscopy
PFP	PerFluoroPentacene
QCM	Quartz Crystal Microbalance
SD	Surface Dipole
SECO	Secondary Electron Cut-Off
SFM	Scanning Force Microscopy/Microscope
SPM	Scanning Probe Microscopy
STM	Scanning Tunneling Microscopy/Microscope
TDS	Thermal Desorption Spectroscopy
UHV	Ultra High Vacuum
UPS	Ultraviolet Photoelectron Spectroscopy
XAS	X-ray Absorption Spectroscopy
XPS	X-ray Photoelectron Spectroscopy

Publications

Journal contributions

Journal contributions in chronological order. Publications which belong to this thesis' work are marked by bold titles.

1. Influence of Alkyl Chain Substitution on Sexithienyl-Metal Interface Morphology and Energetics
   S. Duhm, H. Glowatzki, R. L. Johnson, J. P. Rabe, and N. Koch
   Appl. Phys. Lett. 88 (2006) 203109

2. Morphology, interfacial electronic structure and optical properties of oligothiophenes grown on ZnSe(100) by molecular beam deposition
   S. Blumstengel, N. Koch, S. Duhm, H. Glowatzki, C. Xu, J. P. Rabe, F. Henneberger, R. L. Johnson, A. Yassar
   Phys. Rev. B 73 (2006) 165323

3. Weak charge transfer between an acceptor molecule and metal surfaces enabling organic/metal energy level tuning
   S. Duhm, H. Glowatzki, V. Cimpeanu, J. Klankermayer, J. P. Rabe, R. L. Johnson, N. Koch,
   J. Phys. Chem. B 110 (2006) 21069

4. Spontaneous charge transfer at organic-organic homo-interfaces to establish thermodynamic equilibrium
   S. Duhm, H. Glowatzki, R. L. Johnson, J. P. Rabe, N. Koch
   Appl. Phys. Lett. 90 (2007) 122113

5. Internal structure of nanoporous TiO_2 / polyion thin films prepared by layer-by-layer deposition
   R. Kniprath, S. Duhm, H. Glowatzki, N. Koch, S. Rogaschewski, J. P. Rabe, S. Kirstein
   Langmuir 23 (2007) 9860

6. **Molecular chains and carpets of sexithiophenes on Au(111)**
H. Glowatzki, S. Duhm, K.-F. Braun, J.P. Rabe and N. Koch
Phys. Rev. B. 76 (2007), 125425

7. Energy level alignment for electrically doped hole transport layers on ITO or PEDOT:PSS anodes
K. Fehse, S. Olthof, K. Walzer, K. Leo, R. L. Johnson, H. Glowatzki, B. Bröker, N. Koch
J. Appl. Phys. 102 (2007) 073719

8. **Hexa-*peri*-hexabenzocoronene on Ag(111): monolayer/multilayer transition of molecular orientation and electronic structure**
H. Glowatzki, G. N. Gavrila, S. Seifert, B. Holland, R.L. Johnson, J. P. Rabe, K. Müllen, D. R. T. Zahn, N. Koch
J. Phys. Chem. C 112 (2008), 1570

9. Adsorption induced intramolecular dipole: Correlating molecular conformation and interface electronic structure
N. Koch, A. Gerlach, S. Duhm, H. Glowatzki, G. Heimel, A. Vollmer, Y. Sakamoto, T. Suzuki, J. Zegenhagen, J. P. Rabe, F. Schreiber
J. Am. Chem. Soc. 130 (2008) 7300

10. Electronic coupling in organic-inorganic semiconductor hybrid structures with type-II energy level alignment
S. Blumstengel, S. Sadofev, C. Xu, J. Puls, H. Glowatzki, R. L. Johnson, N. Koch, F. Henneberger
Phys. Rev. B 77 (2008) 085323

11. Orientation-dependent ionization energies and interface dipoles in ordered molecular assemblies
S. Duhm, G. Heimel, I. Salzmann, H. Glowatzki, R. L. Johnson, A. Vollmer, J. P. Rabe, N. Koch
Nature Mater. 7 (2008) 326

12. Interface formation and electronic structure of sexithiophene on ZnO
S. Blumstengel, N. Koch, S. Sadofev, P. Schäfer, H. Glowatzki, R. L. Johnson, J. P. Rabe, F. Henneberger
Appl. Phys. Lett. 92 (2008) 193303

13. **Soft metallic contact to isolated C_{60} molecules**
H. Glowatzki, B. Bröker, R.-P. Blum, O. T. Hofmann, A. Vollmer, R. Rieger, K. Müllen, E. Zojer, J. P. Rabe, N. Koch
Nano Lett. 8 (2008) 3825

14. Data scattering in scanning tunneling spectroscopy
    N. Severin, S. Groeper, R. Kniprath, H. Glowatzki, N. Koch, I.M. Sokolov, J.P. Rabe
    Ultramicroscopy 109 (2008) 85
15. **Influence of pentacene fluorination on the molecule-metal interface formation**
    H. Glowatzki, A. Vollmer, G. Heimel, J.P. Rabe, N. Koch
    in preparation

Conference Contributions

1. STM structure analysis of bismuth high-TC crystals depending on the bias voltage
   10th March 2004, DPG-Meeting in Regensburg (Germany)
   Talk
   Travel grant by the ‘Wilhelm und Else Heraeus Stiftung’
2. STM structure analysis of Pb-doped Bi-2212 depending on the Pb-content
   5th March 2005, DPG-Meeting in Berlin
   Talk
3. Molecular wires and carpets of sexithiophenes on Au(111)
   29th September 2006, Scanning Probe Microscopies and Organic Materials XV in Dresden
   Talk
4. Molecular wires and carpets of sexithiophenes on Au(111)
   26th March 2007, DPG-Meeting in Regensburg
   Talk
5. Monolayer to multilayer transition of hexa-peri-hexabenzocoronene on Ag(111)
   26th February 2008, DPG-Meeting in Berlin
   Poster
6. Thin film growth of hexa-peri-hexabenzocoronene on Ag(111): Monolayer to multilayer transition
   28th May 2008, E-MRS 2008 Spring Meeting in Strasbourg
   Talk
   Travel grant by the ‘Fonds der Chemischen Industrie’

Acknowledgments

Of course, the work on this thesis would not have been possible without the support and help of many people. At first I would like to thank Dr. Norbert Koch for giving me the possibility to work in his group and introducing me to the exciting field of organic electronics. With his enormous experimental experience and overwhelming knowledge about organic electronics, he has been a fantastic mentor with brilliant ideas, who was always open for fruitful discussions. Furthermore, I would like to thank Prof. Jürgen P. Rabe for providing me the access to the experimental equipment in his laboratories and the many stimulating suggestions in scientific discussions.

The experimental work at the synchrotron sources was only possible with the help of several people. UPS data at HASYLAB in Hamburg was derived with assistance of Dr. Norbert Koch and Dr. Steffen Duhm. Important to mention is the continuous technical support by Prof. Robert L. Johnson (Universität Hamburg), who keeps the machine at HASYLAB alive. I was introduced to NEXAFS by Dr. Gianina N. Gavrila, who conducted the measurements with me at BESSY in Berlin and was also a great help by the analysis and discussion of the data. Further support in taking NEXAFS spectra was given by Stefan Seifert. Additional UPS measurements were done also at BESSY by Dr. Antje Vollmer and Dr. Georg Heimel, which were both supporting me with inspiring scientific discussions and suggestions.

For performing theoretical simulations I would like to thank Oliver T. Hofmann and Prof. Egbert Zojer from the Graz University of Technology. Their fantastic calculations were crucial on the way of understanding the experimental results and deriving a coherent picture.

Although not knowing personally, I want to thank Ralph Rieger, Dr. Hans-Joachim Räder and Prof. Klaus Müllen from the Max Planck Intitute for Polymer Research in Mainz for providing the prototypical molecules which have these extraordinary properties.

Additional support through technical assistance and scientific discussion I received from several people at Humboldt Universität, which I want to mention (in arbitrary order): Benjamin Bröker, Dr. Nikolai Severin, Dr. Rolf

Kniprath, Jörn-Oliver Vogel and Dr. Ingo Salzmann. Special thanks I want to say to Dr. Ralf-Peter Blum, who was always there to help me and open for my numerous questions, even before he became a member of our group. Of course, I want to thank all the members of the group for creating this nice atmosphere, which makes it a joy to work in the group. Evi Poblenz, Sabine Schönherr and Lothar Geyer provided excellent administrative support.

Finally, I want to thank my family, especially my mother and my girlfriend for supporting me throughout my whole study.

Selbständigkeitserklärung

Hiermit erkläre ich, die Dissertation selbständig und nur unter Verwendung der angegebenen Hilfen und Hilfsmittel angefertigt zu haben.

Ich habe mich anderwärts nicht um einen Doktorgrad beworben und besitze nicht einen entsprechenden Doktorgrad.

Ich erkläre die Kenntnisnahme der dem Verfahren zugrunde liegenden Promotionsordnung der Mathematisch-Naturwissenschaftlichen Fakultät I der Humboldt-Universität zu Berlin.

Hendrik Glowatzki
Berlin, 19. Januar 2009